# AFM INVESTIGATION OF RIPPLED STRUCTURES IN FRICTION, WEAR AND ADHESION ON THE NANOSCALE

Tesis presentada por
**Patricia Pedraz Carrasco**

Para optar al título de Doctor en Física de la Materia Condensada y Nanotecnología

Departamento de Física de la Materia Condensada

Universidad Autónoma de Madrid

Madrid, Febrero 2017

# INVESTIGACIÓN MEDIANTE AFM DE ESTRUCTURAS ONDULADAS EN LA FRICCIÓN, EL DESGASTE Y LA ADHESIÓN EN LA NANOESCALA

Tesis presentada por
**Patricia Pedraz Carrasco**

Para optar al título de Doctor en Física de la Materia Condensada y Nanotecnología

Departamento de Física de la Materia Condensada

Universidad Autónoma de Madrid

Madrid, Febrero 2017

Tesis presentada para optar al título de Doctor en Física de la Materia Condensada y Nanotecnología.

Director de tesis:
**Dr. Enrico Gnecco**

Tutor de tesis:
**Dr. Amadeo López Vázquez de Parga**


Universidad Autónoma de Madrid


Instituto Madrileño de Estudios Avanzados

*Breakthrough innovation occurs when we bring down boundaries and encourage disciplines to learn from each other.*

*Gyan Nagpal*

# CONTENTS

# ABSTRACT

Since friction, wear and adhesion are essential in everyday life, industrial applications and environmental issues it is quite surprising that the understanding of fundamental mechanisms governing the processes occurring when two surfaces slide past each other is quite restricted. Additionally, nowadays this limitation also creates ongoing challenges as technologically relevant devices are miniaturized and nanotechnology exponentially grows. In fact, it has been demonstrated that one of the most important bottlenecks of current nanotechnological applications is the poor control over the so-called “nanotribology”, which results into low device reliability and lifespan.

The main goal of this PhD thesis is to investigate the subtle interconnections between wavy (“rippled”) nanostructures on different material surfaces and various nanotribological properties observed on those surfaces from the atomic scale to the microscale. The primary tool used in this work is the atomic force microscope (AFM) and its extensions, which offer the possibility to study, among other parameters, friction, wear and adhesion with high resolution on different types of materials and environments. Aiming to fill the gap between investigations on basic (usually atomically flat) surfaces and applications ranging from abrasive wear to cell motility and graphene technology, three examples of ripple structures have been selected and characterized.

First of all, the thesis focuses on the complex topic of polymer nanotribology. To this end, the plastic response of solvent-enriched polystyrene thin films is studied while the film is locally scraped by the AFM tip. As a result of the ploughing process, the surface might become patterned by nanoripples. Surface rippling phenomenon is consistently investigated by varying the applied load, the scan rate and the scan pattern. An adaptation of Prandtl-Tomlinson model is proposed to explain the time and spatial evolution of the surface patterns and successfully compared with the experimental results. The rippling is attributed to a transition from continuous sliding to stick-slip, resembling similar observations in atomic scale sliding friction experiments. Following this analogy, it is also demonstrated that the damage caused by the tip interacting with the polymer can be controlled by introducing out of plane ultrasonic vibrations into the system. According to the results, both wear and friction are reduced or even suppressed when vertical vibrations are applied at a frequency close to the contact resonance frequency of the tip contacting the sample with sufficiently high excitation amplitude.

As a next step, much harder glass nanoripples, produced over broad areas by defocused ion beam sputtering, are used to study how these anisotropic topographies modify the behaviour of larger structures deposited on them. In an attempt to continue AFM experiments on gold nanoparticles manipulated on those substrates, this PhD work has addressed the tribological response of neural stem cells and specifically of filopodia, which are cytoplasmic nanoprojections considered the guiding parts of the cells. In particular, it is found that cell filopodia preferentially align either parallel or perpendicular to the ripple direction and get trapped in those configurations. As a consequence, cells are prevented to spread out

and become less adherent to the rippled substrate, as compared to flat glasses, which makes any attempt of manipulating them extremely challenging.

Finally, a third type of ripples are thermally created in suspended graphene membranes with the aim of investigating the influence of local roughness variations on the tribological properties of this solid lubricant in air. The obtained variability in the pattern characteristics made these samples not suitable for a comparative study, but this did not prevent us to go on with nanotribology investigations on graphene. Specifically, we have focused on high resolution imaging of supported graphene on copper in water extending previous work on atomic scale friction force microscopy of crystalline materials. The experimental observations are also compared to molecular dynamics (MD) simulations done in water and ultrahigh vacuum (UHV). As a result, the role of water in this type of measurements seems to be purely stochastic, which makes the obtained stick-slip practically identical to the one in UHV.

# RESUMEN

Dado que la fricción, el desgaste y la adhesión son esenciales tanto en la vida cotidiana como en aplicaciones industriales y cuestiones medioambientales, es bastante sorprendente que la comprensión de los mecanismos fundamentales que gobiernan los procesos que ocurren cuando dos superficies se deslizan entre sí es bastante reducida. Además, hoy en día esta limitación también crea continuos desafíos como en el caso de la miniaturización de los dispositivos tecnológicos y el crecimiento exponencial de la nanotecnología. De hecho, se ha demostrado que uno de los cuellos de botella más importantes de las aplicaciones nanotecnológicas actuales es el escaso control sobre la "nanotribología" de las mismas, dando lugar a una baja fiabilidad y durabilidad de los dispositivos.

El objetivo principal de esta tesis doctoral es investigar las sutiles interconexiones entre las estructuras onduladas (*ripples*) creadas sobre diferentes superficies de materiales y diversas propiedades nanotribológicas observadas en esas superficies desde escala atómica hasta escala microscópica. La herramienta principal utilizada en este trabajo es el microscopio de fuerza atómica (AFM) así como sus técnicas asociadas, que ofrecen la posibilidad de estudiar con alta resolución, entre otros parámetros, la fricción, el desgaste y la adhesión sobre diferentes tipos de materiales y en varios medios. Con el objetivo de llenar el vacío entre investigaciones sobre superficies básicas (por lo general atómicamente planas) y aplicaciones que van desde el desgaste abrasivo hasta la motilidad celular o la tecnología del grafeno, se han seleccionado y caracterizado tres ejemplos de estructuras onduladas.

En primer lugar, la tesis se centra en el complejo mundo de la nanotribología de polímeros. Para ello, se ha estudiado la respuesta plástica de películas delgadas de poliestireno enriquecido en disolvente al rayarlas localmente con la punta de AFM. Como resultado del proceso, la superficie puede modelarse dando lugar a nanoestructuras onduladas. Este fenómeno se ha investigado sistemáticamente variando la carga aplicada, la velocidad y el patrón de escaneo. Además, se ha propuesto una adaptación del modelo de Prandtl-Tomlinson (PT) para explicar la evolución espacial y temporal de los patrones superficiales, comparando con éxito dicho modelo con los resultados experimentales. La formación de las ondulaciones se atribuye a una transición desde el fenómeno de deslizamiento continuo al proceso de *stick-slip*, de forma similar a las observaciones apreciadas con anterioridad en experimentos de fricción a escala atómica. Siguiendo esta analogía, también se ha demostrado que el daño causado por la punta al interactuar con el polímero puede ser controlado introduciendo en el sistema vibraciones ultrasónicas fuera del plano. Según estos resultados, tanto el desgaste como la fricción se reducen o incluso se suprimen al aplicar vibraciones verticales a una frecuencia próxima a la frecuencia de resonancia en contacto de la punta con la muestra cuando la amplitud de excitación es lo suficientemente alta.

En el siguiente paso, se han utilizado nanoestructuras onduladas producidas mediante bombardeo deslocalizado de iones (*defocused ion beam sputtering*) en amplias áreas de un material mucho más duro como es el vidrio, con el objetivo de estudiar cómo dichas topografías con anisotropía modifican el comportamiento de especímenes mucho más grandes depositados sobre ellas. En un intento de continuar los experimentos realizados previamente con nanopartículas de oro manipuladas mediante AFM sobre dichos sustratos, este trabajo de

doctorado ha abordado la respuesta tribológica de células madre neuronales y específicamente de sus filopodios (nanoproyecciones citoplasmáticas consideradas las guías de las células). En particular, se observa que los filopodios se alinean preferentemente en paralelo o en perpendicular a la dirección de la ondulación y quedan atrapados en estas configuraciones. Como consecuencia, las células se adhieren menos sobre el sustrato ondulado que aquellas depositadas en uno plano, haciendo que cualquier intento de manipularlas sea extremadamente complejo.

Finalmente, un tercer tipo de estructuras onduladas han sido creadas por medio de un tratamiento térmico en membranas de grafeno suspendidas con la finalidad de investigar la influencia de la variación de la rugosidad a nivel local sobre las propiedades tribológicas de este lubricante sólido en aire. La variabilidad obtenida en las características de las ondulaciones hizo que dichas muestras no fuesen adecuadas para un estudio comparativo. Sin embargo, esto no nos ha impedido continuar con la investigación sobre las propiedades nanotribológicas del grafeno. En concreto, nos hemos centrado en la obtención de imágenes de alta resolución de grafeno sobre cobre en agua, extendiendo así un trabajo previo realizado en nuestro grupo en relación con la microscopía de fuerza lateral a escala atómica en materiales cristalinos. Las observaciones experimentales se han comparado también con simulaciones de dinámica molecular (MD) realizadas en agua y en ultra alto vacío. De acuerdo con los resultados, el papel que juega el agua en este tipo de medidas parece ser puramente estocástico, lo que hace que el *stick-slip* sea prácticamente idéntico al obtenido en condiciones de vacío.

# LIST OF ACRONYMS

**AFAM** Acoustic Force Atomic Microcopy
**AFM** Atomic Force Microscopy or Atomic Force Microscope
**AOM** Acousto-Optic Modulator
**CM** Contact Mode AFM
**CVD** Chemical Vapor Deposition
**EDX** Energy-Dispersive X-ray spectroscopy
**FFM** Friction Force Microscopy
**FFT** Fast Fourier Transform
**GNP** Gross National Product
**HOPG** Highly Oriented Pyrolytic Graphite
**LFM** Lateral Force Microscopy
**MEMS** Microelectromechanical devices
**MD** Molecular dynamics
**NEMS** Nanoelectromechanical devices
**NSC** Neural Stem Cell
**PET** Polyethylene terephthalate
**PFA** Paraformaldehyde
**PMMA** Poly(methyl methacrylate)
**PS** Polystyrene
**PT** Prandtl-Tomlinson
**RIE** Reactive Ion Etching
**RMS** Room Mean Square
**SEM** Scanning Electron Microscopy
**SMD** Steered Molecular Dynamics
**SNOM** Scanning Near-Field Microscopy
**SPM** Scanning Probe Microscopy
**STM** Scanning Tunneling Microscopy
**UFM** Ultrasonic Force Microscopy
**UHV** Ultra High Vacuum

# Chapter 1

# INTRODUCTION

# 1. INTRODUCTION

In the first Chapter, the concepts of tribology, nanotribology and surface rippling phenomena are introduced and linked in order to build up a general context for the subject of the present work. Furthermore, the aim and outline of this thesis are exposed.

## 1.1. FROM TRIBOLOGY TO NANOTRIBOLOGY

The word tribology literally means "the science of rubbing" and was firstly coined by Peter Jost in 1966 [1]. It refers to the science and technology of interacting surfaces in relative motion and of associated subjects and practices. It involves, mainly, the following issues:

- Friction, which is the force that prevents the sliding of two bodies in contact.
- Wear, defined as the surface damage or removal of material from one or both of two solid surfaces in a sliding, rolling or impact motion relative to each one another. In most cases, wear occurs through surface interactions at asperities by mechanical and/or chemical means and is generally accelerated by frictional heating producing debris [2].
- Adhesion, which is described as the force required to separate two bodies in contact and is a key element in the friction process. It arises from the combination of different contributions such as the van der Waals forces, electrostatic forces, chemical bondings, hydrogen bonding forces and capillary forces [3].
- Lubrication, the process or technique to reduce friction and/or wear between surfaces in proximity and moving relative to each other.

Tribology interest dates back from the creation of fire though frictional heating, the wheel invention or the water-lubricated sleds used by the Egyptians for stone transportation to current daily life subjects such as writing, shaving, skiing or earthquakes. Furthermore, nowadays it is well known that, from a technological side, friction causes energy dissipation and wear is one of the main causes for component damage and subsequent failure of machines and devices [4]. According to the estimations, the potential economic savings that could be achieved through the development and adoption of better engineering practices by minimizing the unnecessary wear, friction and breakdowns associated with tribological failures is around 1.3 – 1.6 % of the gross national product (GNP) of developed countries [2, 5, 6]. Additionally, between one-fifth and one-third of the world's energy resources are used to overcome friction in one form or another, especially in industry and transportation [5, 7]. Consequently, their mitigation will lead to enormous economic and environmental benefits.

However, considering how much we encounter the tribological phenomena in our daily lives and the wide extend of these phenomena in technology, their fundamental understanding remains quite limited. Their multifaceted nature which requires knowledge of many disciplines including physics, chemistry, solid/fluid mechanics, thermodynamics, materials science, rheology, machine design and performance has made it difficult for scientists and engineers to develop predictive theories for most tribological phenomena [2]. Instead, empirically derived trends are often the only tools available.

The first scientific development in tribology was achieved by Leonardo da Vinci, who introduced the concept of friction coefficient as the ratio of the friction force to the normal load. His friction experiments are collected in the Codex Madrid I, which was found after being lost for 150 years in the Spanish National Library in Madrid in 1964 [8]. Until that moment, Amontons (1699) was considered the pioneer of the field. He postulates the first and the second friction laws: i) the friction force is proportional to the normal load (basically what Da Vinci previously discovered) and, ii) the friction force is independent of the apparent area of contact ($A_{app}$). In the following century, Coulomb added a third rule, which states that the friction force is independent of the sliding velocity once the motion starts, distinguishing between static and dynamic friction. It was in 1950's when Bowden and Tabor introduced the concept of real area of contact ($A_{real}$) as a very small percentage of the apparent contact area. Thus, the real contact area is formed by asperities. This means that a macroscopic contact between two apparently flat solid surfaces consists in practice of a large number of micro or nanocontacts between the asperities present on both contacting surfaces, as shown in Figure 1. In addition, it is important to note that as the load increases, more asperities come into contact and the average real contact area grows. In that way, the frictional force is dependent on the real contact area. Recently, Persson theory [9, 10] proves the contact area is proportional to the normal force in arbitrary rough surfaces by solving a diffusion-like equation with the magnification and the stress formally replacing the space and the time. In this thesis, we will not focus on the complex subject of the asperity interaction in extended contact, but rather center on the tribological behaviour of single asperity sliding on a solid surface. This is possible by the advent of atomic force microscopy techniques, which in the 1980's triggered the establishment of the so-called nanotribology.

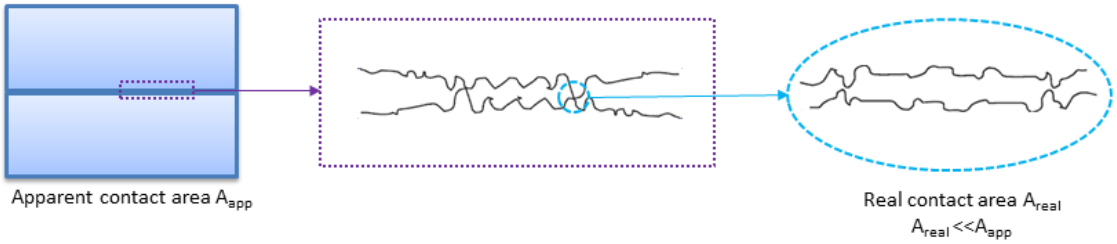


Figure 1. Scheme of asperities upon asperities.

Nanotribology is the field that involves both experimental and theoretical investigations of interfacial processes on scales ranging from the atomic-scale to the microscale, occurring during friction, adhesion, wear, indentation, scratching and thin-film lubrication at sliding surfaces [5]. In addition to the development of fundamental understanding underlying these phenomena, nanotribology is also crucial for the growth of nanotechnology. When moving from the macro to the nanoscale, the surface area-to-volume ratio increases considerably leading to severe adhesion and friction problems, which are proportional to the contact area and dramatically reduce the reliability and lifetime of MEMS and NEMS. Therefore, another goal of nanotribology is to explore new strategies for controlling friction and wear on these scales because traditional methods used on the macroscale such as liquid lubricants are inefficient when applied to nanocontacts. In these conditions, lubricant molecules are indeed found to coalesce in the interstices so that friction increases rather than decreasing. Accordingly, nanotribology is expected to provide an important bridge between science and engineering.

Until now most AFM experiments have dealt with flat surfaces. However, roughness is very important in everyday life as demonstrated in Figure 1 and the discussion above. In the thesis this key factor is introduced but in a controlled way, on almost wavy surfaces with defined average periodicity and corrugation.

## 1.2. SURFACE RIPPLING PHENOMENA

Ripples can be seen as slightly irregular undulations on an otherwise flat surface. It is known that on surfaces that are subject to external perturbations, these periodic wrinkle patterns are commonly formed over a wide range of length scales as shown in Figure 2, where examples of ripples differ by nine orders of magnitude.

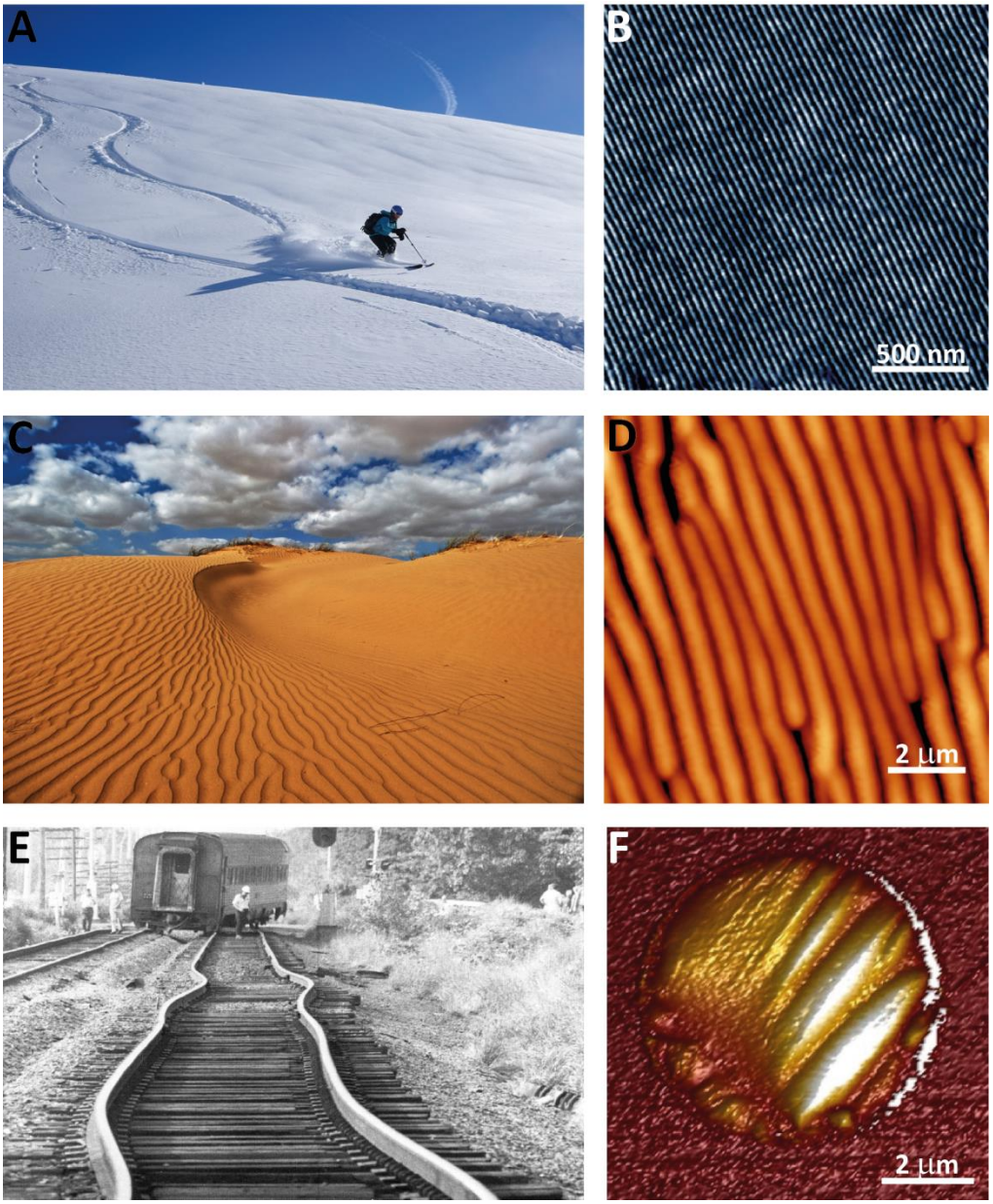


Figure 2. Ripples at different scales. (A) Ripples created locally on snow while skiing (reproduced from [11]). (B) Ripples on a polystyrene thin film produced by an AFM tip. (C) Ripples on sand dunes (reproduced from [12]). (D) Ripples on glass produced by defocused ion beam sputtering. (E) Rippled rail tracks due to thermal expansion (reproduced from [13]). (F) Ripples on a suspended graphene membrane by thermal annealing.

Rippled surfaces are obtained locally by sliding or rolling on unpaved roads or on ski slopes as presented in Figure 2 (A). A striking analogy at nanometer scale has been recognized when scanning a specific area of a surface with an AFM probe leading also to the formation of ripples, such as the polymeric ones shown in Figure 2 (B) and Chapters 3 “Surface rippling on polymers by AFM” and 4 “Control of wear by ultrasonic vibrations”. On the other hand, in nature, macro ripples (with a periodicity from meters to several centimeters) are frequently observed in rocks, sandy deserts or seashores (Figure 2 (C)) due to the erosion provoked under the action of sufficiently high water or wind shear stresses and the subsequent surface diffusion [14]. Similarly, focused ion beam sputtering can produce ripples on the micro and nanoscale over large areas in different materials such as the glass used in Chapter 5 “Influence of ripple patterns in neural stem cells” and shown in Figure 2 (D). These patterns are also the result of the combined action of ion erosion and surface diffusion but on a different scale [15]. Coming back to the macroscopic world, as rail tracks are fixed, they experience compressive stress in extreme heat, which may cause an in-plane-buckling as observed in Figure 2 (E). The same phenomenon can be used for creating out of plane undulations on free-standing graphene membranes during a cooling down procedure as discussed in Chapter 6 “Nanotribology of graphene” and shown in Figure 2 (F). It is important to note that other well-stablished techniques such as nanoimprinting or photolithography can be used for creating similar wavy patterns on the nanoscale. However, in the course of this thesis we focus on the previously mentioned processes. Moreover, it is also worthy to consider that both macro and nanoripple formations have been related to tribological issues such as the onset of wear [16, 17]. In addition, wavy patterns on surfaces have been proposed as prospective candidates for controlling friction and lubrication inside engines [18].

## 1.3. AIM AND OUTLINE OF THE THESIS

This thesis explores the formation of rippled patterns on compliant surfaces (polymers and graphene) and the use of those patterns on harder surfaces (glass) as a playground for nanomanipulation experiments, having as a common denominator the use of the atomic force microscopy (AFM). All analyzed phenomena have been related to tribological processes on the nanoscale. In particular, the onset of abrasive wear in the case of polymers and the possibility of tuning nano-adhesion of specific systems of outstanding importance in medicine such as neural stem cells.

First of all, the mechanism of surface rippling formation on polymer thin films scraped by a sharp nanoindenter was systematically studied using AFM. The results can be important to further investigate the basics of wear on the micro/nanoscale. In addition, the application of external mechanical vibrations was used to control the rippling process, as well as the accompanying friction, on the nanometric scale. As a next step, the intrinsic anisotropy of nanoripples, formed by defocused ion beam sputtering on a glass surface, was employed to evaluate the orientation and adhesion of larger systems like neural stem cells in an original attempt to use these structures as scaffolds in nanobiomedicine. Lastly, an intent of studying the effect of local roughness on tribological and mechanical behaviour of free standing graphene membranes was done by creating ripples when the sample undergoes a thermal annealing. Unfortunately, their inhomogeneities made extremely difficult a comparative study,

but we still succeeded in obtaining interesting results on supported graphene, whose nanotribological response could be investigated at atomic level in water environment.

This multidisciplinary investigation has been only possible by working in interdisciplinary research centers such as IMDEA Nanoscience and NEST Laboratory in Pisa (where I did a short placement) and in collaboration with many scientists with very different background, from theoreticians to applied researchers.

This thesis is organized as follows:

Chapter 2 gives a description of the general experimental methods and the set-up used in the course of this research. Firstly, the standard and modified AFM modes used in this work are described as well as the required force calibrations. The Chapter concludes with an overview of the employed instrumentation.

In Chapter 3 the mechanisms of ripple formation on solvent-enriched polystyrene thin films using AFM probes are systematically explored. The influence of the applied normal load, the scan rate and the distance between scan lines is investigated. In addition, the experimental results are correlated with an extension of Prandtl-Tomlinson model, which shows the transition from stick-slip to wearless sliding as resembling the transition from stick-slip to frictionless sliding in atomic scale measurements on crystal surfaces.

Chapter 4 is devoted to study the effect of out of plane ultrasonic vibrations on friction and wear control on polymers at the nanometric scale. In this case, the impacts of frequency and excitation amplitude are considered in the wear, understood as ripple formation. Furthermore, a home-built vibrometer used in order to accurately calibrate the excitation amplitude of the piezoelectric transducer is detailed.

In Chapter 5 the natural anisotropy of ripples, created on glass by defocused ion beam sputtering, is employed in order to see their influence on large neural stem cells (NSCs) behaviour. In particular, filopodia orientation, cell morphology and both global and local adhesion are compared when plating them on flat and rippled glasses.

Chapter 6 focuses on the nanotribology of graphene, a material with demonstrated solid lubricant capabilities. Firstly, local roughness variations are introduced on free-standing graphene membranes inducing the creation of large ripples by means of thermal annealing. However, the inhomogeneities on the rippled sample make difficult any comparative study. At this point, we decided to go on with the fascinating topic of friction on graphene, but rather focuses on strategies to achieve high resolution FFM images of this material. As proven by experimental results and MD simulations (in collaboration with the group of SPM theory at UAM), this goal is achieved in a straight way by measuring friction in water environment.

Finally, the results presented in this thesis are summarized in the Conclusions, followed by the Appendix, the References and the List of publications.

# Chapter 2

# EXPERIMENTAL METHODS AND SET UP

# 2. EXPERIMENTAL METHODS AND SET UP

In this chapter, a review of the physics, operating modes and characteristics of scanning probe microscopy (SPM) and, in particular, atomic force microscopy (AFM) is done. Firstly, a brief introduction of AFM is made focusing on the peculiar modes used in this thesis followed by an overview of the calibration methodology and the specific instrumentation used.

## 2.1. SCANNING PROBE MICROSCOPY

Scanning probe microscopes (SPMs) are a family of instruments characterized by the use of a sharp probe that physically scans a solid surface. They are based on the interaction between the probe and the specimen and their ability to position the material of interest in relation to the probe with nanometric or atomic resolution by making use of accurate piezoelectric scanners. In that way, a physical quantity representing the interaction (e.g. tunneling current, resonance frequency shift, etc) is recorded as a function of the position in order to create an image resembling specific properties of the surface [19].

In general, there are three main categories of SPMs:

- Scanning Tunneling Microscopy (STM)

It is the ancestor of all SPMs and was developed by Binnig and Rohrer at IBM Zurich in 1981. It was the first instrument to directly generate three dimensional (3D) images of solid surfaces with true atomic resolution [20].

STMs use a sharpened, conducting tip with a bias voltage applied between the tip and the sample. When the tip is brought close enough (0.3 – 1 nm) to the surface, the electrons "tunnel" through the gap. The resulting tunneling current varies exponentially with the tip-to-sample spacing giving a very high vertical resolution. This is thus the signal used to create the STM image. They can be operated in either the constant current mode or the constant height mode. For tunneling to take place, both the sample and the tip must be conductors or semiconductors [21].

- Atomic Force Microscopy (AFM)

AFM was invented by Binnig *et al*. in 1986 [22] and it is one of the most versatile and common SPM techniques. AFM relies on the mechanical deformations of a microcantilever holding the probing tip to produce high resolution, 3D images of sample surfaces based on measuring the forces between them and the tip. AFM will be described in detail in Section 2.2.

- Scanning Near-Field Optical Microscopy (SNOM)

This technique enables users to work with standard optical tools beyond the diffraction limit that normally restricts the resolution capability of those methods. It works by exciting the sample with light passing through an aperture formed at the end of an optical fiber. The aperture has a diameter smaller than the wavelength of the use light as well as the distance to the sample [23].

The invention of SPMs is one of the main reasons of the so-called “nanotechnological revolution” in the last 30 years [24]. Nowadays, scanning probes microscopes with the ability to image, control and manipulate solid matter down to the atomic scale together with their versatility to operate in different environment (air, vacuum, liquid, low/high temperature) are having a dramatic impact on fields as diverse as biology, material science, electrochemistry, tribology, biochemistry, surface physics and medicine [25]. Moreover, SPMs and their derivatives have found applications in many fields beyond basic research and microscopy, as interdisciplinary tool leading to new technologies.

## 2.2. ATOMIC FORCE MICROSCOPY

Atomic force microscopy is one of the most powerful modern research techniques for analyzing superficial characteristics. It allows us to investigate the morphology and the local properties of a surface with high spatial resolution [26].

AFM can sense very small forces, in the range of picoNewtons. Since the instrument measures the forces between the tip and the sample surface it is a suitable technique for both conductors and insulators.

A typical AFM set-up is shown in Figure 3. A very sharp tip (standard radius ≤ 10 nm) is located at the end of a flexible cantilever and physically interacts with the sample. Forces (Van der Waals, friction, electric, magnetic, etc) between the tip and the surface cause the cantilever to bend (deflect) or twist as the tip is scanned over the sample (scanning by probe configuration) or the sample is scanned under the tip (scanning by sample configuration). In the latter case, the sample is placed on the top of a piezoelectric scanner that moves the sample with respect to the cantilever in X, Y and Z directions with extreme accuracy. The prevalent method for measuring the deflection and twist uses a laser beam, which is focused on the cantilever rear and reflected onto a quartered photodiode. As the cantilever bends or twists, the position of the laser beam on the detector changes. Thus, the photodiode voltage reveals the movement and the system can generate the topography or other force maps at the surface with the help of a feedback loop.

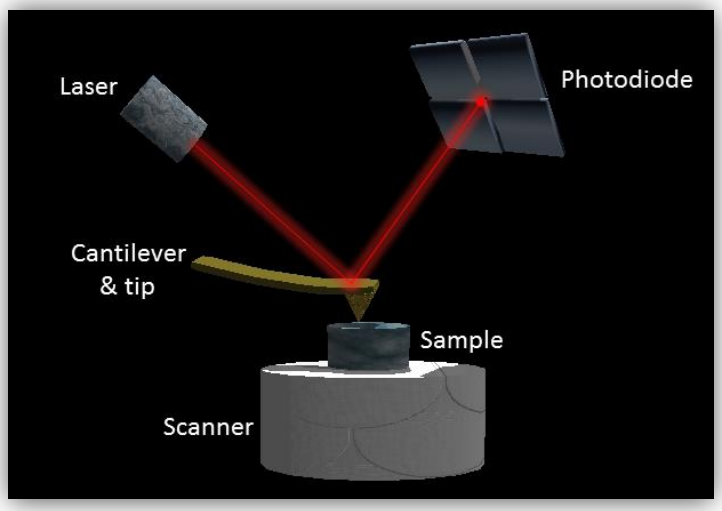


Figure 3. Scheme of an AFM set-up.

## 2.2.1. STANDARD AFM MODES FOR IMAGING

The AFMs are used in many operation modes depending on the pertinent application. The wide variety of these modes makes the AFM a very versatile and powerful tool.

The interaction force between the tip and the sample can be characterized by the Lennard-Jones potential described in Figure 4 and the different regimes can be used to generally classify the standard AFM modes for imaging. In this thesis, contact and intermittent-contact modes are used. A brief explanation of them is given below.

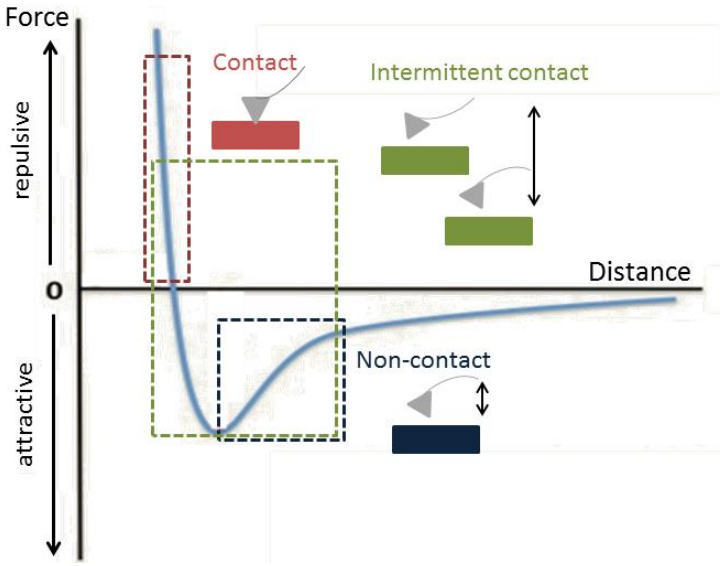


Figure 4. Tip- simple interaction and regimes related to standard AFM modes.

### 2.2.1.1. Contact mode (CM)

In contact mode, the AFM tip is always touching the sample and the contact force causes the cantilever to deflect in order to accommodate changes in topography.

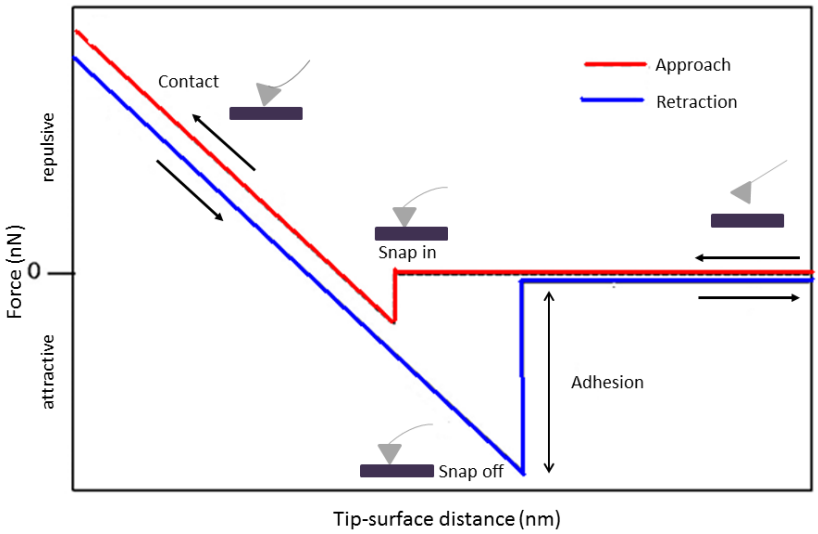


Figure 5. Scheme of a typical force-distance curve in air.

In Figure 5 a typical force-distance curve in air is shown. When the tip is far from the sample surface, the cantilever is not deflected. As the tip approaches the surface, it usually feels an attractive force and a “snap-in” occurs when the tip becomes unstable and jumps into contact with the surface. The instrument continues to push the cantilever towards the surface

and the interaction moves into the “repulsive” regime. It is within this regime where contact mode is usually performed. If the direction of the movement is reversed, the interaction passes again into the attractive regime until instability occurs again and the tip snaps off the surface. The approach and retraction curves can be different due to the capillary forces that make the tip keep attracted to the surface by adhesion.

The resolution of CM is potentially extremely high; however, large lateral forces might appear while scanning, and irreversibly damage a compliant material. Although this last process has been intentionally carried out in this thesis to investigate wear of polymers, it is clear that CM is preferred for imaging hard samples. In this mode, two configurations are possible: *constant height* and *constant force*. In the first one, the spatial variation of the deflection is used directly to generate the topography because the height of the scanner is fixed. The latter is the most common one and in this case the deflection is used as input to the feedback that moves the scanner up and down in z direction responding to the topography by keeping the deflection constant.

#### 2.2.1.2. Intermittent-contact mode

Intermittent-contact mode, also called semicontact or Tapping® is the most commonly applied technique for imaging in air. In this mode, the tip is made to oscillate close to its resonance frequency in the normal direction with a large amplitude (1-100 nm). When the tip approaches the sample surface, the oscillation changes due to the interaction with the sample surface. The detected change in the amplitude oscillation is used in a feedback loop to maintain the tip-sample interaction constant [26]. In addition to amplitude signal, the delay in the phase is often recorded.

In this case the tip and the substrate are only in brief contact during an oscillation cycle. Therefore, it is less likely to produce tip or sample degradation effects because it eliminates lateral forces (friction and drag) and it is preferred when imaging soft or brittle materials. For that reason and in order not to further damage the sample, this mode is employed for imaging ripples in polymer thin films after creating them by scratching in contact mode in Chapters 3 and 4. Furthermore, intermittent-contact mode is also other method of choice for imaging delicate cells in Chapter 5. However, in this case, the quantification of the applied normal force is much more complex than in contact mode.

### 2.2.2. FRICTION FORCE MICROSCOPY (FFM)

As we already mentioned, the relative sliding of tip and surface in contact is usually accompanied by friction. A lateral force ($F_L$), which acts in the opposite direction to the scan velocity, causes the torsion (twist) of the cantilever. In this way, the lateral movement of the lever can be related to the lateral displacement of the laser spot in the photodetector (Figure 3).

The FFM was first used by Mate *et al.* [27] in 1987 to study the friction acting on a tungsten tip dragged on graphite. They found a extremely low friction coefficient for this material, as it will be discussed in Chapter 6. Moreover, in this experiment the authors were able to recognize a saw-tooth variation of the lateral forces (shown in Figure 6 (B)). This modulation with the periodicity of the atomic lattice is due to elastic instabilities

accompanying the sliding motion of the tip, causing it to hop between neighboring lattice sites. This "stick-slip" has been reported several times in literature, especially in UHV, and will be also observed in this thesis on graphene completely covered by water (Chapter 6). Interestingly, stick-slip will also show up when studying the ripple formation on polymers in Chapter 3 on much larger scales (in the order of 100 nm).

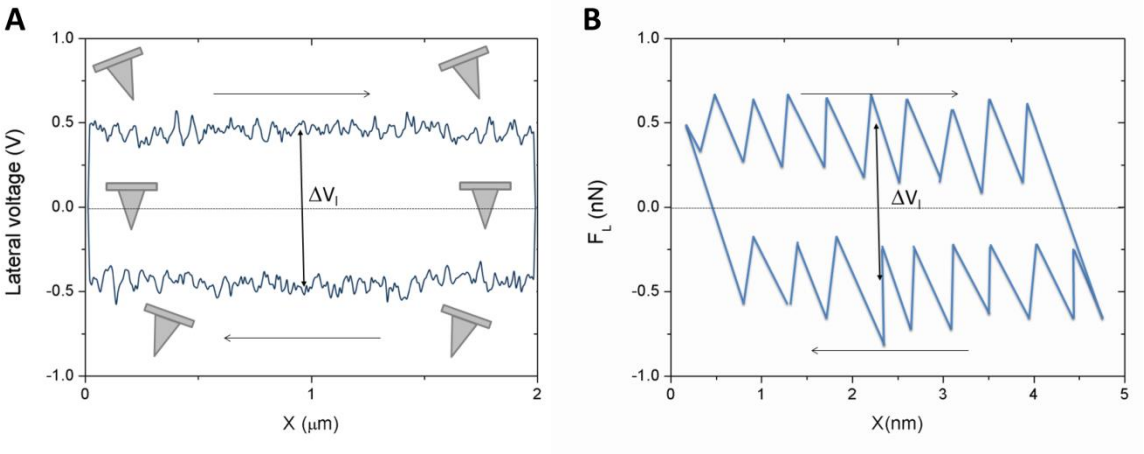


Figure 6. (A) A typical friction hysteresis loop where the $\Delta V_l$ is the difference in the lateral detector signal between the two traces. A scheme of the cross section of the probe position is shown to illustrate the twist of the cantilever at several points in the loops. (B) Typical friction loop at atomic scale where stick-slip is easily recognized. The directions of the relative lateral movement are indicated by the horizontal arrows.

Since the lateral voltage corresponding to zero friction may vary during measurements, it is a common practice to record the lateral force also in backwards and obtain the zero value from friction loops like those in Figure 6. All the features in friction loops can be interpreted within the Prandtl-Tomlinson (PT) model [28] which will be discussed in Appendix I. Note that the area in the loop represents the dissipated energy and the area divided the total distance covered by the tip (twice the scan size) is the mean lateral force [29]. Additionally, the slope of the "sticking" parts in the loop can be used to quantify the lateral stiffness of the contact [30, 31].

Moreover, the friction coefficient (μ) can be defined as the slope between the friction force and the applied load if this relation is linear (Amonton's Law). Even though this is usually the case in the contact of two rough surfaces, it is quite interesting that such as linear relation has been also observed in FFM experiments (and MD simulations) on the atomic scale.

### 2.2.3. PEAK FORCE QNM®

Peak Force Quantitative NanoMechanics® (Bruker) allows performing high resolution quantitative mapping of the mechanical properties of the materials at the same time as topographical imaging.

In this mode, the probe and the sample are intermittently brought together to contact the surface for a very short period eliminating lateral forces, combining the advantages of both contact and tapping® modes. The maximum force on the tip (peak force) is kept constant by the feedback adjusting the extension of the Z piezo.

Since the modulation frequency is around 2 kHz, a force-distance curve can be generated every 0.5 ms, with every cantilever tap [32]. Each curve is then analyzed to obtain the properties of the sample (adhesion, Young's modulus, deformation and dissipation), which are presented as image maps.

Figure 7 shows how mechanical properties are extracted from the calibrated force-separation curves. The elastic modulus is obtained by a fitting of part of the retraction curve (red bold line) using Derjaguin-Muller-Toporov (DMT) model for an elastic sphere-plane contact in the presence of adhesion [33]. The last parameter is calculated as the difference between the baseline and the minimum force during the retraction. In addition, the maximum deformation is the difference in separation from the point where the force is zero to the peak force point along the approach curve. Finally, the dissipation energy is determined by the force times the velocity integrated over one period of vibration (represented by the blue area in Figure 7).

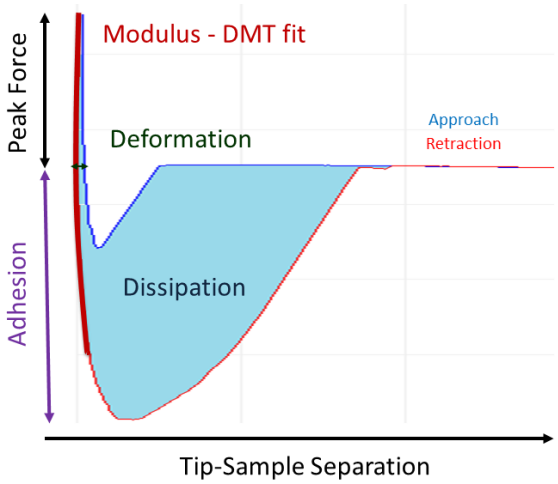


Figure 7. Force vs. separation plot showing how nanomechanical analysis is done.

This mode is used in the present work to extract information of free-standing graphene membranes, especially in adhesion and deformation signals, in Chapter 6.

### 2.2.4. ACOUSTIC SCANNING PROBE MICROSCOPY

The combination of scanning probe microscopy, in particular AFM, with ultrasounds protocols led to the development of a number of measuring techniques which allow surface mechanical properties imaging [34], among other studies.

In this approach, piezoelectric transducers are used to set the sample and/or the cantilever into vibration at ultrasonic frequencies that are well above the cutoff frequency of the electronics, so that the oscillations are not compensated by the feedback. As a consequence this oscillation does not influence the topographical image and the ac component of the deflection signal is not suppressed and can be analyzed. These are key points to simultaneously acquire both topography and acoustic signal images.

Depending on the configuration and strategies, there are many different modes. In the following sections, two of the most widely spread ones are briefly explained: acoustic force atomic microscopy (AFAM) and ultrasonic force microscopy (UFM).

### 2.2.4.1. Acoustic Force Atomic Microscopy (AFAM)

The basic idea of AFAM is to excite the cantilever of an AFM into flexural vibrations when the tip is in contact with the sample [35].

In this mode, the tip scans the surface of a sample whose back side is coupled to an ultrasonic piezoelectric transducer, which oscillates vertically (Figure 8). The resultant out-of-plane surface vibration transfers to the AFM tip and excites a forced flexural vibration of the cantilever. This can be detected by the photodiode and evaluated by a lock in amplifier.

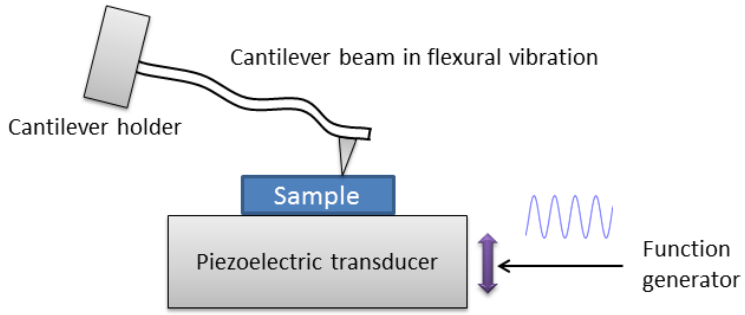


Figure 8. Scheme of an AFM cantilever vibrating in contact with the sample surface.

AFAM is a contact-resonance technique. The contact resonance is the resonance of the cantilever with the tip in contact with the sample. The tip-sample forces in the contact area influence the mechanical boundary conditions of the cantilever, and, therefore, its frequencies increase considerably compared to the frequencies in air. The contact resonance frequency depends, among other parameters, on the stiffness of the tip-sample contact, on the contact radius and the geometry of the cantilever but also on the chosen static load and on the amplitude of the induced vibration [36]. Furthermore, if the amplitude of the vibration is increased above a critical threshold, the resonance curves develop plateaus or asymmetries, which are typical for nonlinear oscillators [37]. It is important to mention that the frequencies of the contact resonances are independent of the configuration for the excitation. However, this is not the case for the amplitudes. In AFAM, the excitation amplitude is typically kept sufficiently small that the tip-sample interactions remains in the linear regime [38].

The shift of the resonance frequencies can be evaluated to measure surface stiffness and elasticity [39, 40] and the width of the resonance peaks for viscoelasticity [41]. However, in this thesis, we exploit this set-up with the aim to introduce in the system mechanical vibrations of frequencies in the range of several hundreds of kHz and amplitudes of less than 1 nm and investigate their effect on wear of polymers, as explained in Chapter 4.

### 2.2.4.2. Ultrasonic force microscopy (UFM)

In contrast to the previously mentioned technique, UFM takes advantage of the nonlinear region of the tip-sample interaction for the qualitative and quantitative imaging of the elastic properties of the sample. When the amplitude of the ultrasound is large and the tip-sample distance is swept over the nonlinear part of the force curve, the average force that acts upon the cantilever will include an additional force apart from the initial set-point force. This additional force constitutes the ultrasonic force and is the physical parameter evaluated in UFM [42, 43].

The set-up needed for this technique is also the one shown in Figure 8. The piezoelectric transducer is driven by a signal, which oscillates at ultrasonic frequency and whose amplitude is modulated by a ramp. Thus, an oscillation of the tip-sample indentation is observed. When the maximum variation of the indentation equals the static indentation and the pull-off point is reached, a periodic discontinuity in the cantilever static deflection occurs. This can be recorded by the oscilloscope and analyzed by a lock-in amplifier in order to calculate the tip-sample contact stiffness, which is inversely proportional to the amplitude of the driving signal at which the pull-off happens [34].

In the present thesis, this technique is employed in Chapter 6 to investigate suspended graphene membranes placed on the top of circular holes prepared on a substrate.

## 2.2.5. FORCE CALIBRATIONS

Force calibrations are needed in order to make quantitative measurements in AFM. In the following sections both load and friction force calculations are described.

### 2.2.5.1. Normal force calibration

Normal force or load ($F_N$) is calculated based on Hooke's law (Equation 1):

$$F_N = k_N \Delta z = k_N S^{-1} V_N$$

Equation 1

where: $F_N$ = Load (N)

$k_N$ = Normal spring constant of the cantilever (N/m)

$\Delta z$ = Displacement (m)

S = Sensitivity of the photodiode (V/m). It can be determined from the force distance curves measured on a hard surface, where the elastic deformations are negligible and the vertical movement of the scanner equals the deflection of the cantilever. Thus, the sensitivity is the slope of the elastic part of the curve (straight line in Figure 5).

$V_N$ = Set point or difference between the vertical signal of the photodiode (V).

**Calibration of the normal spring constant of the cantilever ($k_N$)**

There are many approaches for the determination of the normal spring constant of the cantilever. A good review on this topic is presented in [44]. However, only the methodologies used in the present thesis are described below. These methods are chosen depending on their availability in the equipments used for the measurements and the shape of the used cantilevers.

In most of the experiments, both rectangular and triangular cantilevers are calibrated by thermal tune method. This is probably the most popular and widely available approach and is based on modeling the cantilever as a simple harmonic oscillator. In that way, it is possible to link the thermal motion of the cantilever's fundamental oscillation mode to the thermal energy taking into account the mean square displacement of the cantilever [45]. Furthermore, Butt *et al.* [46] considered the beam theory and the actual bending modes of the cantilever obtaining the following equation:

$$k_N = \frac{16\, k_B\, T}{3\alpha_i^2 \langle z_i^2 \rangle} \left[\frac{\sin\alpha_i \sinh\alpha_i}{\sin\alpha_i + \sinh\alpha_i}\right]^2$$

Equation 2

where: $k_B$ = Boltzmann constant = $1.38 \cdot 10^{-23}$ J/K.

T = temperature (K).

$\langle z_i^2 \rangle$ = mean square displacement of the cantilever ($m^2$).

$\alpha_i$ = Constant that depends on the bending mode of the lever.

In general, thermal tune is an attractive method because of its simplicity and its applicability to both rectangular and v-shaped cantilevers. The only real limitation of this technique is that it is best applied to relative soft cantilevers where the thermal noise is well above the noise floor of the deflection measurement.

### 2.2.5.2. Friction force calibration

On the other hand, friction or lateral forces are obtained by standard continuum mechanics using Equation 3 [47]:

$$F_L = \frac{3}{2} k_L \frac{h}{L}\, S^{-1}\, V_L$$

Equation 3

where: $F_L$ = Friction force (N)

$k_L$ = Lateral spring constant (N/m)

h = Height of the tip plus the half of the cantilever thickness (m)

L = Length of the cantilever (m)

S = Sensitivity of the photodiode (V/m)

$V_L$ = Average of the trace lateral deflection minus the average of the retrace lateral deflection divided by 2 (V).

**Calibration of the torsional spring constant of the cantilever ($k_L$)**

In a similar way as previously mentioned for normal spring constant calibration, there are several methodologies for the determination of the lateral or torsional spring constant of the cantilever. Two different approaches are chosen depending on the shape of the used cantilevers.

In the case of rectangular silicon cantilevers, the torsional spring constant is determined by Equation 4:

$$k_L = \frac{G\, w\, t^3}{3\, h^2\, L}$$

Equation 4

where: $k_L$ = Lateral spring constant (N/m)

G = Shear modulus of the cantilever, for silicon, $0.5 \cdot 10^{11}$ $N/m^2$

w = Width of the cantilever (m)

t = Thickness of the cantilever (m)

h = Height of the tip plus half the cantilever thickness

L = Length of the cantilever (m).

The main error associated to this method is the measurement of the cantilever thickness, which can be indirectly determined from the resonance frequency of the lever [48]:

$$t = \frac{2\pi\sqrt{12}}{1.875^2}\sqrt{\frac{\rho}{E}} f_0 L^2$$

Equation 5

where: t = Thickness of the cantilever (m)

$\rho$ = Density of the cantilever material, for silicon, 2330 kg/m$^3$

E = Young's Modulus of the cantilever, for silicon, 1.69·1011 N/m$^2$

$f_0$ = free resonance frequency of the cantilever (Hz)

L = Length of the cantilever (m).

On the other hand, in the case of triangular or v-shaped cantilevers, the lateral spring constant is calculated by the standard method [49] given by this equation:

$$k_L = \frac{2}{6cos^2\theta + 3(1+v)sin^2\theta}\left(\frac{L}{H}\right)^2 k_N$$

Equation 6

where: $k_L$ = Lateral spring constant (N/m)

v = $Si_3N_4$ Poisson's ratio = 0.2

L = Length of the cantilever (m)

H = Height of the tip (m)

$k_N$ = normal spring constant (N/m).

# 2.3. INSTRUMENTATION

During the present thesis different AFM systems has been used depending on their capabilities for specific measurements and their availability. In this Section a brief overview of them is included.

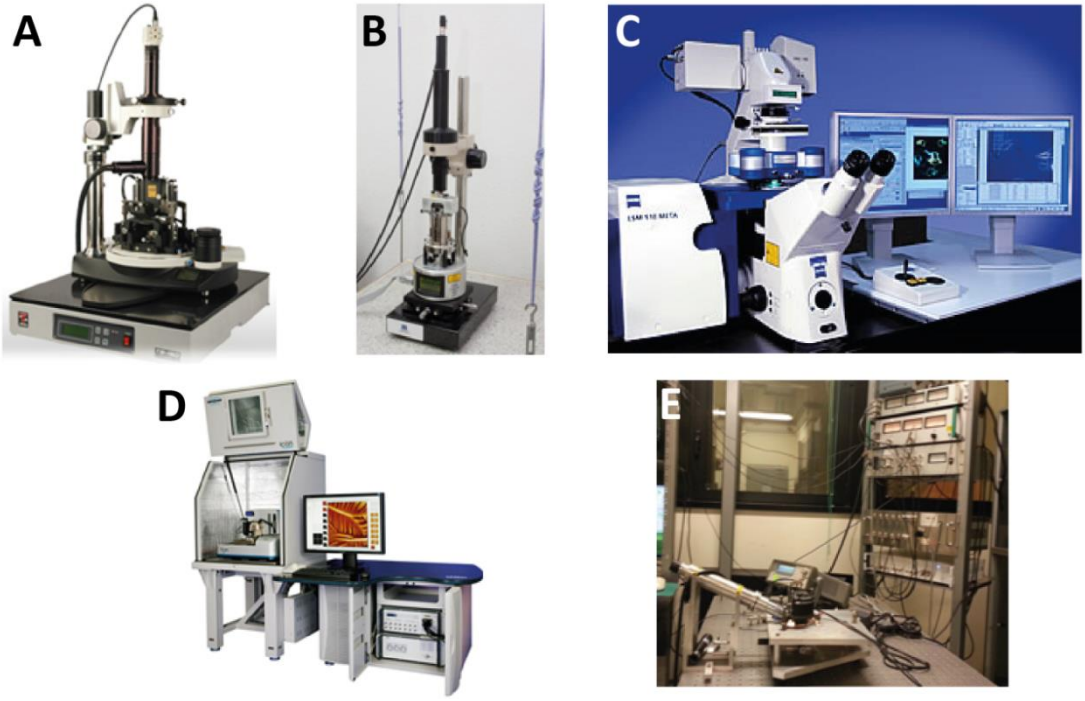


Figure 9. (A) Ntegra Prima (NT-MDT). Reproduced from [50]. (B) Multimode III (Bruker) [51]. (C) Nanowizard II (JPK) [52]. (D) Dimension Icon (Bruker) [53]. (E) Home-built AFM at CNR-INO.

The obtained images are usually processed with the specific software of each AFM. However, in some cases, WSxM software [54] is also used for analysis.

### 2.3.1. NTEGRA PRIMA (NT-MDT)

Ntegra Prima (Figure 9 (A)), available at IMDEA Nanoscience, is able to work in scanning by sample and scanning by probe configurations in dry nitrogen atmosphere and also in liquid conditions. Two different scanner sizes are accessible: 90 x 90 x 9 $\mu m^3$ and 1 x 1 x 1 $\mu m^3$. In addition to typical AFM modes, the scanning by probe configuration allows the utilization of a piezoelectric transducer for out-of-plane excitations in AFAM mode. In fact, this is one of the few commercial equipments where this mode is fully implemented. The transducer can be driven by means of the equipment software or by a external function generator (model DDS 4030, PeakTech). This instrument has been employed for measurements in Chapters 3 and 4, where vertical mechanical vibrations are induced to the tip in contact with the sample. Additionally, the software gives the possibility to obtain the contact resonance frequency sweeping up to 700 kHz.

### 2.3.2. MULTIMODE III (Bruker)

Multimode III (Figure 9 (B)), at The National Centre of Microscopy (Universidad Complutense, Madrid), is equipped with three different scanners: 1 x 1 x 1 $\mu m^3$, 15 x 15 x 1 $\mu m^3$, 150 x 150 x 10 $\mu m^3$ to work in air or liquid environment in scanning by sample configuration. Due to its outstanding high stability and resolution, it has been used for obtaining atomic resolution images of supported graphene in water in Chapter 6. This instrument has been used in collaboration with Dr. Carlos Pina and Carlos Pimentel.

### 2.3.3. NANOWIZARD II AND IV (JPK)

Nanowizard II (IMDEA Nanoscience), which works in scanning by probe configuration (Figure 9 (C)), has been conveniently employed in this PhD thesis for visualizing neural stem cells in Chapter 5. On the one hand, its scanner of 100 x 100 x 15 $\mu m^3$ is specially designed to image large specimens. Another advantage is that JPK instruments have a very accurate control of the applied load exerted by the tip (in the pN range), aiding the imaging of biological and soft samples. Furthermore, this equipment is coupled with an inverted optical microscope (Nikon Ti-U), which enables optical visualization and localization of the cells previously to the AFM acquisition.

On the other hand, Nanowizard IV at Otto-Schott-Institute für Materialforschung in Jena (Germany) has been used in Chapter 3 in order to study the effect of the distance between scan lines in ripple formation. This equipment uses raster scan and presents the advantage of having “Hover” mode which allows us to scrap the polymer in contact during the forward direction while during the backward one the tip is completely retracted.

### 2.3.4. DIMENSION ICON (Bruker)

This AFM system (Figure 9 (D)) at NEST Laboratory (Pisa, Italy) has, in addition to usual techniques, Scan Asyst® and Peak Force® modes allowing the simultaneous study of several mechanical properties in air or liquid, with an accurate control of the force. It has been used for measuring friction and other mechanical properties of graphene in Chapter 6. Apart from

being an user-friendly and very versatile equipment, it presents the benefit that its optical system with an implemented green filter extraordinarily facilitates the visualization of graphene sheets on the top of a silicon substrate.

### 2.3.5. HOME-BUILT AFM SYSTEM

This home-built AFM prototype (Figure 9 (E)) was developed at CNR-INO (Pisa, Italy) by Dr. Franco Dinelli and is specially designed to work with ultrasonics, in particular, UFM. It has been used in order to qualitatively characterize free-standing graphene membranes in Chapter 6 using frequencies around 2 MHz. The set-up employed in this equipment is composed of a commercial head (Smena, NT-MDT) that works with scanning by probe configuration, a digital lock-in amplifier (Zurich HF2LI) and home-made electronics. Its intrinsic open configuration enables also the possibility to change several conditions as the user wants.

## 2.4. USED CANTILEVERS AND PROBES

Table 1 summarizes all the different probes used throughout this thesis and their main characteristics:

Table 1. Used AFM tips and their characteristics.

| AFM tip | Company | Material | Cantilever Shape | Normal spring constant (N/m) | Free resonance frequency range (kHz) | Tip radius (nm) | Chapter |
|---|---|---|---|---|---|---|---|
| **CSG30** | NT-MDT | Silicon | Rectangular | 0.13-2 | 26-76 | <10 | 6 (UFM) |
| **FMG01** | NT-MDT | Silicon | Rectangular | 1.2-6.4 | 47-76 | <10 | 4 |
| **HA-FM** | NT-MDT | Silicon | Rectangular | ~6 | ~114 | <10 | 5 |
| **NSG01** | NT-MDT | Silicon | Rectangular | 1.45-15.1 | 87-230 | <10 | 3 |
| **Scan Asyst-air** | Bruker | Silicon nitride | Triangular | 0.2-0.8 | 45-95 | <12 | 6 (Peak Force®) |
| **SNL10 D** | Bruker | Silicon nitride | Triangular | 0.03-0.12 | 12-24 | <2 | 6 (Liquid) |

# Chapter 3

# SURFACE RIPPLING ON POLYMERS BY AFM

# 3. SURFACE RIPPLING ON POLYMERS BY AFM

In Chapter 3, ripple formation on solvent-enriched polystyrene thin films using an AFM tip is studied. In the first place, an introduction on the background of surface rippling phenomena and the mechanisms proposed for explaining it is done. Secondly, the influence of several scanning parameters such as the load, the scan rate and the distance between scan lines on surface rippling is reported. After that, these experimental results are compared with a new proposed model based on Prandtl-Tomlinson (PT) mechanism, which describes the nanoripple evolution in a single scratch test, showing a remarkable analogy with the transition from stick-slip to continuous sliding previously observed in atomic-scale friction [55]. Both experimental and theoretical results presented here suggest strategies to achieve a good control over the rippling process on polymers (and not only) at the nanoscale level.

## 3.1. BACKGROUND

### 3.1.1. SURFACE RIPPLING PHENOMENA

Appearance of periodic wrinkle patterns on a surface is often observed when the shear stress exceeds the yield strength of the material. This phenomenon is called surface rippling and occurs over a wide range of length scales. For instance, macroripples are created by wind erosion on sandy deserts and seashores [56].

The formation of macroscopic surface undulations was first discussed by Schallamach [57] in the case of an elastomer under compressive loads. Under certain conditions, waves are created perpendicularly to the sliding direction within the contact region of a rigid sphere due to the inability of the surface to sustain high shear forces [58]. The contact radius could be reduced from mm to nm, and after the invention of atomic force microscopy, the formation of nanoscale ripples induced by an AFM tip in contact has also been recognized on very different materials such as metals [59], ionic crystals [60] and semiconductors [61].

In particular, this phenomenon has been widely reported in the case of polymers, especially thin films. Nanoripples can be obtained over a polymer film when repeatedly scraping the same area with an AFM tip, as observed in a pioneer work by Leung and Goh [62]. Besides scanning several times, other approaches have been considered after that in order to reduce the number of scans and processing time. On the one hand, nanorippling is temperature dependent and, thus, it is possible to create ripples scanning only once near the glass transition temperature of the polymer by either heating the sample [63-65] or the probe [66-68]. Another way to form these nanopatterns in one scan is by taking advantage of a typical phenomenon in polymeric materials namely plasticization. In this case, the presence of solvent molecules in the polymer matrix weakens its mechanical properties making the process easier and less time consuming when using solvent-enriched polymers [69-71].

The main mechanisms proposed in literature for nanopatterning on polymer films induced by means of an AFM probe are three: Schallamach waves, fracture based descriptions and stick-slip behaviour [72]. The first already mentioned is attributed to buckling and is more suitable for simulating ripples on the macroscale than on the nanoscale [64]. Regarding the second possibility, Elkaakour and coworkers [73] proposed that surface rippling is caused by a peeling process where the material is pushed ahead of the contact by crack propagation. In addition, Iwata *et al*. [74] found that the bundles are less stiff than the undamaged surface, which is interpreted as the presence of voids or cracks in the damaged region. However, the peeling hypothesis has been recently discarded by Rice *et al.* [68] in the case of copolymers locally heated and scraped. Lastly, several authors have also suggested stick-slip behaviour at the tip-polymer interface to explain the repeating nature of the patterns [73, 75]. According to that, a hole is formed where the tip resides and a mound of polymer accumulates in advance of the scanning tip as it slides across the surface, hindering the sliding motion. Eventually, the mechanical equilibrium becomes unstable, because the lateral force overcomes the tip-sample adhesive interaction, and the tip hops (slides) over the mound and starts to form a new one. In the next forward scan the nearest part of the bump is pushed again at an angle $\theta$, creating the pattern along the scan as shown in Figure 10 (A). This mechanism was described first for the case of ripple formation on ionic crystals [60]. Furthermore, Napolitano and coworkers [70] associated the surface rippling on solvent-enriched polymer thin films to the combination of stick-slip and squeezing-drying processes. In this particular case, due to the tip pressure, the solvent evaporates while scanning forwards (Figure 10 (B)); resulting in the local hardening of the precursors.

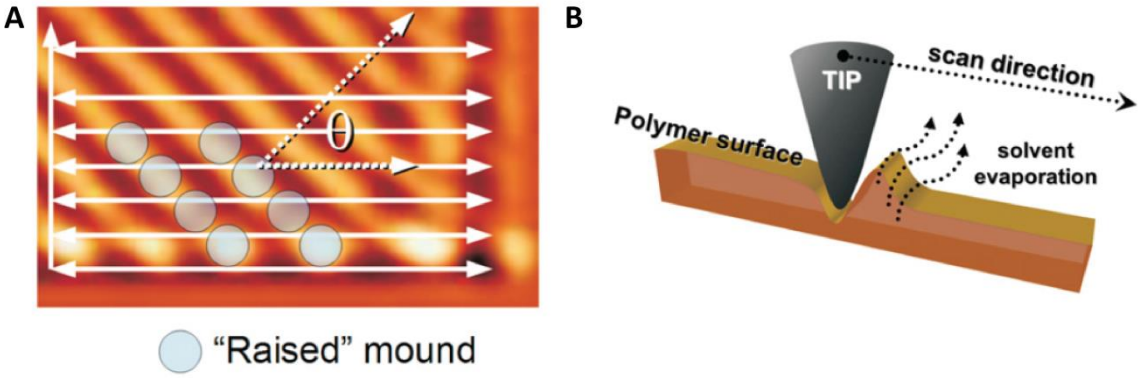


Figure 10. (A) Scheme for the nanopattern formation along one scan. (B) Scheme the combination between stick-slip and mechanically-induced solvent evaporation processes. Reproduced from [70].

Finally, it is important to recognize that many parameters can affect the formation of nanoripples. These parameters depend on the physico-chemical properties of the sample, the experimental conditions and the tip-surface contact characteristics. Regarding the influence of the material properties is worthy to mention the composition of the sample (composites, blends), the crystallinity, the presence of solvents, the temperature (as explained before) and the polymer molecular weight and monodispersity index. All these parameters strongly change the sample viscoplastic behaviour and, so that, its propensity for nanoripple formation. In the case of molecular weight ($M_w$) it is known that ripples only form if the $M_w$ value exceeds a critical one ($M_c$) that depends on the polymer. This is due to the fact that for $M_w < M_c$ the molecules are never entangled [76]. On the other hand, scanning parameters such as the load, the rate, the tip shape, the cantilever longitudinal and lateral stiffness, the spacing between

lines and the tip trajectory also play an important role on the ripple formation on those materials. A better understanding of this process is extremely important for opening the possibility of varying and controlling ripple characteristics in order to develop technological applications [72].

# 3.2. SAMPLE PREPARATION

The samples used for experiments of surface rippling on polymers are prepared using high molecular weight polystyrene (PS). The solvent enriched thin films (~400 nm) are spin coated onto silicon wafers covered by a native oxide layer (~2nm).

First of all, a new silicon wafer is cleaned by sonication for 15 min in acetone, in ethanol and in ultrapure water, successively. Between each step and at the end, the wafer is dried by nitrogen flow.

On the other hand, 6 % wt solution of PS (325000 g/mol, PDI < 1.02, Polymer Source) in toluene (Merck 99.9 %, HPLC grade) is prepared. After that, the solution is spin coated at 3000 rpm for 60 seconds in order to obtain a thickness around 400 nm as shown in Figure 11 [77].

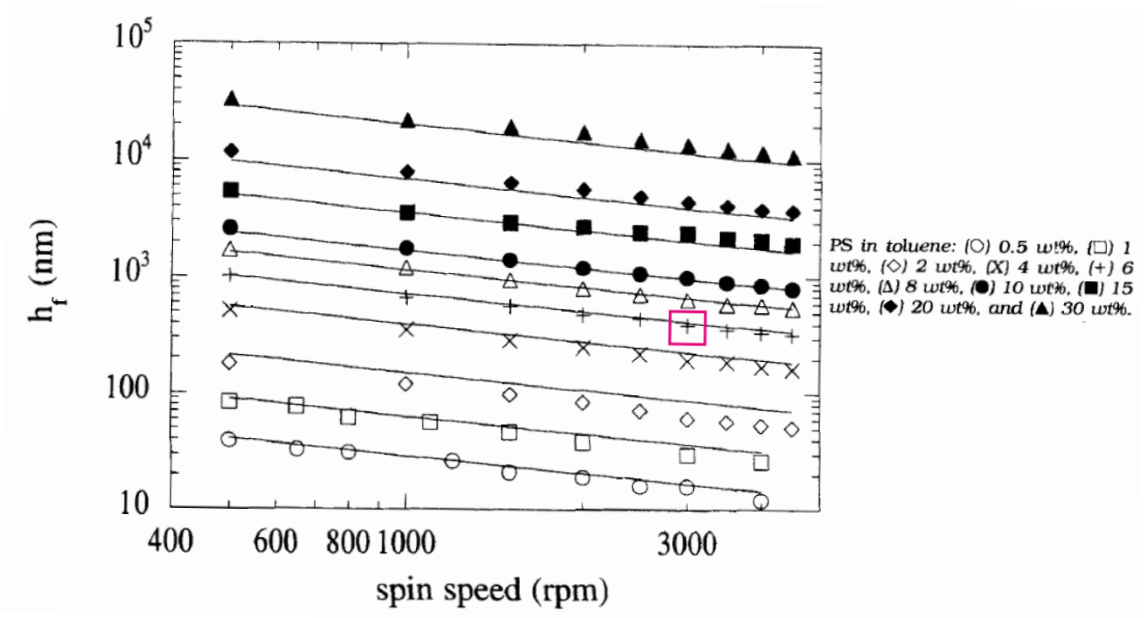


Figure 11. Film thickness ($h_f$) as a function of spin speed and initial polymer solution concentration for PS in toluene for 60 s of spincoating. The pink square shows the conditions for the preparation of our samples. Reproduced from [77].

Finally, to allow fast ripple formation, samples are used as spin coated without any thermal annealing in order to avoid complete solvent removal [69].

It is important to notice that the molecular weight has been chosen, as mentioned in the background, to be large enough to create samples prone to surface rippling.

# 3.3. EXPERIMENTAL RESULTS

The first step in this set of experiments was to test if the samples, prepared as mentioned in the previous Section, are suitable for surface rippling with an AFM tip in contact by scanning only once at room temperature.

Figure 12 shows an AFM topography and the corresponding lateral force map acquired while scanning 250 lines of 10 μm with a load of 530 nN and a scan rate of 10 μm/s. As it is observable in Figure 12 (A), very regular ripple pattern with a period around 210 nm and an amplitude of 2 nm is obtained in those conditions. In addition, the stick-slip motion of the tip (with the same periodicity) is easily recognized in the lateral force map and profiles in Figure 12 (B) and (D), respectively.

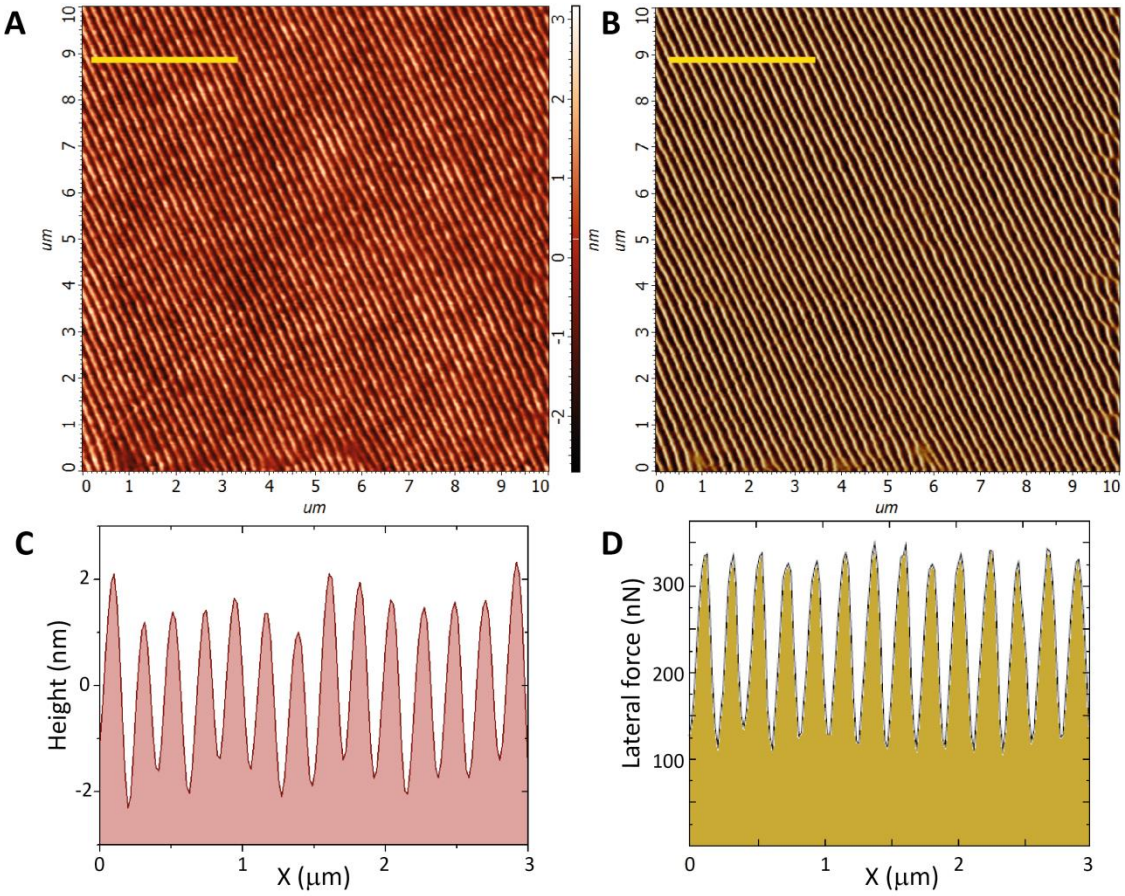


Figure 12. (A) AFM topography image (10 x 10 $\mu m^2$) and (B) lateral force map accompanying the formation of ripples on a solvent-enriched PS thin film with an applied normal force $F_N$ = 530 nN and a scan velocity $v$ = 10 μm/s. (C) and (D) Profiles corresponding to the yellow lines in (A) and (B). Number of lines = 250.

Since the samples are adequate for surface rippling, the influence of several scanning parameters (load, scan rate and distance between scan lines) on ripple characteristics such as periodicity, amplitude (corrugation) and orientation are studied in the following Sections for solvent-enriched polystyrene thin films. It is important to mention that, as elsewhere in the thesis, the ripple corrugation is defined as the amplitude of the lowest-order Fourier component of the rippled topography.

### 3.3.1. LOAD INFLUENCE

The dependence of ripple periodicity and amplitude with the normal applied force exerted by the AFM tip while scanning in contact has been investigated. Series of scratches (10 μm wide and 2 μm long) on the PS films have been done, increasing systematically the load ($F_N$) as shown in Figure 13 (A).

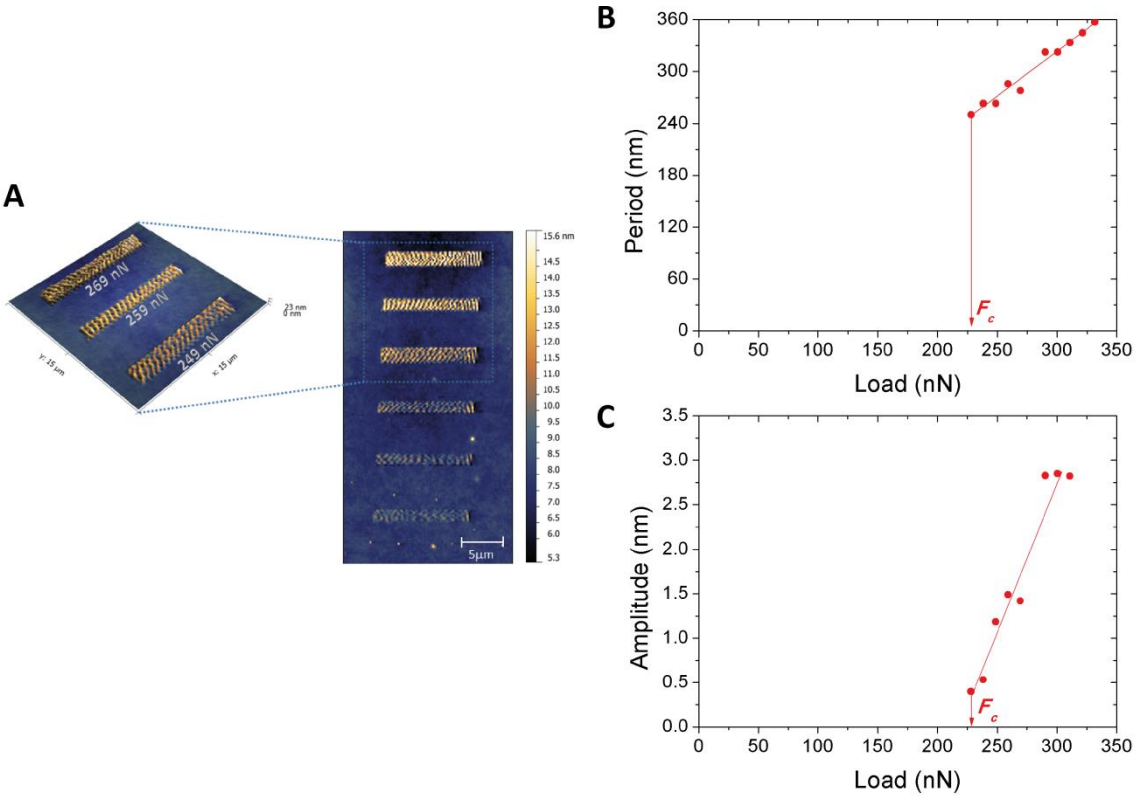


Figure 13. (A) Topography of a series of scratches performed on 10 x 2 $\mu m^2$ lines on solvent-enriched PS thin film varying the load. (B) Experimental variation of ripple periodicity and (C) ripple amplitude as a function of the normal force. The sliding velocity is $v$ = 10 μm/s and the distance between lines $b$ = 20 nm. Linear fits are also shown untill the data points where the ripple pattern becomes unstable. Critical values, corresponding to the vertical lines, are labelled with "c".

Ripple period and amplitude are estimated by doing the Fast Fourier Transform (FTT) and Figure 13 (B) and (C) show how load influences them. Both parameters are found to increase linearly with the applied normal force. This tendency is in accordance with previous results in literature regarding the ripple period and corrugation as load function [64, 70, 78]. Furthermore, it is important to notice that ripples are only formed if the load is larger than a critical value $F_c \approx 220$ nN. This critical value is associated, on the one hand, with an amplitude $A \approx 0.3$ nm and, on the other hand, with a periodicity of $\lambda_c \approx 240$ nm. The value for $\lambda_c$ suggests that the tip has a radius of about $\lambda_c / 4 \approx 60$ nm (see Scheme in Figure 18), which is larger than the nominal one for the kind of tips used for the experiments (~10 nm). However, it is consistent with SEM images of a similar tip (Figure 14 (C)) after performing repeated indentation of the polymer surface with normal forces of few hundreds of nN (Figure 14 (A) and (B)).

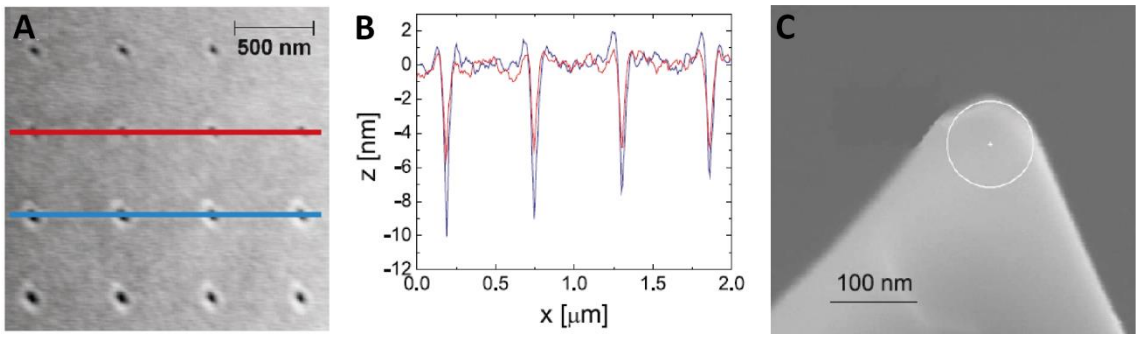


Figure 14. (A) Solvent-enriched PS surface after indentation with normal forces of 400 nN (upper two rows) and 1200 nN (lower two rows). Note that the tip was completely retracted after each indentation. (C) Height profiles corresponding to the red and blue lines in (A). (C) SEM image of a tip (nominal tip radius = 10 nm) after repeated indentations on the PS surface with loads of few hundreds nN.

## 3.3.2. SCAN RATE INFLUENCE

The velocity dependence of the ripple formation has been also tested experimentally by performing again series of scratches on the PS film, but in this case varying the scan velocity ($v$) as it is visible in Figure 15 (A).

Experiments show that ripple periodicity slightly decreases when increasing the scan rate up to a critical value $v_c \approx 45$ μm/s, which corresponds again to $\lambda_c \approx 240$ nm. Above this value, the ripples are not formed (Figure 15 (B)).

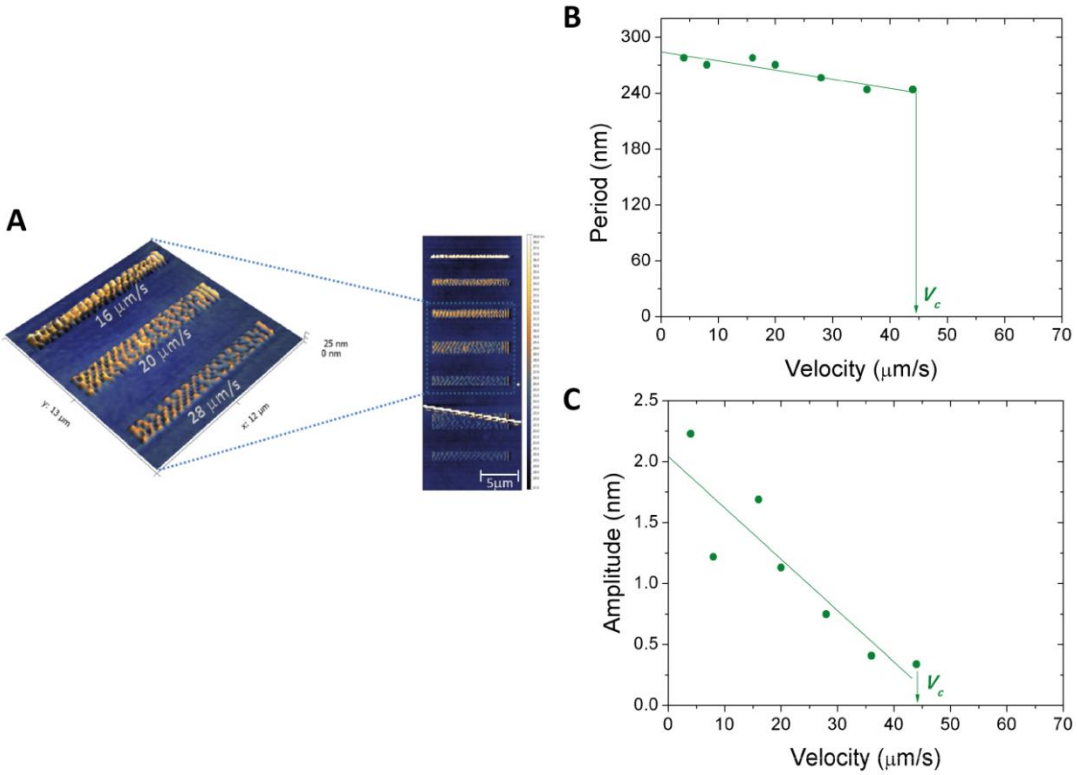


Figure 15. (A) Topography of a series of scratches performed on 10 x 2 $\mu m^2$ lines on solvent-enriched PS thin film varying the scan rate. (B) Experimental variation of ripple periodicity and (C) ripple amplitude as a function of the velocity. The applied load is in all the cases $F_N$ = 270 nN and the distance between lines $b$ = 20 nm. Linear fits are also shown untill the data points where the ripple pattern becomes unstable. Critical values, corresponding to the vertical lines, are labelled with "c".

On the other hand, the decrease of amplitude *A* with increasing scan rate *v* is more pronounced (Figure 15 (C)) and in qualitative agreement with results previously reported by Sun *et al.* [79] when working in the same load and molecular weight range. The ripples disappear again above the critical value, when the $A \approx 0.3$ nm.

### 3.3.3. SPACING BETWEEN SCAN LINES INFLUENCE

The spacing (*b*) or distance between two consecutive scan lines of the AFM tip is schematically represented in Figure 16. As it was mentioned in the introduction of this Chapter, the ripples are formed when the polymer creates a rim (see Figure 14 (A)) by the effect of the tip. When considering the 3D case, in the following scan line (separated by a distance *b*) the upper part of the previous bump is pushed again, creating the ripple pattern along the scan with an angle $\theta$ with respect to the X axis, as shown in Figure 10 (A).

First of all in this study, we considered the most typical scan patterns adopted in an AFM: raster path (Figure 16 (A)), where *b* parameter is well-defined, and zig-zag path (Figure 16 (B)). In addition, it is possible to scan only forward lines in contact while during the backward ones the tip is completely retracted (Figure 16 (C)). The latter option with only one scratch per line is more convenient for this type of experiments in order to avoid ambiguities about the scan direction with respect to the ripple orientation.

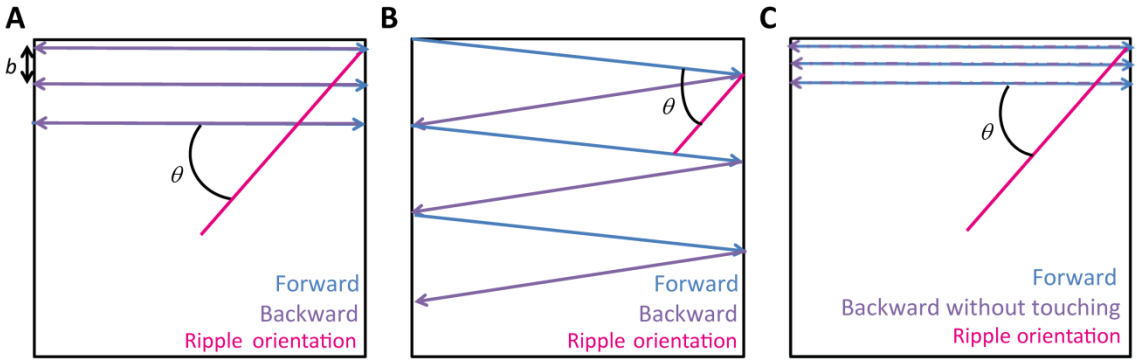


Figure 16. Schemes of (A) raster scan path, (B) zig-zag scan path and (C) raster scan path with the tip in contact only during the forward line.

The final 3D structure orientation $\theta$ depends on the spacing between scan lines in a certain analogy with the direction of motion of rigid nanospheres manipulated by AFM [80]. The exact relation between $\theta$ and *b* is determined, in addition, by the visco-elastoplastic properties of the polymer and the geometric shape of the precursor. In particular, the case of solvent-enriched PS thin films has been investigated during this thesis by varying the number of scan lines and the scan area systematically in order to obtain *b* values from 10 to 80 nm and measure the orientation of the obtained ripples under certain conditions maintaining the load and the scan rate constant.

The obtained patterns are shown in Figure 17 (A-D). According to the results, the angle $\theta$ tends to increases with the distance between lines as plotted in Figure 17 (E). This is in qualitative accordance with previous results reported by Sun *et al.* [81] when working with polycarbonate in the μN range. Furthermore, it is possible to see that if $b > 50$ nm, no ripples are found and/or the resolution is not good enough for visualizing them. Additionally, a second orientation (around 90°) appears in the left part of the images, which is related to the

propagation of boundary effects [70]. It is important to note that similar experiments were also carried out using zig-zag pattern (forward and backward) but the results were unclear.

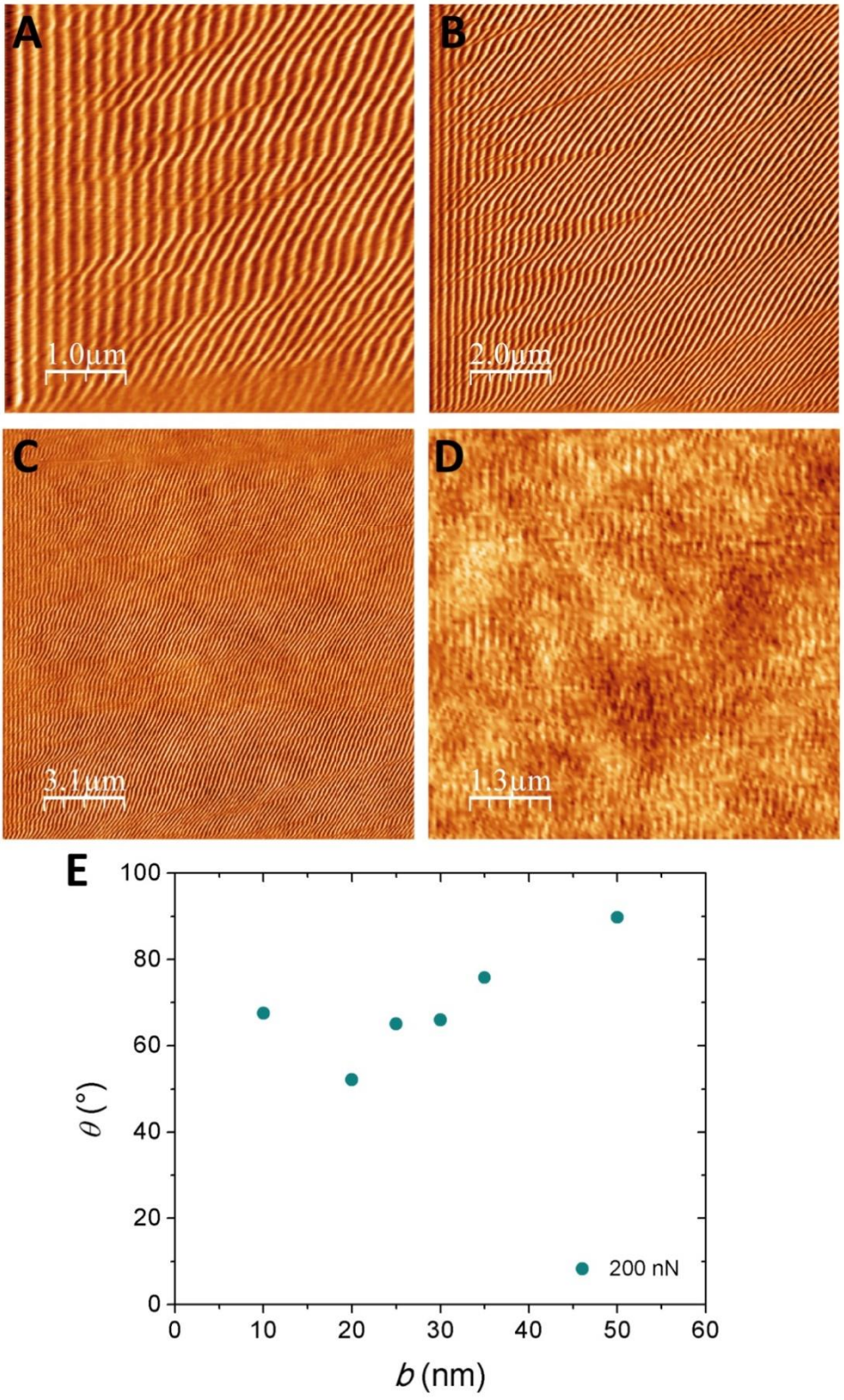


Figure 17. Topography of the pattern obtained when scanning in contact with an applied normal force $F_N$ = 200 nN on a solvent-enriched PS thin film varying the spacing between lines $b$ (A) $b$ = 10 nm, (B) $b$ = 20 nm, (C) $b$ = 30 nm and (D) $b$ = 50 nm. (E) Experimental variation of ripple orientation ($\theta$) as a function of the distance between lines ($b$) for a load of 200 nN. The scan rate in all the experiments is $v$ = 11 μm/s. The scan starts from the bottom left part of the image.

# 3.4. THEORETICAL MODEL

As previously mentioned in this Chapter, stick-slip occurs when the ripples are formed either in the case of ionic crystals [60] or at the tip-polymer interface [73, 75], suggesting interesting relations between stick-slip and surface rippling.

In this section this analogy is exploited and an original model is proposed in order to describe ripple evolution in one dimension.

The mechanism consists of the tip that, while indented into the surface with a normal force $F_N$, builds a crater with a circular rim round it. In the cross section along the scan direction two mounds ahead and behind the indentation tip appear. At the same time, the lateral force increases since the spring pulling the tip in contact is constantly elongated. If the elongation reaches a certain threshold (depending on the ripple amplitude) the equilibrium becomes unstable, the tip hops beyond the mound ahead and sticks again into the new equilibrium position on the surface and the process is repeated several times. This mechanism presents certain analogies with the Prandtl-Tomlinson (PT) model discussed in Appendix I.

Moreover, it is important to notice that the atomic structure of the substrate is not considered, which makes this continuum model quite suitable for the description of polymeric materials.

## 3.4.1. DESCRIPTION

In our approach, the AFM tip apex is represented by a point mass, which is moved at a constant velocity $v$ along a straight line. The surface profile $h(x,t)$ at the time $t$ is assumed to be indented by a Gaussian profile of half-width $\delta$ centered at the tip location $x_0$. In addition, in order to take into account the material piled up ahead and behind the tip, it is considered that the surface grows in the form of two Gaussian shape mounds with same width and half height of the indenting Gaussian. To get a realistic shape, the two mounds are centered at the distance $\pm 2\delta$ from $x_0$ as shown in Figure 18.

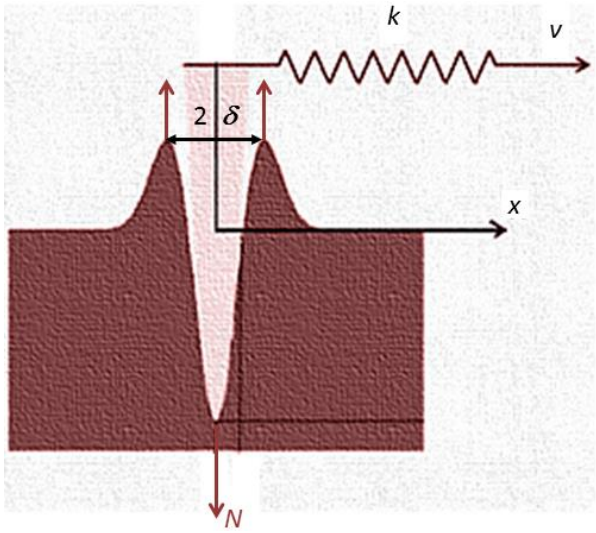


Figure 18. Scheme of the tip indenting the polymer applied to surface rippling. At a given time $t$ a rigid tip (in light pink), which is laterally pulled by a spring of stiffness $k$ at a velocity $v$, is indenting a compliant surface (dark pink).

In such a way, the overall time evolution of surface profile is described by the Equation 7. The shape of the time evolution is suggested by the typical footprints left by the tip when indenting the polymer without scanning (Figure 14 (A) and (B)). On the other hand, the factor (1/2) corresponds to the assumption that the mass density remains constant during the indentation due to the plastic deformation (Section 6.2 in [82]) and no debris is displaced far away from the indentation site. Fully plastic deformation is justified by the fact that the yield strength of PS is in the order of few tens of MPa [83] and the average normal stress in the conditions of the measurements is in the order of 1 GPa, considering the residence time of the tip is not too large.

$$\frac{\partial h}{\partial t} = N\left(-e^{-\left(x-x_0(t)\right)^2/2\delta^2} + \frac{1}{2}e^{-(x-x_0(t)-2\delta)^2/2\delta^2} + \frac{1}{2}e^{-(x-x_0(t)+2\delta)^2/2\delta^2}\right)$$

Equation 7

where: $N$ is the growth factor of the surface (nm/s)

$\delta$ is the half-width of the tip apex.

However, it is important to mention that a more accurate material-dependent characterization of the pile-up profile, which were neglected in early simulations of nanoindentation [84], can be achieved using finite or boundary element methods [85]. As a result, the pile-up process is generally found to be enhanced if the deformation is fully plastic. In addition, the pile-up profile might change during the indentation and this is not considered in this simple model.

A second important hypothesis in our approach is that the surface profile ($h(x,t)$) resembles the evolving tip-surface interaction potential $U_{int}(x,t)$. If the scan velocity $v$ is sufficiently low, the tip is locked in the equilibrium position $x_0(t)$ defined by the conditions given by the first derivative of the potential with respect to $x$ being equal to zero. In that way,

$$\frac{\partial U_{int}}{\partial t} = \frac{N_0}{N}\frac{\partial h}{\partial t}$$

Equation 8

where: $N_0$ is the growth rate of $U_{int}$ (J/s).

## 3.4.2. SIMULATIONS IN 1 DIMENSION

Simulations of polymer surface rippling are done by studying the time evolution of the potential profile $U_{int}(x,t)$ numerically by solving Equation 7 and Equation 8, considering $x_0(t)$ as the minimum of the total potential in Equation 23 (see Appendix I) at time $t$.

The indentation rate ($N$), the scan velocity ($v$) and the stiffness ($k$) are varied in a range of values consistent with previous AFM measurements on the PS surface. For that reason, we refer to Figure 12 (topography and lateral force maps acquired while scanning 250 lines of 10 μm with a load of 530 nN and a scan rate of 10 μm/s) to estimate realistic values of the model parameters. In those conditions, regular ripples of period $\lambda$ = 210 nm and amplitude $A \approx 2$ nm are obtained when using a tip with a half-width $\delta$ in the order of 50 nm (nominal tip radius = 10 nm) after several indentations (Figure 14 (C)).

According to the discussion in Section 2.2.2, the lateral stiffness of the contact $k$ is approximately given by the slope of the lateral force versus distance curves when the tip is sticking to the surface. Considering Figure 14 (D), the obtained value for stiffness is $k \approx 2$ N/m. On the other hand, the indentation rate $N$ can be estimated dividing the ripple amplitude ($A \approx 2$ nm) between the residence time $t_{res} = \lambda/v = (210\text{ nm})/(10000\text{ nm/s}) = 21$ ms. Thus, $N = A/t_{res} = 95$ nm/s. By taking into account Equation 29 (see Appendix I), it is possible to estimate also the work carried out during the indentation ($\lambda = 210$ nm and $F_L^{max} = 350$ nN from Figure 12 (D)); the obtained value is $U_0 = 12 \cdot 10^{-15}$ J. Finally, the growth rate can be calculated as $N_0 = U_0 N/A = 0.56 \cdot 10^{-12}$ J/s.

Ripple profiles obtained by numeric integration of Equation 7 and Equation 8 with these parameter values are shown in Figure 19 (A). The simulated ripples have an amplitude $A = 1.3$ nm and a periodicity of $\lambda = 231$ nm for an indentation rate $N = 100$ nm/s. Note that the indentation rate $N$ parameter used in the model can be in principle related with the load applied by the tip and their dependence ($N(F_N)$) has been reported to be approximately linear in experiments on polymers [86].

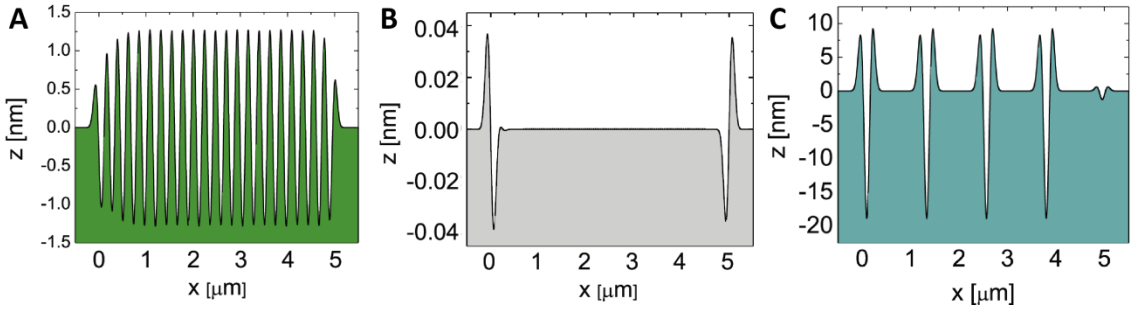


Figure 19. Surface profiles obtained by numeric integrations of Equation 7 and Equation 8 with lateral stiffness $k = 2$ N/m, a tip half-width $\sigma = 50$ nm, a scan velocity $v = 10$ μm/s and an indentation rate (A) $N = 100$ nm/s, (B) $N = 10$ nm/s and (C) $N = 250$ nm/s.

If $N$ is ten times lower, the ripple pattern disappears as observed in Figure 19 (B). In this case, the height of the side mounds and the depth of the indentation pit are too low to prevent lateral motion and the tip continuously follows the support. As a result, no ripples are formed and the surface remains almost unperturbed except for two hillocks at the borders of the scanned line. This mechanism has certain analogy with the transition from stick-slip to continuous sliding observed in atomic-scale friction when the normal force is reduced below a critical value [55]. On the contrary, when increasing the indentation rate up to $N = 250$ nm/s, the pattern is produced in two consecutive stick phases (Figure 19 (C)), resembling the profiles in Figure 14 (B) and Figure 18, where indentations are less overlapped. These simulations are in accordance with the observed experimental results when varying the applied load exerted by the tip.

Changes in amplitude and periodicity of the ripples upon systematic variation of indentation rate $N$, sliding velocity $v$ and lateral stiffness $k$ are shown in Figure 20. The obtained tendencies as a function of the $N$ and $v$ fully support the experimental results presented in Figure 13 (B-C) and Figure 15 (B-C) regarding the load and the scan rate dependence, respectively. In relation to the simulation of the effective spring constant $k$ variation, the period tendency is consistent with the dramatic increase of $\lambda$ reported when

polymer surfaces are heated about the glass transition temperature, which significantly reduces the material stiffness [64, 87].

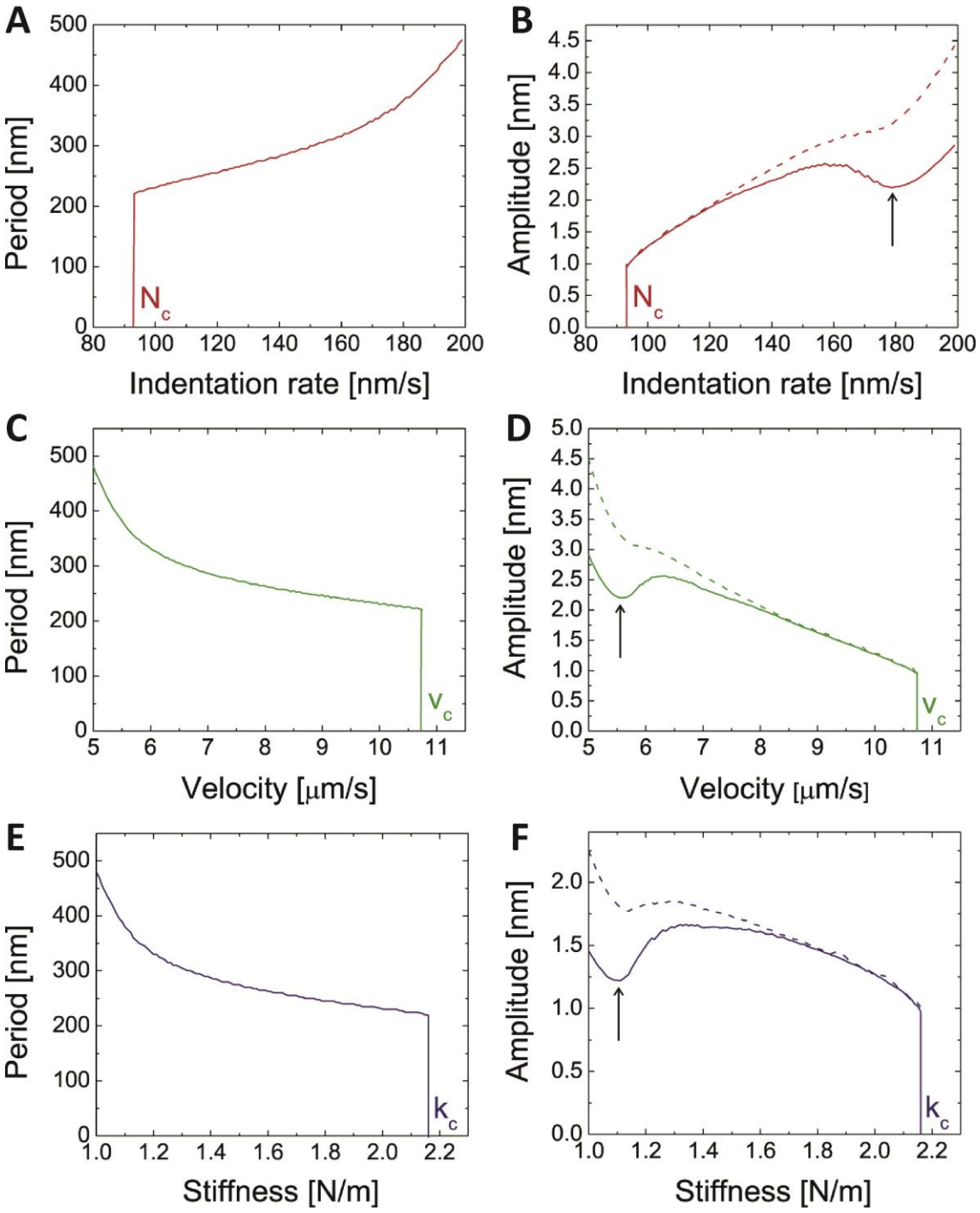


Figure 20. (A, C, E) Ripple periodicity as a function of the indentation rate $N$, the sliding velocity $v$ and the lateral stiffness $k$, respectively. (B, D, F) Ripple amplitude as a function of the indentation rate $N$, the sliding velocity $v$ and the lateral stiffness $k$, respectively. The rest of the parameters are kept fixed at the same values of Figure 19 (A). The vertical lines represent the critical values where ripples disappear. Dashed curves correspond to the maximum height of the surface profiles.

In addition, it is also observed that ripples appear only if $N > N_c$, $v < v_c$ and $k < k_c$, where the critical values correspond to a period $\lambda_c \approx 200$ nm, in agreement with the experimental results presented in Section 3.3, too. This size $\lambda_c$ of the trace left by an indentation represents

a strict lower bound for the ripple formation. Beyond these parameter critical values ($N_c$, $v_c$, $k_c$), the indentation rate is too low, the scan rate too high or the driving spring to stiff for the ripples to be formed, and the surface remains unchanged (Figure 19 (B)).

A simple criterion for estimating that critical values (with the other two parameters fixed) can be obtained as follows. Assuming the tip does not move laterally, the second derivative of the interaction potential at a time *t* with respect to the *x* at the tip location is

$$k_{int}(t) = 1.406\,\frac{N_0 t}{\delta^2}$$

Equation 9

This value has to be compared with the corresponding derivative of the parabolic spring potential, which is equal to *k*. According to the PT model, stick-slip is expected only if $k_{int}(t) > k$. Besides, it is important to notice that the order of magnitude of the time *t* at which the comparison can be done is $\delta$/v (time to form and overcome the first ripple). As a result, the approximate condition for ripple appearance is given by Equation 10:

$$k < 1.406\,\frac{N_0}{\delta v}$$

Equation 10

The critical values defined by this relation are consistent with those in Figure 20. For example, considering the values of $N_0$, *v* and $\delta$ in Figure 20 (E) and (F), the calculated value of $k_c$ is 1.57 N/m, which is slightly lower than the value obtained numerically (≈ 2.15 N/m). Moreover, it is noticeable that these values mark a sharp transition between two regimes: stick-slip (where ripples are formed) and wearless sliding (Figure 21), in contrast to the continuous transition that occurs in the case of atomic-scale friction [55].

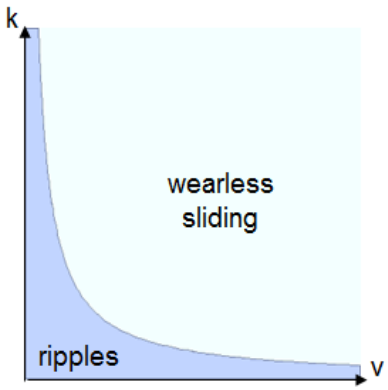


Figure 21. Transition from stick-slip to continuous sliding.

On the other hand, far enough from the critical values, the patterns are produced in two consecutive stick phases that are less and less overlapped. As a consequence and according to the model, the maximum height of the resulting profile (shown as dashed curves in Figure 20) differs from corrugation of the profile divided by two (shown with the continuous lines in the same figure). Furthermore, it is also possible to observe that this corrugation can even decrease in the regions indicated by the arrows, until the overlap between consecutive stick phases becomes negligible and series of well-separated "bumps" are left on the surface (Figure 19 (C)) in agreement with the experimental observations.

Finally, it is important to mention that, as a first step in the model, the indentation rate is assumed to be constant. However, indentation experiments on polyethylene terephthalate (PET) have shown that *N* decreases with the tip time of residence $t_{res}$ at a given location [88]. Figure 22 shows the experimental indentation depth as function of time when a load of 100 nN is applied by the tip on PS. The strain grows viscously at an exponentially

decreasing rate. This decay can be explained by the fact that the contact area continuously increases, so that the average pressure decreases as the tip sinks into the material. At a certain moment, the fraction of the contact area which gets plastically deformed will start shrinking and the indentation process will slow down. In this case, the time by which the penetration depth saturates $\tau$ is around 10 s. Nonetheless, this time is three orders of magnitude larger than the typical tip residence time $t_{res}$ (ms), meaning that *N* can be assumed constant as long as $v \gg \lambda/\tau \sim$ 10 nm/s, as in the present study.

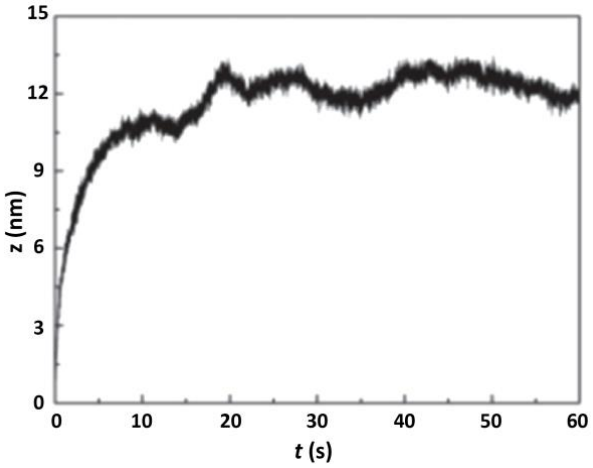


Figure 22. Indentation depth vs time measured when a tip is pushed against a PS surface by a normal force of 100 nN.

## 3.4.3. MODEL EXTENSION TO 3 DIMENSIONS

A 3D extension of the model described in Section 3.4.1 is needed for a precise comparison between the simulations and the experimental results regarding the load and the scan rate parameters. Furthermore, the spacing between lines influence in ripple orientation can only be supported within that 3D modeling.

This extension is being developed in collaboration with Iván Bailera and Dr. Juan Mazo from Institute of Material Science of Aragón.

In this case, the indentation profile consists in a volcano (Figure 23 (E)), centered at a given position $\overrightarrow{r_0}(t)$. The ratio $\zeta$ between the height of the material piled-up around the indentation pit and the pit depth is determined by

$$\int_0^\infty \left(-e^{-d^2/2\delta^2} + \zeta e^{-(d-2\delta)^2/2\delta^2}\right) \cdot 2\pi x \, dx = 0$$

Equation 11

considering that the total volume is conserved in the indentation and the distance *d(t)* is defined as $d(t) = |\vec{r} - \overrightarrow{r_0}|$. The solution of Equation 11 is the following one and the corresponding pattern is shown in Figure 23 (E):

$$\zeta = 0.1978 \approx \frac{1}{5}$$

Another improvement is the incorporation of a saturation condition in order the tip not to stop at a minimum. For that, a function that modulates *N* depending on the height is used and given by Equation 12. Its shape is inspired in Figure 22.

$$N = N_0 \, e^{-\frac{|h(x)|}{h_0}}$$

Equation 12

where: $h_0$ = 1.8.This value is adjusted by considering the appearance of ripples in 1D in the region corresponding to Equation 10.

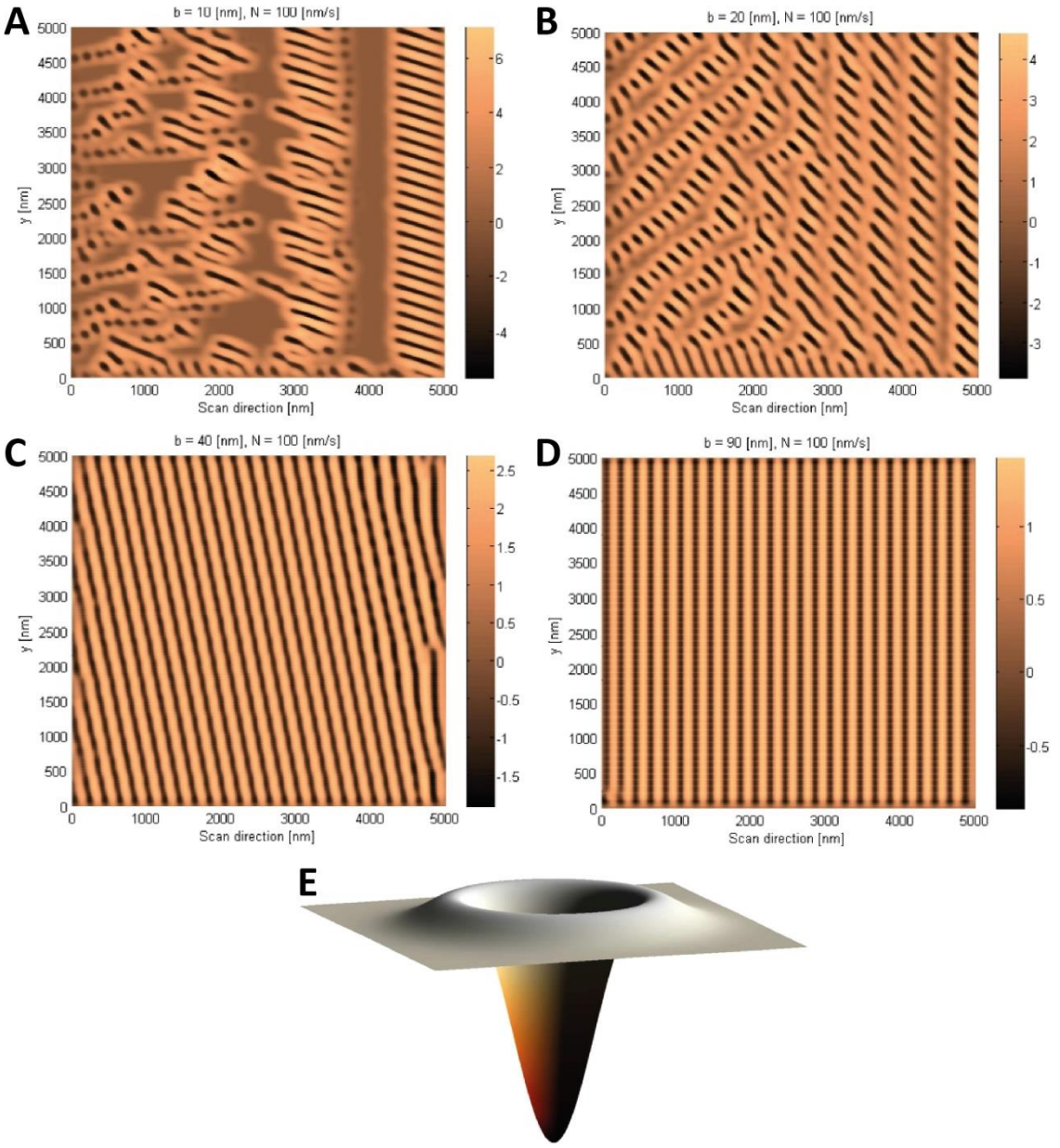


Figure 23. 3D simulation of ripples varying the distance between lines: (A) *b* =10 nm; (B) *b* = 20 nm; (C) *b* = 40 nm; (D) *b* =90 nm. $N_0$ = 100 nm/s. Unpublished work. (E) Tip footprint where the material piled-up and the indentation pit have the same volume.

Preliminary results of the extension of the model in three dimensions, considering a raster path, are shown in Figure 23 (A-D), where 3D ripples are clearly observed. In addition, boundary effects are also present in the right part of each image. According to the simulations,

changes in the distance between scan lines *b*, clearly affect the ripple orientation. Note that the obtained angle is not consistent with the experimental results in Section 3.3.3. This is possibly due to the fact that during the development of these first simulations, it is assumed that the tip apex moves up on a new scan line and, because of that, the material is pushed in the bottom-left direction and the ripples have other orientation. This problem is being considered in ongoing simulations.

# 3.5. CONCLUSIONS AND NEXT STEPS

In Chapter 3, we explore the general surface rippling phenomenon by, on the one hand, proposing a continuum model in one dimension and, on the other, by carrying out experimental work on solvent-enriched polystyrene thin films with a sharp AFM tip.

Ripple formation is the result of a stick-slip process with interesting analogies with atomic-scale friction. Four key parameters are pivotal in the model: the indentation rate *N*, the sliding velocity *v*, the lateral spring constant *k* and the tip width $\delta$, by introducing a variable interaction potential $U_{int}$, resembling the surface profile.

As a result, we observed that the periodicity and corrugation of ripple structures increase if the loading force (or indentation rate) is increased or the scan velocity is decreased when varying systematically those parameters in both experiments and numeric simulations based on our model.

Simulation also predicts that ripple amplitude and periodicity decreases when increasing lateral stiffness. Experimental confirmation will be required in this sense. However, the used of probes with different stiffness is not suitable enough for comparison because the effective spring constant *k* is the contribution of lateral spring constant of the cantilever and the lateral stiffness of both contact and tip. AFM experiments at different temperatures can contribute also to fully understand this behaviour.

On the other hand, both model and experiments conclude that the ripples disappear if the sliding velocity or the lateral contact stiffness increase, or the indentation rate decreases beyond critical values. This abrupt transition occurs when the ripple periodicity, which depends almost linearly on *N*, *v* and *k*, is twice as large as the tip apex. A simple criterion has been proposed to predict ripple appearance in terms of those parameters.

Nevertheless, quantitative detailed comparison between model and experimental evidences is hindered by the one-dimensional character of the model and the feedback-dependent relation between normal force and indentation rate.

For that reason, work is in progress to completely develop a 3D model in collaboration with Dr. Juan Mazo at the University of Zaragoza.

Furthermore, quantitative correspondence between period and material properties (i.e. shear modulus) will require the introduction of a temperature dependent damping term in the model, representing the viscous properties of the material.

The work described in this Chapter demonstrates the possibility of controlling the periodicity and the amplitude of the pattern achieving certain control over the rippling process on polymers at the nanoscale. This improvement could lead to an increasing interest in this phenomena not only in nanolithography and but also for some long-term technological applications such as gratings for nano-optics.

Finally, even though this research has been carried out on a specific polymeric surface, the same approach, with a proper indentation law, could be used to describe the evolution of other systems where similar rippling process are conducted. For example, this model system could contribute to a better understanding on the so-called contact ageing phenomena. And, on larger scales, it would be also useful to study phenomena such as the rippling of unpaved roads, sky slopes and rail tracks.

# Chapter 4

# SUPPRESION OF WEAR BY ULTRASONIC VIBRATIONS

# 4. CONTROL OF WEAR BY ULTRASONIC VIBRATIONS

In Chapter 4, the effect of out of plane ultrasonic vibrations on friction and wear of polymers on the nanoscale is investigated. For this purpose, the same system described in Chapter 3 is selected as ripple formation is particularly suitable for a quantitative characterization of these effects.

Firstly, a concise review on the concept of ultrasonic waves and their used for friction and wear reduction on the different scales is presented. Secondly, the key parameters considered in this study and the home-built set-up used for the calibration of the excitation amplitude of the piezoelectric transducer are detailed. Finally, the influence of the frequency and the excitation amplitude of the ultrasonic vibrations on wear and friction mechanisms is presented and their effect are discussed. Also in this case, a remarkable analogy with "tuning" stick-slip on crystal surfaces via ultrasonic vibrations can be recognized.

This part of the thesis was performed in close collaboration with Dr. Reinhold Wannemacher, who is the expert in nanoacoustics at IMDEA Nanoscience.

## 4.1. MOTIVATION AND BACKGROUND

### 4.1.1. NANOWEAR AND SURFACE RIPPLING ON POLYMERS

Wear, at any scale, is one of the main causes for component damage and subsequent failure of machines and devices. Thus, its mitigation by appropriate material choice, coating, surface design and lubrication is of high economic importance.

In the case of the nanoscale, the surface area-to-volume ratio considerably increases becoming a cause of serious concern from a tribological point of view and the limiting factor to broad-impact of the field on daily life. In addition, traditional lubricants cannot be used since their viscosity dramatically increases when molecular chains are confined into nanometer-sized interstices [89].

On the other hand, the use of polymeric materials constantly increases in nanotechnology. However, these materials are softer than metallic and inorganic ones, and, therefore, they are easier to deform and wear off.

The formation of ripples structures on polymers, presented in Chapter 3, can be considered as the initial stage of wear processes [90]. Thus, the same system with PS thin films can be employed to investigate wear occurrence on polymer surfaces on the nanoscale by means of an AFM.

### 4.1.2. ULTRASONIC WAVES FOR FRICTION REDUCTION

Ultrasonic vibrations are defined as mechanical vibrations of frequencies from 20 kHz up to GHz. They have a wide range of applications in many different fields, for example, non-destructive testing of materials, cleaning, ranging (sonar) and medical imaging.

In addition, on the macroscale ultrasounds have been employed for many years to modify frictional behaviour to reduce wear and undesired acoustic emission related to friction in industrial processes [91-94]. The first work on the influence of vibrations on static friction was done by Fridman and Levesque in 1959 [91], who studied oscillations of several frequencies (6-42 kHz) normal to the contact plane, finding a decrease of approximately 100 % in the static friction coefficient with increasing amplitude. Moreover, the effect of out-of-plane mechanical vibrations not only in friction but also in wear was also investigated on the macroscale [95, 96].

The simplest examples of that effects are vibration compactors and plates as well as oscillating conveyors [4]. Furthermore, high frequency oscillations are utilized to influence friction in metal working such as assembly, wire drawing and cutting [97, 98]. In addition to metal forming processes, ultrasonic vibrations are used to control frictional forces in technical devices, such as ultrasonic motors for cameras and objectives, where the influence of that oscillations on the sliding friction is of utmost importance [99].

On the microscale, on the other hand, Hesjedal and Behme [100] employed surface acoustic waves (200 kHz-3GHz) on the surface of hard samples (i.e. quartz, GaAs or Au) to demonstrate that reduction in friction results only from modulations in the normal direction to the surface. Dinelli *et al.* [101] found, in a pioneer work, that friction disappearance is due the fact that contact breaks during vibration, but the frictional force is reduced even before the loss of contact.

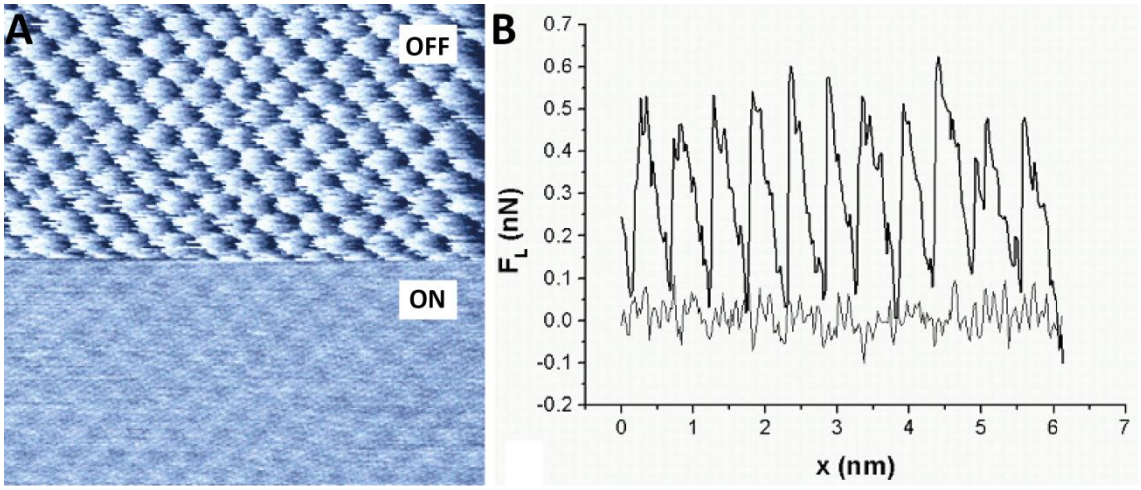


Figure 24. (A) Lateral force map (6.2 nm x 6.2 nm) on an atomically flat NaCl (100) surface at a static load of 2.73 nN. In the lower part of the image an ac voltage of frequency 56.7 kHz with a peak-to-peak amplitude of 3 V is applied. To enhance the atomic contrast in the superlubric regime, the whole image is flattened line by line. (B) Representative scan lines from the upper part (thick line) and the lower part (thin line) in (A). Profiles are not flattened. Reproduced from [102].

More recently, friction on the atomic scale was also studied, in ultrahigh vacuum (UHV) and ambient conditions, by Socoliuc and coworkers [102-104]. A significant reduction of friction was observed when bending mechanical resonances between the AFM tip and alkali halide surfaces were excited at lower frequencies (20-300 kHz). Figure 24 illustrates the transition from atomic stick-slip motion to continuous sliding in such conditions. Following this strategy, prevention of abrasive wear of silicon tips sliding over several hundred meters was also demonstrated in [105].

# 4.2. KEY PARAMETERS INVOLVED IN THIS WORK

In the present study, external mechanical vibrations are induced by a highly damped piezoelectric transducer coupled to the sample using a set-up similar to the AFAM one explained in Section 2.2.4.1 and shown in Figure 25. An external function generation (model DDS 4030, PeakTech) supplies a sine signal with a excitation amplitude ($A_{exc}$) at frequencies around the lowest bending resonance frequency of the cantilever in contact ($f_{res}$) with the PS sample (prepared as in Section 3.2). In that way, the piezoelectric transducer is driven and moves vertically together with the sample, producing a vibration amplitude ($A_{vib}$) in the cantilever that can be measured by the AFM photodiode.

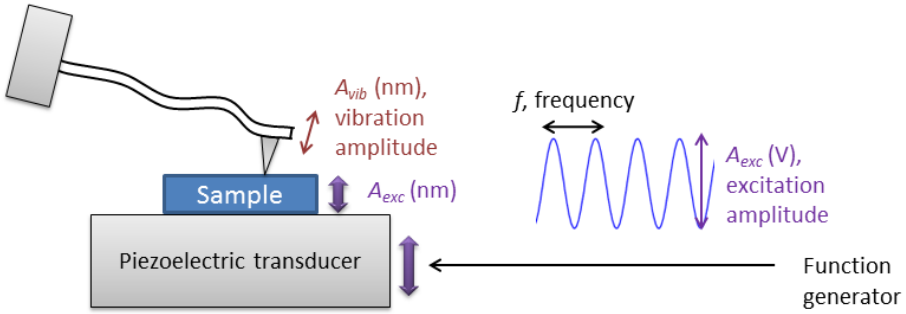


Figure 25. Scheme of the set-up and key parameters considered in the present study.

## 4.2.1. CONTACT RESONANCE FREQUENCY ($f_{res}$)

The contact resonance frequency ($f_{res}$) is the resonance of the cantilever with the tip in contact with the sample.

Due to the fact that the tip-sample forces in the contact area influence the mechanical boundary conditions of the cantilever, the value of the resonant frequencies in contact increase considerably compared to the free cantilever (around 5-6 times for the first bending mode). In addition, the contact resonance frequency depends, among other parameters, on the stiffness of the tip-sample contact, on the contact radius and on the geometry of the cantilever. Figure 26 (A) and (B) show how the contact resonance frequency, as measured on our PS surface, also varies with the chosen static load and with the amplitude of the induced vibration. The contact resonance peak, as seen in the vertical deflection, is plotted for different excitation amplitudes and for two static load of (A) 26 nN and (B) 442 nN. It is clear that the peak shifts to higher frequencies with the increasing load. At the same time, the width of the resonance curves decreases with increasing load and decreasing vibration amplitude.

Furthermore, it is possible to observe that for higher amplitude values, the peaks become asymmetric and shift, showing the typical nonlinear behaviour of these oscillators. All these results are in accordance with previous reports [36, 37, 106].

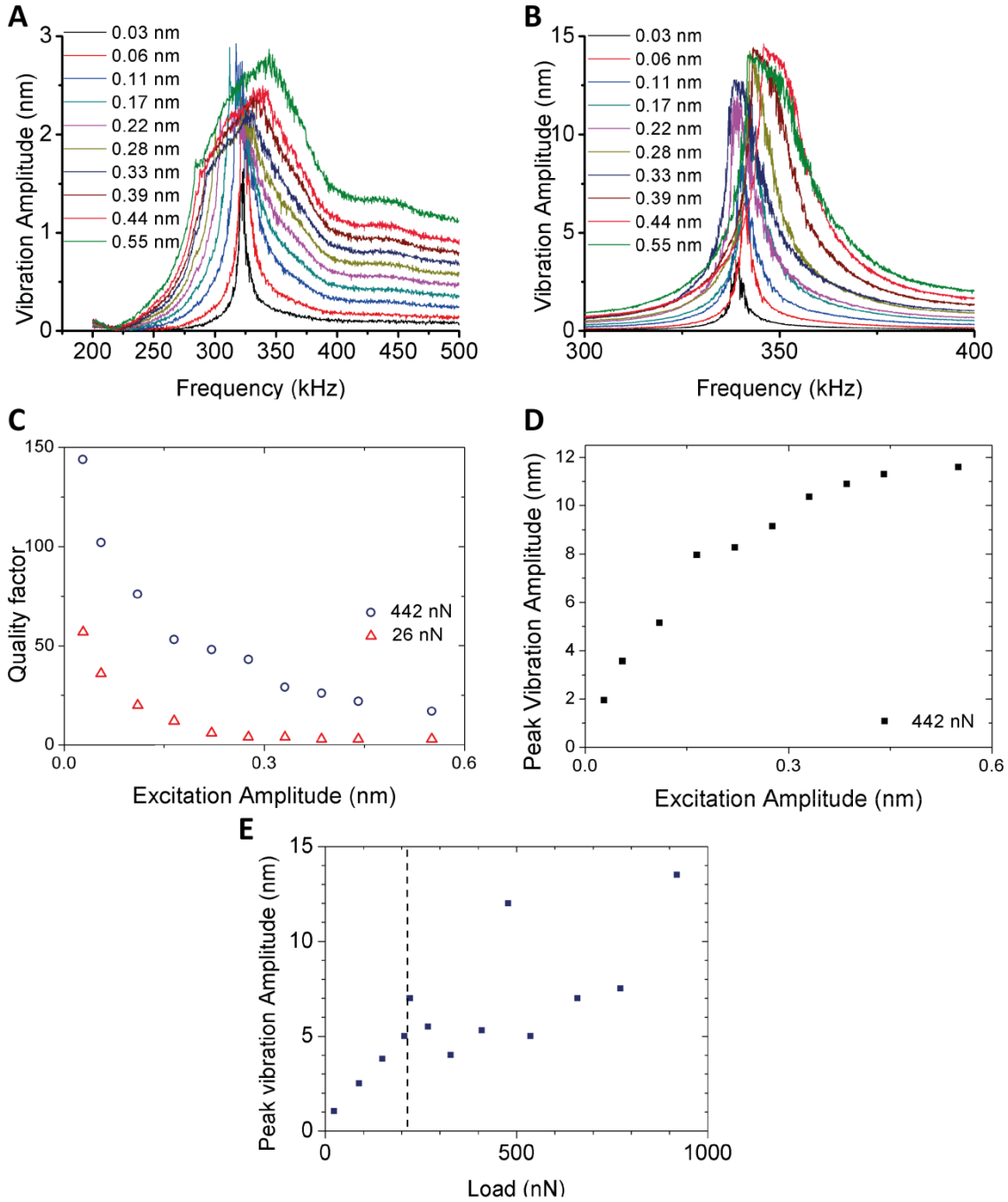


Figure 26. Contact resonance spectra at different excitation amplitudes on the PS sample measured when the applied load is (A) 26 nN and (B) 442 nN. The free resonance of the cantilever is 71.6 kHz. (C) Quality factor $Q$ vs $A_{exc}$ at two different loads. (D) Peak vibration amplitude, obtained using the standard static calibration of vertical deflection, as a function of the $A_{exc}$ at 442 nN. (E) Peak vibration amplitude at $A_{exc}$ = 0.55 nm versus the load.

On the other hand, the peak quality factor ($Q$) decreases with the increasing $A_{exc}$, as shown in Figure 26 (C), regardless of the load.

## 4.2.2. EXCITATION AMPLITUDE ($A_{exc}$)

The excitation amplitude ($A_{exc}$) induced by the function generator in Volts can be converted into the real transducer movement in nm by performing an absolute calibration of the piezoelectric transducer. This calibration is done by means of a home-built laser Doppler vibrometer [107] developed by Dr. Reinhold Wannemacher. This technique (Figure 27) allows the measurement of solid surface velocities based on the Doppler shift of the frequency of the light backscattered from the moving object, following the Equation:

$$\Delta f = \frac{2\,{}^{v}/_{c}}{1+{}^{v}/_{c}} f \approx \frac{2v}{\lambda}$$

Equation 13

where: $\Delta f$ = Frequency Doppler shift of the light backscattered from the moving object

$v$ = velocity component normal to the surface

$\lambda$ = Optical wavelength

The beam of a 632.8 nm HeNe laser is split into a reference beam and a beam which is firstly diffracted by an acousto-optic modulator (AOM), whose carrier frequency is 80 MHz and, secondly, reflected by the sample. The frequency modulation imposed on the light by the vibration of the reflecting surface is shifted down to measurable frequencies by interfering the reflected beam with the reference one at the photodetector, using a beam splitter as shown in Figure 27.

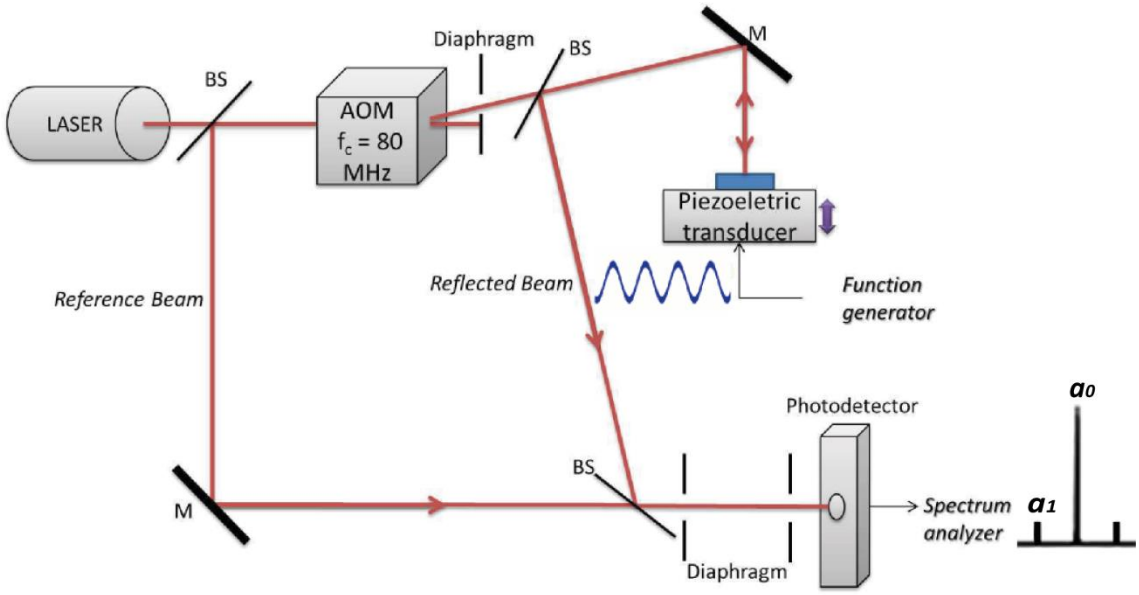


Figure 27. Laser Doppler velocimetry set-up used for calibrating the out-of-plane excitation amplitude of the sample surface when excited by the piezoelectric transducer. AOM, Acousto-optic modulator; BS, Beam Splitter; M, Mirror.

The AOM in one of the beams shifts the modulation to its carrier frequency and allows both sidebands of the frequency-modulated signal to be observed when the electric signal from the photodiode is Fourier-transformed (Figure 28 (A)).

Moreover, the amplitude of the vibration can be calculated from the ratio between the sideband and carrier amplitudes ($a_1$ and $a_0$, respectively) in the FFT of the signal:

$$\left|\frac{a_1}{a_0}\right| = \left|\frac{J_1(\beta)}{J_0(\beta)}\right|$$

Equation 14

where: $a_1$, $a_0$ = the amplitude of the sidebands and the carrier, respectively.

$J_1$, $J_0$ = Bessel functions of the first kind and $\beta$ is the modulation index. The relation between the ratio of the Bessel functions and $\beta$ is shown in Figure 28 (B) [108].

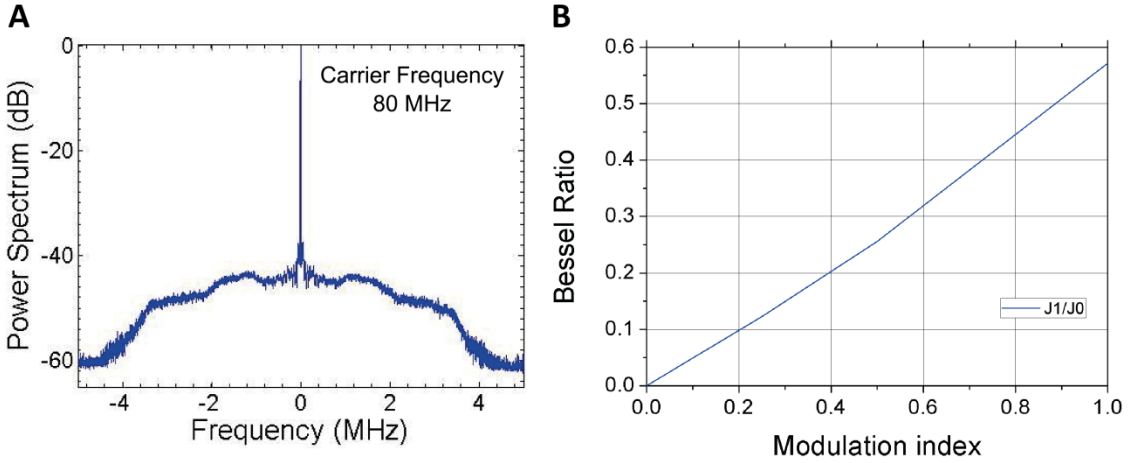


Figure 28. (A) Transducer response measured by the home-built laser Doppler vibrometer. The excitation frequency is scanned from 1 kHz to 5 MHz and the output of the photodiode is Fourier-transformed to produce the power spectrum of the interference signal at each frequency step. The drive amplitude is 10 $V_p$ and the carrier frequency of the AOM is 80 kHz. (B) Bessel ratio ($J_1/J_0$) vs modulation index.

The modulation index $\beta$, on the other hand, is the ratio between the frequency deviation, $\Delta f$, and the frequency of vibration of the piezoelectric transducer, $f_m$:

$$\beta = \frac{\Delta f}{f_m} = \frac{2\,{}^{v_0}/_{\lambda}}{f_m} = \frac{4\pi x_0}{\lambda}$$

Equation 15

where $v_0$ = velocity component normal to the surface = 2 $\pi f_m$ $x_0$

$x_0$ = Surface vibration amplitude (nm) = $A_{exc}$ (nm)

By taking into account the previous Equation and only considering the first sidebands due to the fact that, in our case, the modulation index turns out to be small, piezoelectric transducer can be accurately calibrated. The calibration yields a peak excitation amplitude of 0.55 ± 0.05 nm for a peak drive voltage of 10 V. The error results from the unequal amplitudes of the lower and upper sidebands used for calibration. It is also confirmed that $A_{exc}$ of the piezoelectric transducer is proportional to the applied ac voltage as shown in Table 2. Besides, $A_{exc}$ at a given drive voltage does not vary within the error of measurement in the frequency range used for the experiments.

Table 2. Piezoelectric transducer calibration.

| $A_{exc}$ ($V_p$) | $A_{exc} = x_0$ (nm) |
|---|---|
| 0.0 | 0.00 |
| 0.5 | 0.03 |
| 1.0 | 0.06 |
| 2.0 | 0.11 |
| 3.0 | 0.17 |

| | |
|---|---|
| 4.0 | 0.22 |
| 5.0 | 0.28 |
| 6.0 | 0.33 |
| 7.0 | 0.39 |
| 8.0 | 0.44 |
| 10.0 | 0.55 |

### 4.2.3. VIBRATION AMPLITUDE ($A_{vib}$)

The vibration amplitude ($A_{vib}$) can be determined by using the standard static calibration of the vertical tip deflection instead of an accurate interferometric calibration of the cantilever vibration. This approximation is correct because the cantilever deflection is almost entirely due to the deformation of the sample for the following two reasons. On the one hand, under conditions of resonance, the vibration amplitude is much larger than the excitation amplitude. And, on the other hand, because the elastic modulus of silicon (~160 GPa [109]) is very large compared to the one of PS (about 3.5 GPa [110]).

In Figure 26 (D) it is possible to observe how the $A_{vib}$ rises with the excitation amplitude and saturates at higher drive amplitudes at about 11 nm for a load of 442 nN. Moreover, it is interesting to observe that, at the contact resonance, $A_{vib}$ corresponds to a normal velocity amplitude on the order of several millimeters per second. For example, considering $f_{res}$ = 360 kHz and $A_{vib}$ = 10 nm, the normal velocity $v = 2\ \pi\ f_{res}\ A_{vib}$ = 23 mm/s, which is three orders of magnitude larger than the scan velocity of the experiments (10 μm/s).

Finally, the measured vibration amplitudes at the maximum excitation amplitude employed in the experiments ($A_{exc}$ = 0.55 nm) initially increases linearly with the load as shown in Figure 26 (E). However, at values exceeding ~200 nN, they scatter significantly. This behaviour could be attributed to the onset of plastic deformation, which implies hysteresis and, therefore, dependence of the response on the history of the sample under the tip.

## 4.3. INFLUENCE OF ULTRASONIC VIBRATIONS

The first experiment of this set (Figure 29) shows how the out-of-plane ultrasonic vibrations have a clear effect on wear of the PS film, in the sense of ripple formation, and friction between the tip and the sample, even for small transducer oscillation amplitudes below 1 nm.

In the upper part of the image, where no mechanical vibrations are applied, the typical ripple pattern is observed. However, the ripples immediately disappear when, during the acquisition of the image, the piezoelectric transducer coupled to the sample starts vibrating vertically with a peak amplitude $A_{exc}$ = 0.55 nm (10 $V_p$ applied ac voltage) at a frequency equal to the system resonance frequency in contact (Figure 29 (A) and (C)). At the same time, friction is remarkably reduced by a factor of around 3, as observed in Figure 29 (B) and the corresponding profile in Figure 29 (D).

At this point, it is important to notice that surface modification in the form of ripple formation can be considered as a pre-stage of abrasive wear [111]. Thus, it is expected that

abrasive wear will be also reduced by means of external vibrations. However, this particular regime of even higher normal forces has not been studied systematically in this thesis.

Since it is demonstrated that out-of-plane ultrasonic vibrations influence wear and friction of the system, the effect of excitation frequency and amplitude of those vibrations is investigated in detail in the following Sections.

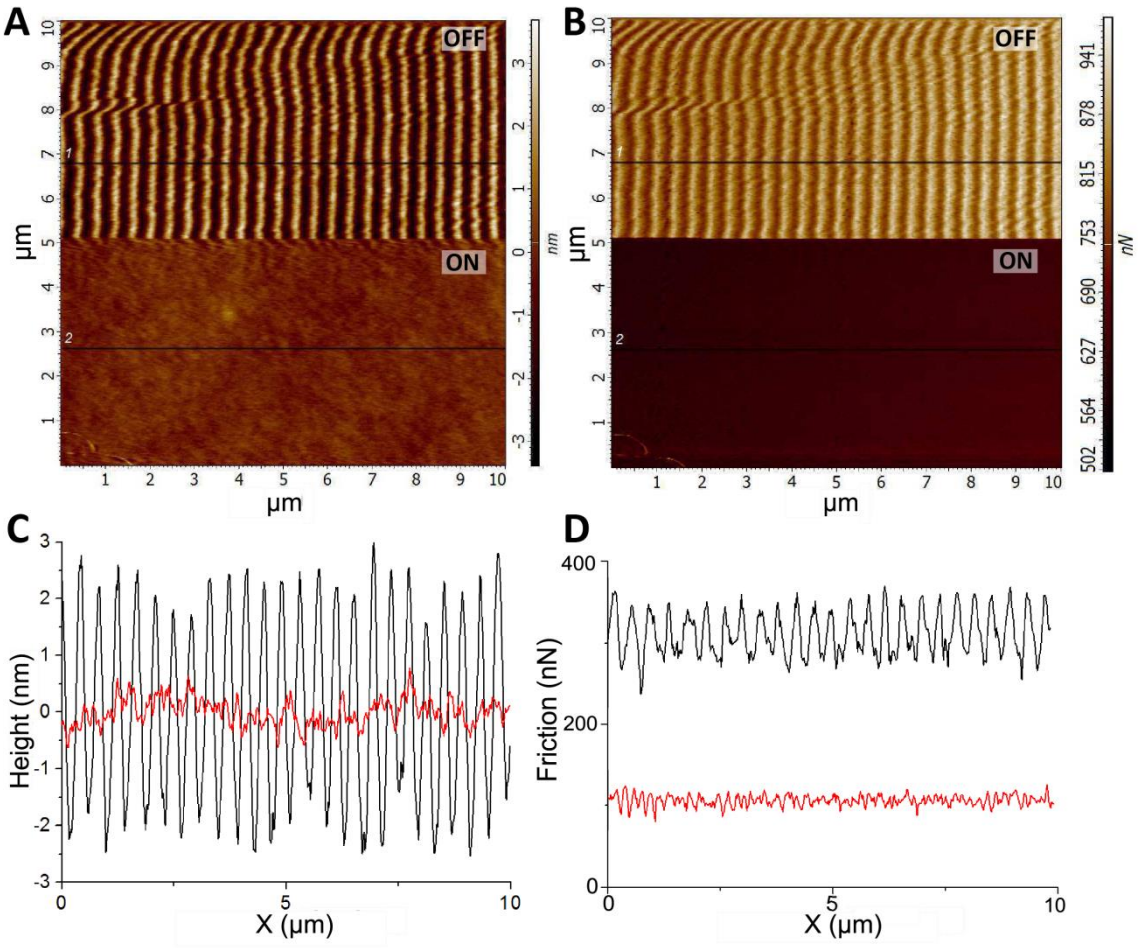


Figure 29. (A) Topography and (B) lateral force (retrace) while scanning a PS thin film with an AFM tip in contact mode (static load of 1378 nN, scan rate of 10 µm/s and distance between lines of 20 nm). (C) and (D) Profiles corresponding the black lines in (A) and (B). An ac voltage of a peak amplitude 10 $V_p$, corresponding to a peak excitation amplitude of 0.55 nm, is applied to the transducer while scanning in the lower part of the images at a resonance frequency in contact of 366 kHz (red profiles). The drive voltage is zero while acquiring the upper part of the images (black profiles).

### 4.3.1. EXCITATION FREQUENCY INFLUENCE

The effect of the out-of-plane vibration frequency is studied by acquiring AFM images of pristine PS thin film areas while sweeping the frequency around the resonance frequency in contact of the system, maintaining the rest of the parameters (load, scan rate and excitation amplitude) constant.

Figure 30 (A) and (B) show the topography and the lateral force, respectively, obtained while inducing linearly upward and downward frequency sweeps (from 350 to 370 kHz) in the vicinity of contact resonance frequency $f_{res}$ = 362 kHz with a peak amplitude of 0.28 nm, which corresponds to a drive voltage of 5 $V_p$. It is possible to observe that, on the one hand, the

ripples and, hence, the wear becomes less pronounced or even disappear at the contact resonance frequency depending only on the drive voltage. On the other hand, for vibration frequencies away from the resonance one, the ripple corrugation is slightly smaller than in the case of no external vibrations. In addition, darker areas, corresponding to lower friction between the tip and the sample, appear in the lateral force image in a range of frequencies $\Delta f$ ≈ 8 kHz around the $f_{res}$.

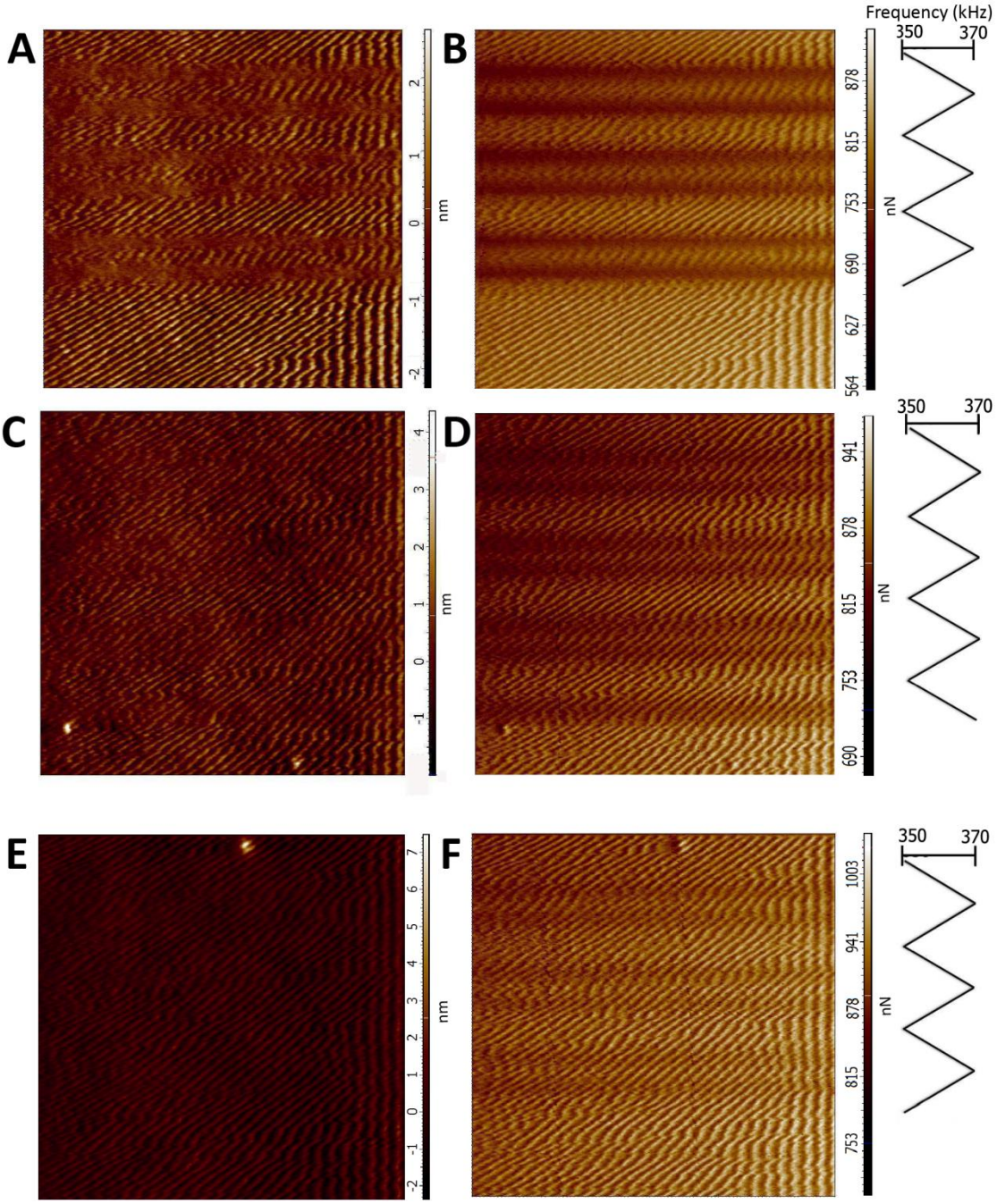


Figure 30. (A) Topography and (B) corresponding lateral force (retrace) when scanning in contact while sweeping the external vibration frequency between 350 and 370 kHz (contact resonance frequency is 362 kHz) with a peak amplitude of 0.28 nm (5 $V_p$). (C) and (D) Same as (A) and (B) but for a $A_{exc}$ = 0.22 nm (4 $V_p$). (E) and (F) Same as (A) and (B) but for a $A_{exc}$ = 0.14 nm (2.5 $V_p$). The diagrams on the right-hand size of the figures indicate the actual vibration frequency during the scan. At the beginning and at the end of the image, no vibration is induced. Applied static load of 984 nN. Frame sizes: 10 x 10 $\mu m^2$.

Furthermore, the same images measured when using an $A_{exc}$ = 0.22 nm and $A_{exc}$ = 0.14 nm are shown in Figure 30 (C-D) and (E-F), respectively at an applied static load of 984 nN. At the lowest $A_{exc}$, ripples and wear appear during the whole frequency sweep. However, slightly darker areas, corresponding to a friction reduction of about 9 % with respect to the one without vibrations, are observed in the lateral force image when the frequency is in the range of 4 kHz around the contact resonance frequency. On the other hand, for the intermediate value of the excitation amplitude ($A_{exc}$ = 0.22 nm), ripples become less pronounced and much darker areas appear in the lateral force image, with a friction reduction of around 15 %.

According to the previous results, the effect of the contact resonance frequency on wear and friction consists only in the resonance enhancement of the vibration amplitude. Therefore, it is expected to see wear (ripples) and friction reductions at other drive frequencies but at correspondingly higher drive amplitudes.

### 4.3.2. EXCITATION AMPLITUDE INFLUENCE

The influence of the excitation amplitude ($A_{exc}$) induced on the sample surface, on both the ripple formation and friction, is also investigated.

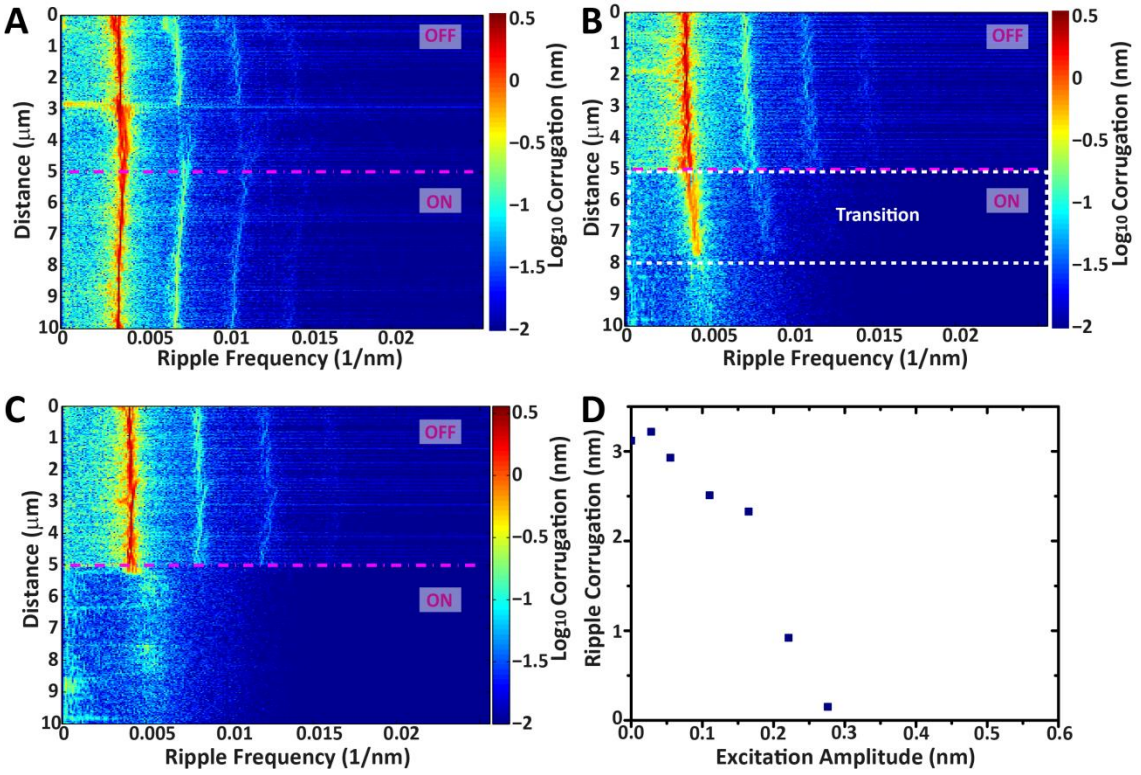


Figure 31. (A) FFT of ripple corrugation along the fast scan direction (colorbar in logarithmic scale, in nm) for $A_{exc}$ = 0.03 nm (0.5 $V_p$) at the resonance frequency in contact. Vertical axis corresponds to the AFM slow scan direction. (B) Same for $A_{exc}$ = 0.22 nm (4 $V_p$). (C) Same for $A_{exc}$ = 0.55 nm (10 $V_p$). (D) Corrugation as a function of the induced vertical peak $A_{exc}$ from 0 nm (no vibration) to 0.55 nm (10 $V_p$) at the contact resonance frequency. Applied static load in all the cases is 442 nN. Magenta dashed lines in the slow scan direction show the scan line where the vibration is turned on. In each image, vibration is induced at the $f_{res}$ obtained for the specific load and the chosen $A_{exc}$.

The same experiment shown in Figure 29, where the mechanical vibrations at the $f_{res}$ are induced only in the second part of the image, is repeated at different $A_{exc}$. In order to get a quantitative picture of excitation amplitude effect on ripple formation, the line by line Fast

Fourier Transform (FFT) of the topography is calculated. The results of such an analysis are shown in Figure 31 (A-C). Here, the corrugation (ripple amplitude) is defined as the magnitude of the lowest-order Fourier component of the rippled topography, as elsewhere in the present thesis.

At low $A_{exc}$, there is no significant change in the ripple periodicity and corrugation along the scan whether or not the vibration is present, as demonstrated in Figure 31 (A). On the other hand, at intermediate $A_{exc}$, it is possible to observe a transition stage, which starts when the vibration turns on (Figure 31 (B)). During this period, the ripples become less pronounced and their periodicity and corrugation decrease. Furthermore, the duration of that stage is shorter when $A_{exc}$ is larger. This transition from stick-slip behaviour to smooth sliding after turning-on the ultrasounds can be explained due to the overlapping phenomena with previous scan lines where ripples already exist, since distance between lines is only 20 nm. This overlap stabilizes the stick-slip movement until the corrugation is gradually reduced and the ripples vanish. Finally, at high $A_{exc}$ (Figure 31 (C)) ripples disappear as soon as the vibration starts. In fact, it is interesting to notice that ripples fade off immediately after applying the vibration if the plateau value of about 10 nm for the vibration amplitude is reached, as shown in Figure 26 (D).

Moreover, the ripple amplitude is plotted as a function of $A_{exc}$ at the contact resonance frequency in Figure 31 (D). The values are obtained by calculating the one-dimensional FFT of the AFM topography images. The Figure shows that the corrugation decreases up to $A_{exc}$ = 0.28 nm (5 $V_p$), where the ripples disappear in the case of the chosen load of 442 nN.

At this point in order to investigate the effectiveness of out-of-plane ultrasonic vibrations for reducing wear on the nanoscale, an area previously scanned in contact with and without vibrations is imaged using Tapping® mode.

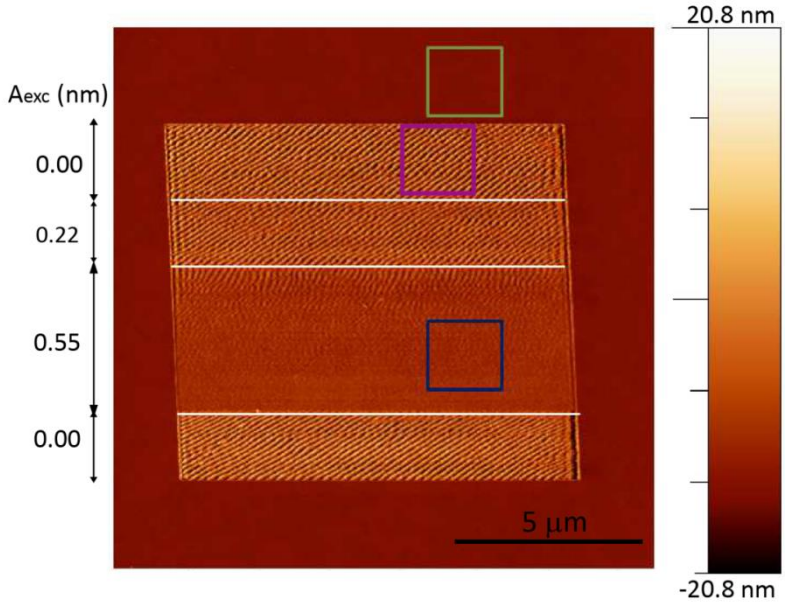


Figure 32. AFM topography, measured in Tapping® mode, after scraping the PS thin film in contact mode at a static load of 156 nN. White lines point the borders of the scanned regions where different excitation amplitudes ($A_{exc}$ = 0 nm, 0.22 nm and 0.55 nm) are induced to the piezoelectric transducer, as indicated on the left. PS molecular $M_w$ = 248000 g/mol. Color squares indicate the 2 x 2 $\mu m^2$ area from where RMS roughness is calculated.

Figure 32 reveals, in accordance with Figure 29, that simultaneous application of an excitation amplitude $A_{exc}$ = 0.55 nm at the contact resonance frequency completely suppresses ripple formation while scanning in contact mode with the AFM tip. The root-mean-square roughness (RMS) is determined as an indirect way to quantify the wear, evidenced by the ripple formation. Three 2 x 2 $\mu m^2$ areas (indicated in Figure 32) are chosen for this purpose regarding the different $A_{exc}$. The RMS roughness for the area where external vibrations at $A_{exc}$ = 0.55 nm were previously applied is 1.35 nm. Even though, this value is higher than the one observed in the pristine area (0.32 nm); both of them are very low if they are compared to the one where no vibration at all was applied (8.34 nm).

Furthermore, in Figure 32 it is possible to observe that the average height of the previously scanned areas is slightly higher than the pristine one. However, this increment is contrary to the expectations based on the assumption of abrasive wear. Besides, abrasive removal of material by the tip should be also evidenced by a pile-up of material at the borders of area previously scanned in contact mode. This apparent increase in height can be ascribed to surface roughening after scanning in contact, leading to interactions between the tip sidewalls and the rough sample.

The influence of $A_{exc}$ on friction is also studied in Figure 33. The friction force averaged over all the area diminishes with the increasing $A_{exc}$ up to $A_{exc} \approx$ 0.33 nm (6 $V_p$) and levels off at a value of 150 nN, corresponding to a friction reduction of 42 % compared to the one without out-of-plane vibrations. Regarding the friction coefficient, it decreases from 0.57 to 0.34 in the plateau. The latter value is consistent with values reported on the macroscale for silicon/polystyrene systems in the absence of external vibrations [112].

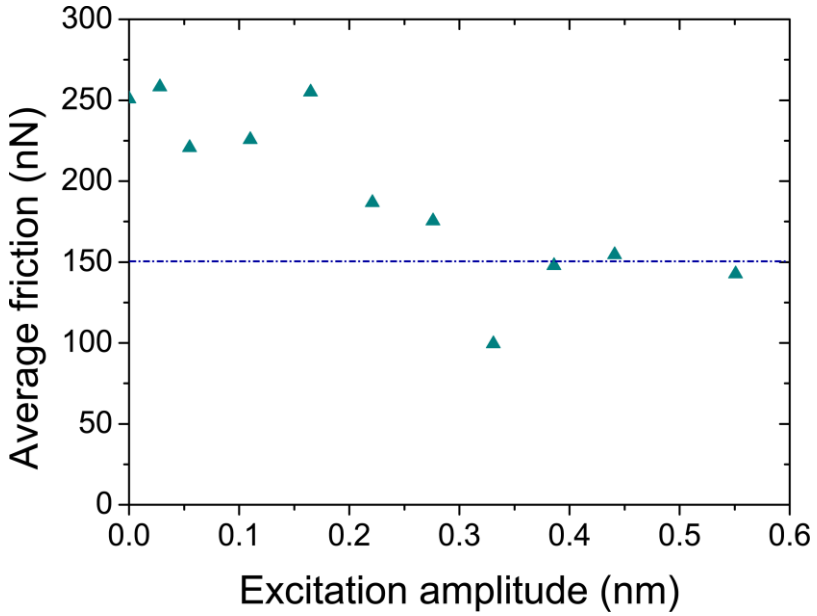


Figure 33. Average frictional force as a function of $A_{exc}$ from 0 nm (no vibration) to 0.55 nm (10 $V_p$) at the contact resonance frequency for the chosen $A_{exc}$ and load. Applied static load is 442 nN.

The reduction of the rippling effect when increasing $A_{exc}$ has again some interesting analogies with the friction reduction observed in wearless stick-slip on the atomic scale while applying external vibrations by force modulation [102]. This effect has also been interpreted in the case of hard materials [103] assuming that the tip-surface interaction changes periodically with the time according to the excitation signal.

In this way, the energy barriers that the tip has to overcome while moving on a crystal surface are reduced. As a consequence, the amplitude of the stick-slip pattern also decreases, as well as the related friction force.

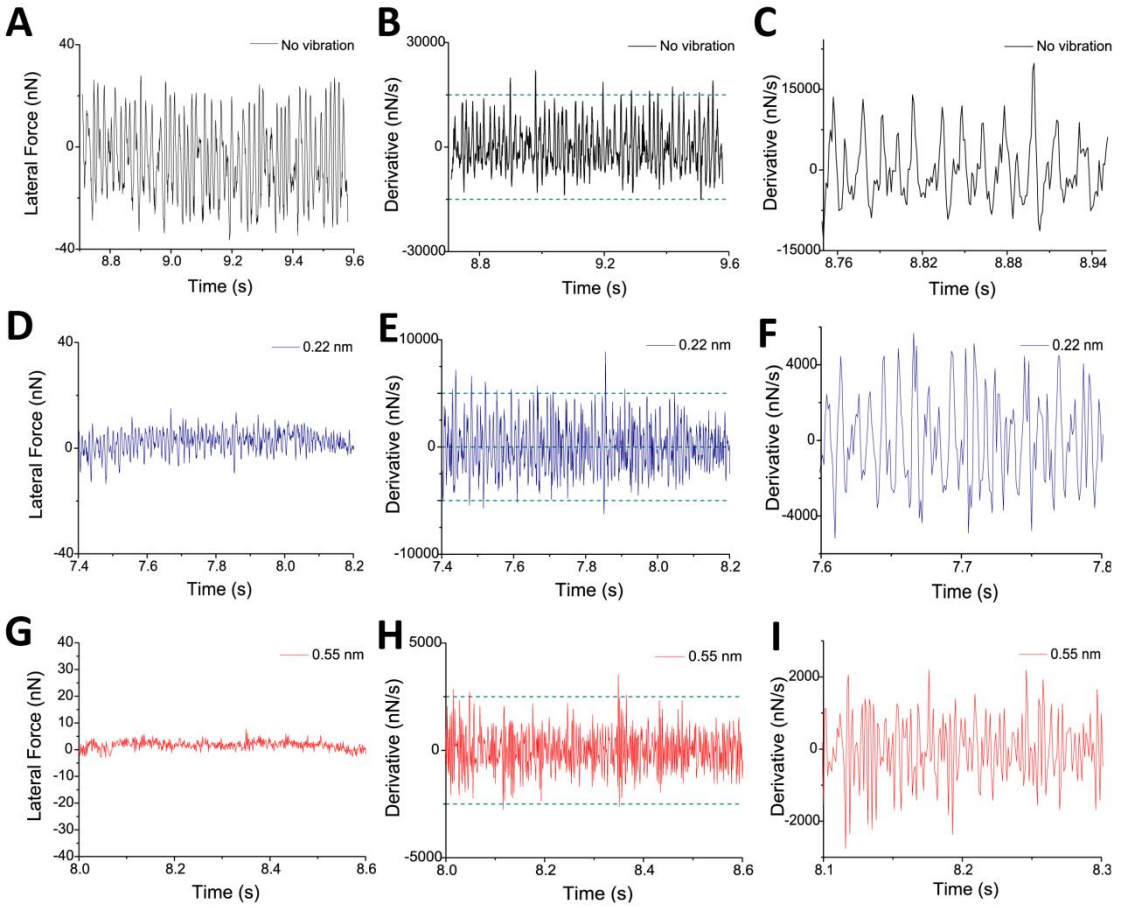


Figure 34. (A) Lateral force raw signal, (B) corresponding derivative of the lateral force and (C) a zoom of (B) where no vibration is applied. (D) (E) and (F) Same for $A_{exc}$ = 0.22 nm (4 $V_p$). (G) (H) and (I) Same for $A_{exc}$ = 0.55 nm (10 $V_p$). Applied static load of 156 nN.

In order to identify the stick-slip movement in the present case, the lateral force signals obtained while scanning in contact mode in the presence and absence of vibrations are recorded. Figure 34 (A), (D) and (G) show the lateral force signal obtained during scanning in contact mode at three increasing values of $A_{exc}$. It is seen that the range of lateral force variation decreases with the increasing excitation amplitude. However, the stick-slip mechanism is not clearly evident from those signals. To clarify that, the lateral force derivatives and a zoom of them are shown in Figure 34 (B-C), (E-F) and (H-I). The derivatives of the signals exhibit significant asymmetry when no vibration is applied. In addition, this asymmetry disappears with the increasing excitation amplitude due to the absence of stick-slip.

According to Socoliuc *et al.* [103], the normal force increases and decreases cyclically when the transducer vibrates up and down; leading to a premature slip of the tip in the case of rigid substrates. However, on a compliant polymeric material, the surface profile created by the tip is expected to partially follow the excitation amplitude, but only while the tip sinks into the polymer. On the contrary, when the tip retracts from the surface during the oscillation, the load and, hence, the friction are significantly reduced. This is because of the partly plastic response of the sample; which, in addition, facilitates the slip of the tip. Besides, according to force-distance curves experiments on pristine PS thin films, it is possible to exclude important adhesion contributions to the tip-sample interaction during the retraction process. As a result, the surface damage occurring in the oscillation cycle is reduced, which explains why the ripple corrugation decreases when the $A_{exc}$ increases. Furthermore, the friction force diminishes and levels off at a value determined by the load and the excitation amplitude.

A full theoretical analysis of the wear reduction by out-of-plane mechanical vibrations considering the specific material properties of the sample is beyond the goal of this thesis. Nonetheless, polystyrene plasticity is an important factor affecting the observed experimental results. Plastic behaviour below the glass transition temperature $T_g$ (for high molecular weight PS $T_g$ = 100 ºC) is generally considered to be thermally activated, leading to Arrhenius laws for the stress rate at a given stress at $T << T_g$ [113, 114]. In the case of amorphous glassy polymers, plastic deformation is associated with the disentanglement of molecular chains with energy barriers. It involves, on the one hand, the intermolecular interactions at low strain rates and high temperatures [114] or, on the other hand, the activation of secondary $\beta$ molecular relaxation processes at high strain rates and low temperature [115].

It is possible to estimate the threshold load at which the PS yield strength $\sigma_y$ is reached in our case. On the one hand, the stress $\sigma$ is defined as:

$$\sigma = \frac{F_N}{\pi r^2}$$

Equation 16

where: $F_N$ = Load (N)

$r$ = contact radius (m)

In addition, the contact radius $r$ can be calculated by means of Hertz theory [116], assuming that no adhesion is present and that the tip is much harder than the sample:

$$r = \left(\frac{F_N R}{K}\right)^{1/3}$$

Equation 17

where: R = Tip radius ≈ 50 nm

$K = \frac{4}{3}\frac{E}{(1-\nu^2)}$, with $\nu$ as PS Poisson's ratio equals to 0.34 and $E$ as PS Young's modulus equals to 3.5 GPa [110].

Taking into account both equations and that the PS yield strength $\sigma_y$ has been determined at low strain rates and has a value of 88.9 MPa [117], the load at which plastic deformation begins is around 1 nN. This onset of plasticity is well below (about two orders of magnitude) the normal forces used in our experiments. Accordingly, there is always a

plastically deformed volume of polymer under the tip. As a consequence, this result is fully consistent with the ones in Chapter 3, where ripples are formed as a result of the competition between the plastic indentation and the elastic shear force exerted by the tip.

Furthermore, according to Richeton and coworkers [118], the $\sigma_y$ depends significantly on the strain rate and can be several times larger than the value measured at low strain rates. At that point, it is possible to determine the order of magnitude of the oscillatory strain rate provoked by the vibrations considering the following equation:

$$\xi = \frac{A_{vib}}{d}\,\omega$$

Equation 18

where: $\xi$ = strain rate

$A_{vib}$ = Vibration amplitude = 10 nm (Figure 26 (D))

d = PS film thickness = 400 nm

$\omega$ = angular contact resonance frequency = 2 $\pi$ $f_{res}$ =2 $\pi$ 360 kHz

The obtained strain rate is $\xi$ = 5600 Hz, similar to the ones used in reference [118] for other polymers. Therefore, a significant increase of the yield strength is expected from the oscillatory deformation. This increase at high strain rates, hence, contributes to the observed wear reduction under the external out-of-plane vibrations, in addition, to the stick-slip mechanism outlined above.

# 4.4. CONCLUSIONS AND NEXT STEPS

In Chapter 4, we investigate mechanisms of wear on compliant materials using an atomic force microscope. In particular, this Section is focused on the reduction of wear and friction on the nanoscale by means of normal ultrasonic vibrations.

The wear-induced nanoripples created on PS thin films by an AFM tip, as detailed in Chapter 3, are chosen as an appropriate system for this purpose. A highly-damped piezoelectric transducer, which vibrates vertically, is coupled to the bottom of the sample.

The effect of out-of-plane mechanical vibrations on rippling phenomena is investigated considering two parameters: the contact resonance frequency $f_{res}$ and the excitation amplitude $A_{exc}$ of the piezoelectric transducer coupled to the sample. The frequency and width of the resonance depend critically on properties of the sample, the load and the excitation amplitude. In addition, the $A_{exc}$ is accurately calibrated by a home-built Laser Doppler vibrometer.

We found that wear, as evidenced by the formation of ripples, is progressively reduced when out-of-plane vibrations are applied at a frequency close to the contact resonance between the cantilever and the sample, and when the amplitude, $A_{exc}$, of the external vibration increases. In addition, friction between the tip and the sample is also reduced under the same conditions.

Moreover, the effect of wear and friction reduction is reversible, indicating that the tip is not damaged by the ultrasonic vibrations, as shown in both contact and tapping® experiments.

Furthermore, the contact resonance merely amplifies the vibration amplitude ($A_{vib}$). In fact, vibrations of the same amplitude at other frequencies should be similarly effective. The $f_{res}$, however, enables control of friction and wear at very small transducer amplitudes (< 1nm for the studied cases).

Ultrasonic vibrations reduce wear and friction on the surface by facilitating the slip in each retracting phase of the vertical vibration. Besides, this effect might be aided by the so-called “strain hardening”, which is the hardening produced in the plastic regime of the deformation at high deformation rates.

Thus, our results suggest a possible method for “tuning” AFM nanopatterning, generated as mentioned in Chapter 3 by turning on and off the vibrations. They also confirm out-of-plane resonant contact vibrations as an efficient method to strongly reduce wear and friction on the nanoscale. Furthermore, the observed effect is particularly interesting in application to nano and microelectromechanical systems (NEMS and MEMS) operated in clean environments where fluid lubrication is not feasible. In this regard, the effect of in-plane vibrations should be also studied in the future.

Finally, as it was already mentioned in the previous Chapter, wear of compliant materials implies plasticity. As a consequence, a detail study of wear reduction by ultrasonic vibrations on the nanoscale should be also investigated in the future in terms of the plastic response and other properties of the specific material, but also of the temperature and the deformation rates. In fact, a research with those characteristics will be of enormous interest for mechanical engineering and practical applications, as it is expected to be relevant on the macroscale. In that case, it should be taken into account that the problem is much complex because the contact between macroscopic bodies is generally modelled as a multitude of micro or nanoasperities that are continuously established and ruptured. Therefore, the contact resonance will be spread over a wide frequency interval and change with time.

# Chapter 5

# INFLUENCE OF RIPPLED PATTERNS ON NEURAL STEM CELLS

# 5. INFLUENCE OF RIPPLED PATTERNS ON NEURAL STEM CELLS

In Chapter 5, we focus on the second type of nanoripples introduced in Chapter 1, the ones produced by ion beam sputtering over large areas instead of locally by AFM lithography such as in Chapters 3 and 4.

In this case, the multidisciplinary working environment at IMDEA Nanoscience allows us to combine nanotribology and biological field and increase the degree of research complexity in collaboration with Dr. Ángel Ayuso Sacido. Our first intention was to study the frictional behaviour of biological complex systems such as neural stem cells (NSCs) in order to extend previous work published in our group about nanosphere manipulation on glass rippled patterns [119]. However, this investigation became extremely challenging because of cell adhesion modification on those substrates. For that reason, we decided to center the study on investigating ripple influence on NSCs adhesion and orientation.

First of all, a brief review on the effect of patterns on manipulation of nanofeatures previously done in our group is included. Secondly, an introduction to contact guidance concept is done in order to relate nanopatterns and biosystems.

As a result, a comparison between the behaviour of mouse neural stem cells on flat and rippled glass substrates in terms of adhesion and filopodia orientation is performed by combining cell viability tests with optical microscopy and AFM. In addition, a theoretical model previously described in literature is applied to explain some of the experimental results.

## 5.1. BACKGROUND

### 5.1.1. INFLUENCE OF NANOPATTERNS ON MANIPULATION

Nanomanipulation became the subject of important investigations quite soon after the invention of AFM. In one of these first experiments on the topic, the AFM allowed to estimate the shear stress between $C_{60}$ islands and NaCl when the islands are pushed in contact mode [120]. However, contact AFM can be successfully used only on relatively “large” objects (hundreds of nm). On length scales of few tens of nm tapping mode is more reliable, although the friction forces between particles and substrate are not easy to quantify in this case. Gnecco and coworkers have demonstrated how the trajectories of nanospheres manipulated in tapping mode can be used as a signature of the friction force between spheres and substrate [80, 121]. In such a case, friction is expected to reduce the fluctuations and the apparent discontinuities in the trajectories. Furthermore, extensions to nanorods and irregularly shaped islands have been also proposed and tested experimentally [122, 123]. We introduced friction between Sb islands and substrate as fit parameter and estimated it from a comparison of a simple collisional model with the experiment. In addition, AFM-based manipulation experiments have been performed on complex biosystems such as biological

micro/nanoparticles [124], viruses [125] and cells [126, 127]. Nonetheless, these efforts have faced many limitations and restrictions.

All the aforementioned investigations were performed only on atomically flat surfaces. On the other hand, another investigation in our group show how anisotropic patterns can influence the manipulation of gold nanoparticles [119]. According to the results shown in Figure 35, nanosphere motion is confined to one channel in the ripple structure even if the sphere is pushed perpendicular to the ripple direction. When it reaches a bottleneck, it jumps into another channel and continues its longitudinal displacement. In an attempt to continue this previous work and linking this idea to the concept of contact guidance, we decided to study the influence of rippled patterns on manipulation and/or orientation of larger objects such as cells.

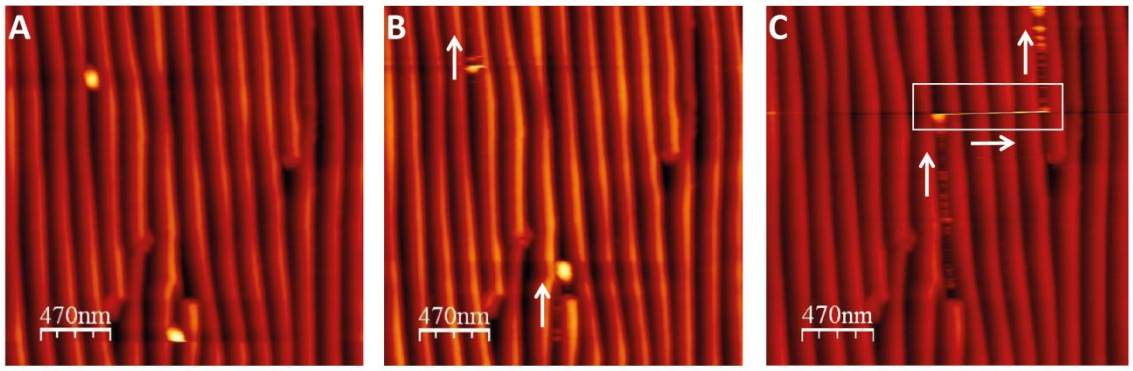


Figure 35. A series of consecutive topography images showing the manipulation of gold nanoparticles when the applied normal force is 3 nN. The arrows indicate the direction of motion of the particles. Reproduced from [119].

### 5.1.2. CELL RESPONSE TO NANOTOPOGRAPHIES

It is commonly recognized that surface roughness or topography is an important factor influencing cell adhesion, motility, proliferation and, in the case of stem cells, also differentiation. However, this response is different depending on the cell type [128]. Therefore, many nanostructures such as protrusions, porous and fibrous substrates have been designed in order to study the response of cells [129]. In particular, groove architecture has drawn much attention due to its ability to induce contact guidance, especially on the microscale.

Contact guidance consists in stimulating cell alignment on nano/micro grooved patterns and has special interest in tissues with anisotropic geometry i.e. skeletal muscle, cardiac muscle, tendon, ligaments and nerve [130]. Several possible mechanisms for contact guidance have been proposed such as selective distribution of proteins on the surface, formation of focal adhesions, aggravation and alignment of specific cytoskeleton and function of pseudopodia, in particular, filopodia. Additionally, multiple factors are associated to the occurrence of contact guidance e.g. the pattern scale, the mechanical and chemical properties of the material, the cell type and the experimental conditions [131]. Hence, it is widely accepted that the co-effect of one or multiple factors contribute to the mechanism of this process.

The expansion of nanotechnology, on the other hand, has brought the development of several novel nanofabrication methods for engineering cell-substrate interaction such as electron beam lithography, photolithography, dip-pen lithography, capillary lithography, polymer demixing, block-copolymer lithography, phase separation colloidal lithography, chemical vapor deposition of nanofibers, electrochemical etching or nanoimprinting [132]. For good discussions on this topic, see the reviews by Norman *et al.* and Wood [133, 134].

In particular, micro and nanogrooved or rippled surfaces have been frequently used in order to study contact guidance of different types of cells. The general response to such topographic rippled features is cellular alignment and elongation along the ripple direction. For instance, rat cardiomyocytes highly follow nanogrooves on polystyrene and polyurethane substrates [135]. C6 glioma cells and mammalian cells also grow parallel to nanoridges on polystyrene [136, 137]. Additionally, reference [138] shows that neurites can grow either parallel or perpendicular to micro/nanogrooves on quartz, depending on the depth and width of these structures. Moreover, Fujita and coworkers [139] described the behaviour of mesenchymal stem cells on polystyrene with 870 nm wide ridges/670 nm wide grooves and 200 nm in depth observing cell protrusions which extend either parallel or perpendicular to the nanopattern. In the same way, Teixeira *et al*. found that filopodia of human corneal epithelial cells align along or perpendicular to silicon nanogrooved patterns [140, 141] and similar results were reported in the case of macrophages [142]. In any case, it must be noticed that most of these studies have been performed on polymeric substrates where nanopatterning protocols change the polarity and, hence, the hydrophilicity of the raw materials.

In addition, any slight change in geometrical constraints such as width, depth, orientation or pattern can affect the behaviour of these biosystems. Therefore, investigation of the effects of structure and properties of nanomaterials has become a novel issue in multi-interdisciplinary fields, such as tissue engineering, regeneration medicine and material science.

## 5.2. MOUSE NEURAL STEM CELLS

A stem cell is an undifferentiated biological cell with the ability to differentiate into specialized cells when an exogenous stimulus is introduced in its environment and that can divide through mitosis to produce more stem cells [129]. There are two main types of stem cells: adult stem cells whose capacity to differentiate is limited and embryonic stem cells which are pluripotent.

Neural stem cells (NSCs) are adult stem cells that can differentiate into neurons, astrocytes and oligodendrocytes. Their establishment was one of the landmark events in neuroscience in the last 30 years. Furthermore, they play a key role in order to overcome the dogma related to the lack of regenerative power of nervous system and have been proposed for the development of new regenerative medicine approaches. For instance, *in vitro* artificial tissue growing for implantation into the injured site is one of the potential strategies for the regeneration of central neural system injuries [143, 144]. One of the simplest approaches in this regard needs substrates treated to maintain optimal conditions for adhesion, growth and

differentiation but also to allow directed migration that position the cells into specific location within the growing neural tissue [145].

In the present thesis, mouse C17.2 NSCs are chosen to study how their morphology and adhesion are influenced by anisotropic patterns, specifically, ripples. As mentioned in previous section, NSC contact guidance behaviour has a special interest due to their anisotropic geometry.

Mouse C17.2 NSCs line used in this research belongs to the personal collection of one of our collaborators in this work: Dr. Ángel Ayuso Sacido. This mouse multipotent cell line is capable of differentiation *in vitro* and usually has fibroblast-like morphology (Figure 36). The cell line was immortalized by using a lentivirus for a transduction of myc oncogene into mitotic progenitor cells of neonatal mouse cerebellum.

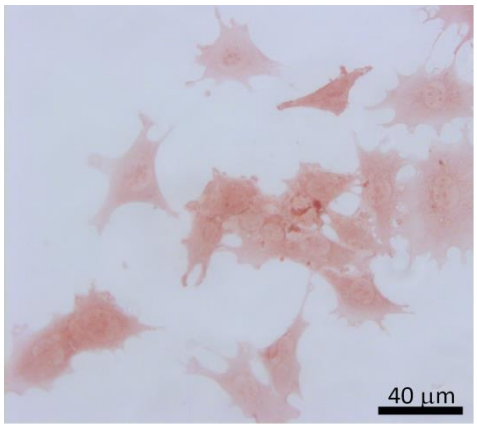


Figure 36. Optical image of mouse C17.2 NSCs.

During the experiments, mouse C17.2 NSCs are grown in media containing DMEM-F12 (Gibco) with 10 % fetal bovine serum, 5 % horse serum and 1 % pen/strep. In addition, cell lines are maintained at 37 ºC and 5 % $CO_2$.

# 5.3. GLASS RIPPLED SUBSTRATES

The substrates used in this study consist of arrays of parallel nanoripples made on glass. Figure 37 shows an AFM topography of the nanopatterned glass substrate where the ripples run on 1-2 µm. Their lateral periodicity is about 200 nm, their corrugation around 40 nm and their RMS roughness of about 12 nm.

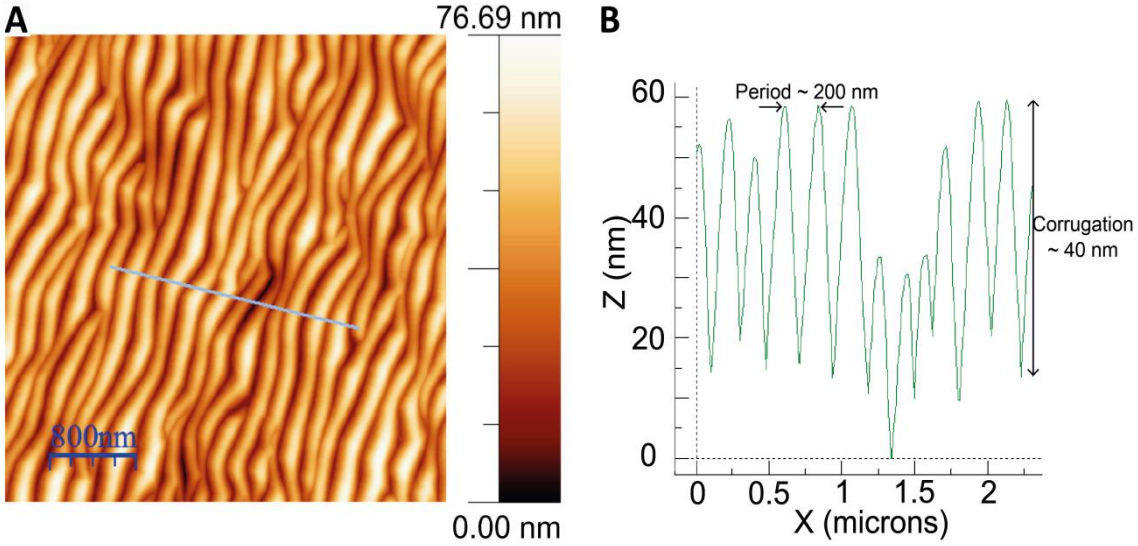


Figure 37. (A) AFM topography of a nanostructured glass surface used as a substrate for the stem cells. (B) Profile along the blue line in (A) showing the periodicity and corrugation of the ripples.

These ripples were produced by Prof. Francesco Buatier de Mongeot and coworkers at the University of Genoa (Italy) using defocused ion beam sputtering [146]. In Figure 38, a

scheme of this methodology is shown, where an ion source is used to physically remove atoms from the surface of the chosen target without any chemical reaction [147]. The mechanism of ion beam sputtering is considered a combination of erosion and surface diffusion. By this technique, during the bombardment with a low-energy defocused Ar ion beam, it is possible to form homogeneous, self-organized wavelike nanopatterns [148] in many different materials, either metallic [149, 150] or dielectric [146, 151], in a controlled way.

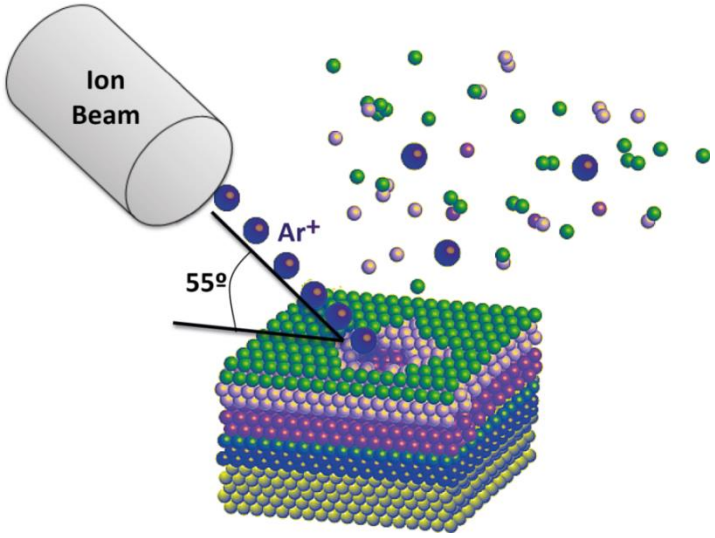


Figure 38. Scheme of ion beam sputtering technique.

In our case, flat glass cover slides (1 cm diameter, from Marienfeld-Superior, reference 0111520) are sputtered with a defocused Ar ion beam (5 N purity) in order to produce the previously mentioned nanoripples. Low-energy (800 eV) ion irradiation is performed in UHV generated from a gridded multiaperture ion source (TECTRA) at an incident angle of 35°, measured with respect to the surface normal. In order to prevent the charging of the sample, a biased tungsten filament that provides electrons by thermoionic emission is positioned at the end of the source ensuring an efficient neutralization of the surface during ion erosion.

Furthermore, defocused ion beam sputtering has several advantages. First of all, it belongs to the self-organized approaches, which can be used to obtain ensembles [152] or random networks [153] of nanostructures over large area substrates (~$cm^2$). In that way, it overcomes the limitation of top-down lithographic ones which allows to prepare highly defined geometry, shape and size nanopatterns [154, 155] but only in limited surface areas (~10-100 $\mu m^2$), opening an important issue in terms of technological application costs. Additionally, even though a slight change of stoichiometry of the irradiated top layer cannot be excluded due to the preferential sputtering Na atoms with respect to the predominant Si and O species forming the glass matrix [156, 157], in the present case, the steady state composition of the top is achieved after ion fluencies which are two orders of magnitude lower than those employed in typical experiments and no lateral modulation of the chemical composition is expected to occur. Hence, this strategy does not change surface polarity and can be considered as a natural alternative to classical chemical treatments focused on the constituents of the substrate such as gelatin, collagen, fibronectin, laminin or polyamino acids which reduce reproducibility between assays. Moreover, in contrast with the perfectly regular patterns that are usually adopted, these ripples have better matching with the complex irregular morphology of the cells. On the one hand, ripple dimensions are of the order of

magnitude of filopodia, which are considered the exploratory and guiding parts of the cells [158]. Moreover, the ripple irregularity is a bit closer to the natural environment of the stem cells as compared to very regular patterns. In addition to that, glass as a chosen material presents some benefits because it is inexpensive and completely transparent.

# 5.4. GLOBAL ADHESION MODIFICATION

As it has been previously mentioned in this Chapter, a strong correlation between substrate nanoroughness/nanotopography and adhesion modifications in cells has been reported by several groups. It has been recognized for instance the influence of membrane morphology on neuronal cells [159], of nanopores on mesenchymal stem cells [160, 161] and of nanotube diameters on the cell fate [162]. Still these effects have been rarely studied on nanopatterned glass surfaces.

## 5.4.1. VIABILITY TEST

First of all, a viability assay is performed using AlamarBlue® (Sigma R7017) in order to study the influence of the rippled glass substrates introduced in Section 5.3 on global adhesion of mouse neural stem cells C17.2.

This test can quantitatively determine cell viability because Alamar Blue® is an oxidation-reduction indicator of living cell metabolic activity and it is considered non-toxic for the cells. The compound is added to the cells in a concentration of 0.01 mg/ml and incubated at 37 ºC and 5 % $CO_2$ for 4 hours. During this time, resazurin (blue dye) is reduced by the living cells to resorufin (pink dye) as shown in Figure 39 (A). In that way, it is possible to measure the relative amount of living cells by measuring the absorbance at 570 and 600 nm (Figure 39 (B)) [163]. Cell viability (%) is obtained by using the following equation:

$$Cell\ viability\ (\%) = \frac{(A_{570} - A_{600})}{(A^*_{570} - A^*_{600})}\ 100$$

Equation 19

where: $A_{570}$ and $A_{600}$ are sample absorbances at 570 and 600 nm

$A^*_{570}$ and $A^*_{600}$ are positive control absorbances at 570 and 600 nm [164] (cells on flat substrates).

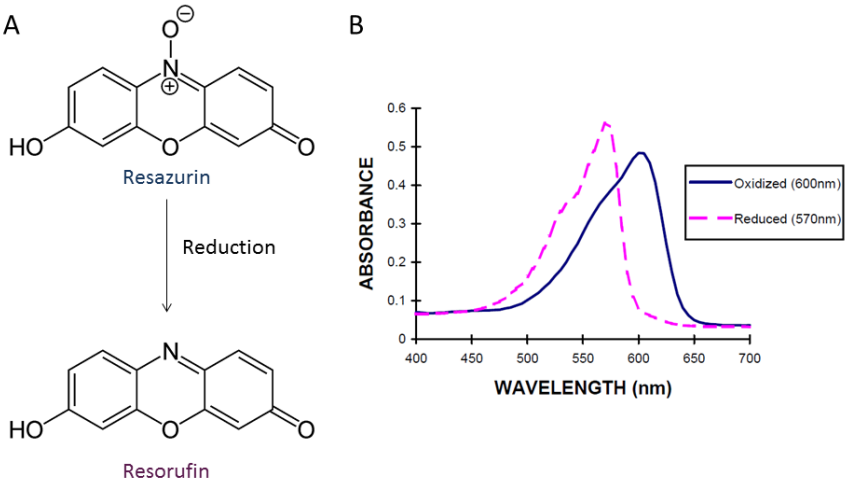


Figure 39. (A) Resazurin reduction into resofurin. (B) AlamarBlue® absorbance spectra from [164].

The response of around 5000 cells incubated for three days on both flat and rippled substrates is compared after 4 hours with AlamarBlue® and the results of a series of three independent experiments are shown in Figure 40. As it is observable in the graph, the percentage of cell viability on rippled substrates is much lower than on standard flat glasses. The mean value for the rippled case decreases to 41.3 % with a standard deviation of 6.3 % in comparison to the flat one. These results suggest that the global cell adhesion is strongly reduced on the nanostructured substrates due to the fact that neural stem cells are anchorage dependent (not viable suspended in a fluid) [128].

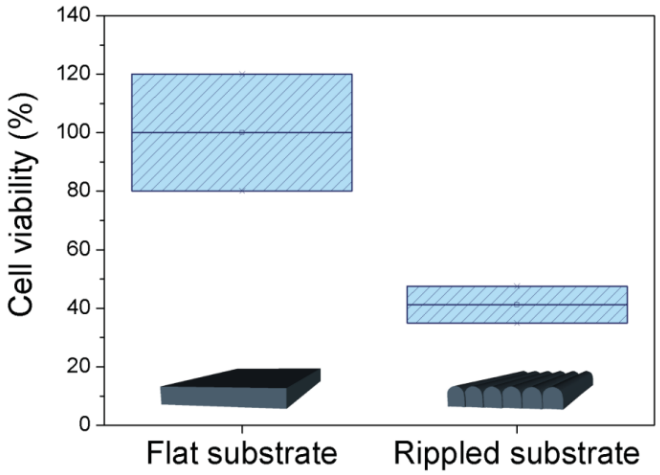


Figure 40. Relative cell viability (%) in a series of three independent experiments on stem cells adhered to flat and rippled substrates measured after three days of incubation at 37 ºC and 5 % $CO_2$ and 4 hours with AlamarBlue®.

## 5.4.2. MORPHOLOGICAL DIFFERENCES

As a complementary step to shed light on previous results, differences in the morphology of the cells either on a flat surface or on rippled glass are studied focusing on a single stem cell or small aggregates of them by using an optical microscope (Leica DMI 3000B).

The images are taken also in this case after three days of incubation in the normal conditions. Previous to the imaging, the cells are fixed in 4 % paraformaldehyde (PFA, Sigma-Aldrich) at room temperature for 20 minutes and cleaned several times with ultrapure water. After that, they are dyed with neutral red (Panreac) at room temperature for 2 minutes and cleaned with ultrapure water. Then, the cover slides are mounted on microscope slides using DePex (Serva).

Figure 41 shows how neural stem cells adhere to the flat and rippled substrates in a different manner. On flat surfaces the cells present the fibroblast-like morphology typical of NSCs and tend to form aggregates which extend laterally over hundreds μm. However, on rippled substrates, the cells have compact round shapes and their coalescence seems to be strongly inhibited. Thus, the cells are reluctant to spread on the rippled glass.

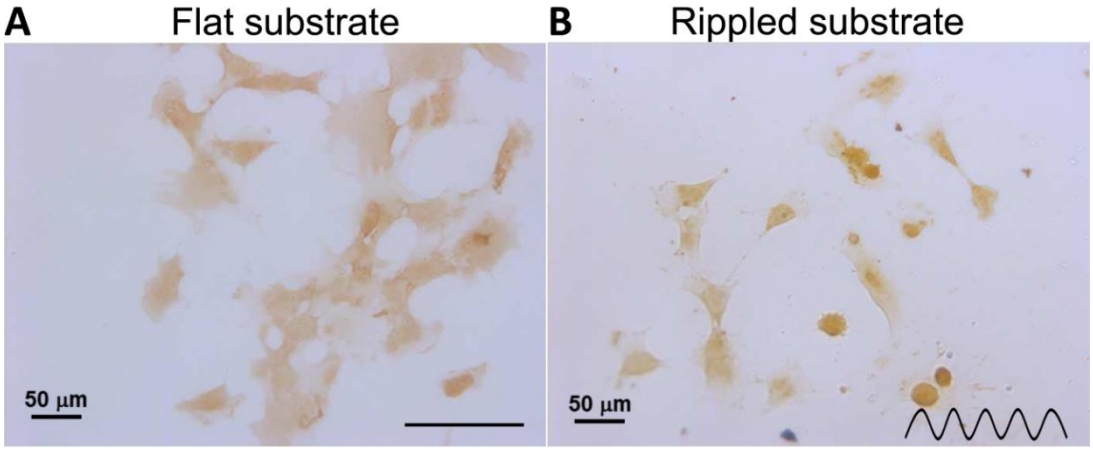


Figure 41. Optical images of NSCs adhered to (A) flat and (B) rippled glass substrates.

Additionally, we have tried to image living cells plated on rippled glass without being fixed by AFM in liquid in order to obtain more information about friction and adhesion phenomena. However, neither proper imaging of the living cells nor extracting useful information of adhesion and friction between cells and substrate has been possible. This kind of experiment faces many limitations. Since cells are not good adhered to the substrates, as soon as the AFM tip touches them, they move to another position or get attached to the tip (Figure 42) even though the minimum force required for performing the measurements is used (in contact and Tapping® modes).

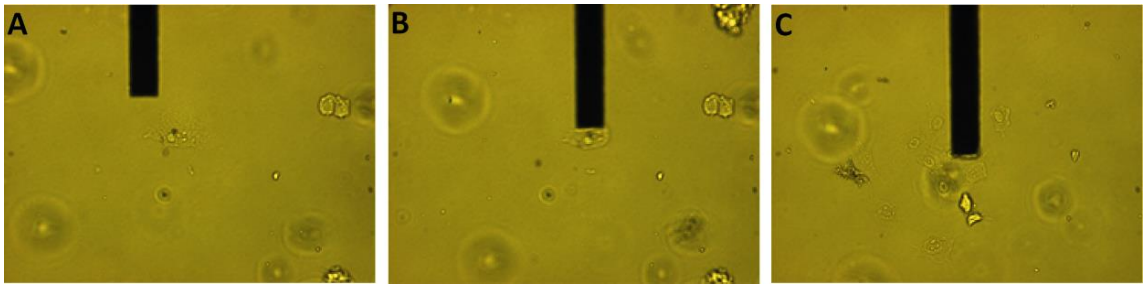


Figure 42. Optical image of (A) a cell before the tip touches it, (B) a cell that moves while the tip touches it, (C) a cell attached to the tip.

All these observations along with previous results fully confirm that the cell adhesion is significantly influenced by the surface nanotopography and roughness. In this context it is interesting to note that Bartolo *et al*. [159] also demonstrated that in random surfaces with nanoroughness between 50 and 200 nm, neurons presented round-shaped soma and poorly branched processes. Furthermore, Kulangara and coworkers [165] found that adhesion is downregulated in the case of human mesenchymal stem cells on nanogrooved substrates (350 nm in width and 350 nm in depth). The same behaviour is also observed when *E. coli* adhesion decreases on randomly rough (but isotropic) substrates [166]. This is related to the fact that, even if bacteria or NSCs have a linear size in the order of few tens of μm, the functional domains where they attach to the substrate are in the same range of the substrate roughness. In our case, the role of such functional domains seems to be played by the so-called filopodia.

# 5.5. LOCAL ADHESION MODIFICATION

Filopodia are thin cytoplasmic projections with a diameter around 60 - 200 nm [167] that steer fundamental cell functions such as cell adhesion, spreading and migration. As mentioned before, it is commonly recognized that topography plays a fundamental role in the formation of focal adhesion sites. In particular, reorganization of cell cytoskeleton and focal adhesion formation in response to nanostructures have special interest in research.

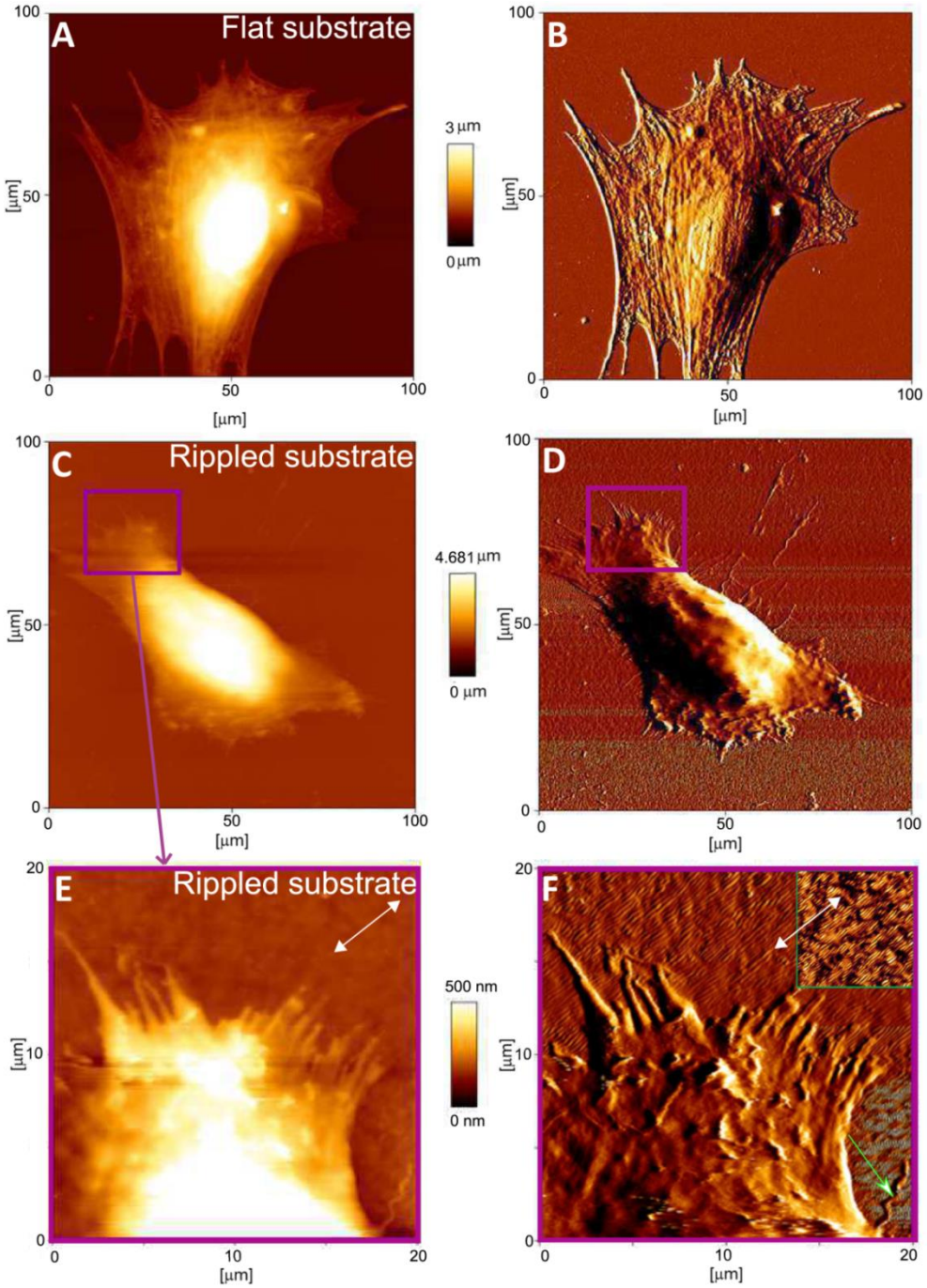


Figure 43. (A) Topography and (B) vertical deflection (indicating the local differences of sample heights) AFM images of NSC on a flat glass. (C) Topography and (D) vertical deflection AFM images of NSC on a rippled substrate. (E) and (F) AFM image zoom of (C) and (D). Inset in (F) shows the ripples with enhanced contrast. The white two-sided arrows indicate ripple preferential orientation. The white arrow shows zig-zag conformation assumed by a filopodium, which would be otherwise strongly misaligned with respect to the ripple pattern.

However, the mechanism by which filopodia can recognize topographical features is not fully understood although it is commonly accepted that it is related to steric hindrance in the case of nanogrooved patterns [158]. To gain insight into this attachment process, it is essential to study the arrangement of the filopodia with respect to the ripples. In order to deal with their characteristic length scales, we have conveniently imaged the dyed cells using an AFM.

Figure 43 (A) and (B) show a stem cell fixed on a flat surface imaged by AFM in Tapping® mode. Since the glass substrate is completely isotropic, the cell spreads along arbitrary directions and filopodia do not show any preferential direction. On the other hand, Figure 43 (C-F) shows a NSC on a rippled glass substrate imaged in two different magnification degrees. It seems from those images that in the latter case filopodia are strongly influenced by the anisotropic substrate morphology. In order to quantify this effect, the angles $\theta$ between the filopodia central axis and the ripple crest lines are measured for more than 50 data points in each case. The angle distributions on flat and rippled glasses are compared in Figure 44 (A) and (B). According to the histograms, the filopodia are found to align parallel and, to a lesser degree, perpendicular to the ripples. In fact, whereas the angle distribution on flat substrates is homogeneous, a peak around 0° and a minor one around 80° are observed on the rippled substrate, which indicates the two preferential direction alignment of the filopodia (Figure 44 (C) and (D)).

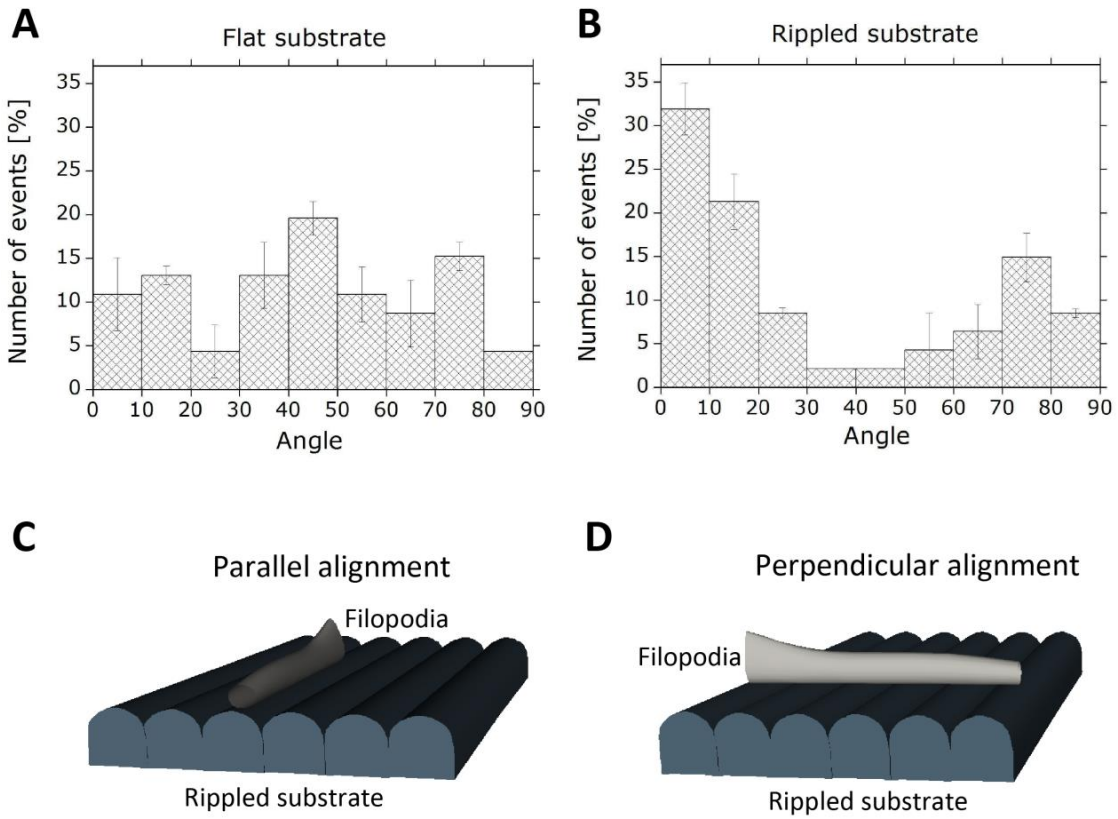


Figure 44. Statistical angle distribution of filopodia orientation when NSCs are plated (A) on a flat substrate and (B) on a nanorippled glass. Schemes of (C) parallel and (D) perpendicular alignments between filopodia and ripples.

This observation is not completely new. Even if parallel alignment of pseudopodia is generally prevealing, similar results have been reported when working with mesenchymal

stem cells and human corneal epithelial cells on micro/nanogrooved patterns by Fujita *et al*. [139] and Teixeira and coworkers [141], associating this behaviour to steric hindrance.

In our particular case, parallel alignment is easy to explain by the fact that since filopodia thickness *t* and the ripple height *h* are in the same range, the filopodia can conveniently conform to the ripple geometry (Figure 44 (C)). In this way, the contact area with the substrate is maximized and so that the local adhesion.

On the other hand, if the filopodia are tilted with respect to the ripples, and they are assumed to be rigid, the contact or focal adhesion points occur almost exclusively on the top of the "ridges" [131, 139]. Thus, the number of contact points between filopodia and substrate is maximum when $\theta$ = 90°, which also favors the perpendicular alignment by maximizing again local adhesion. However, in this case the situation is more complex due to the fact that filopodia are not rigid.

Still, it is important to notice that both parallel and perpendicular orientations correspond to the most symmetric possible configurations of the system and any deviation from them would result in the appearance of mechanical moments leading to the realignment of the filopodia along the preferable directions. This effect explains the zig-zag configuration of some filopodia, as the one highlighted by the green arrow in Figure 43 (F).

# 5.6. THEORETICAL MODEL

A theoretical model proposed by Carbone and Decuzzi [168] may help to clarify the complex situation observed in the AFM measurements. In this work it has been studied the possible configurations of a thin elastic beam on a rigid sinusoidal pattern (Figure 45), which is a simplified version of our biological system.

According to this model, the total energy ($U_{tot}$) of the elastic beam on the wavy pattern is the combination of three main contributions: the bending, the elongation and the adhesion of the beam, which sum up according to Equation 20:

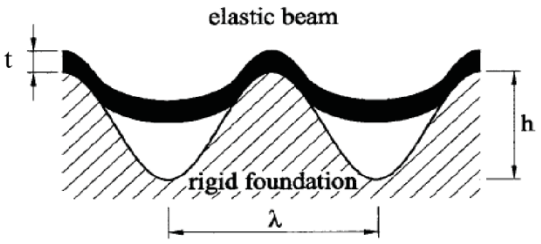


Figure 45. Scheme of the model system from [168].

$$U_{tot} = 2\pi^2(4\pi^2 a + \pi\sin(4\pi a) + \frac{4\,sin^2(2\pi a)}{1-2a}) \\ -12\,\frac{\gamma}{H^2T^2}\,\frac{I}{\pi} + \frac{48}{H^2T^2}\left(\frac{I}{2\pi} - a\right)^2 (\frac{I}{2\pi} + \frac{1}{2} - a)$$

Equation 20

Where: *I* = Elliptic integral = $2\pi\int_0^a \sqrt{1+(2\pi\sin 2\pi x)^2}\;dx$

*T* = Dimensionless thickness = beam thickness (*t*) divided by the period (λ)

*H* = Dimensionless height = Height of the wavy pattern (*h*) divided by the period (λ)

γ = Dimensionless surface energy density = Surface energy density ($\tilde{\gamma}$) divided by the elastic modulus (*E*) times the beam thickness (*t*) = $\tilde{\gamma}/Et$. The surface energy is described as the

total work per surface unit required to detach the beam away from the full contact condition to a final zero contact area.

*a* = Dimensionless contact length = Contact length ($\tilde{a}$) divided by the period ($\lambda$). The quantity *a* is not known *a priori* and must be determined numerically by the condition that $U_{tot}$ has a minimum. As a result *a* is found to depend on the elastic and geometric properties of the system and the surface energy density.

For applying this model to the particular studied system, some parameters have been assumed taking into account the characteristics of both filopodia and ripples: *t* = 100 nm, *h* = 40 nm, $\lambda$ = 200 nm and an elastic modulus for the filopodia *E* = 50 kPa [169]. In that way, *a* can be determined numerically for different values of the surface energy ($\gamma$) as shown in Figure 46 (A) and (B). As a result, we observed that *a* undergoes a rather abrupt transition from 0 (no adhesion, Figure 46 (C)) to 0.5 (full adhesion, Figure 46 (D)). This value corresponds to a surface energy density of around 1.5 mN/m, which is well below typical values for biological materials (in the order of 10 mN/m [170]). This means that, according to the model, the filopodia perpendicularly aligned are expected to fully adhere to the ripples.

It is important to notice that whether this is also the case when the beam is tilted by an angle $\theta \neq 90°$ can only be substantiated by extending the model to three dimensions. Even in that case, it remains questionable whether a filopodium can be simply approximated by an elastic thin beam.

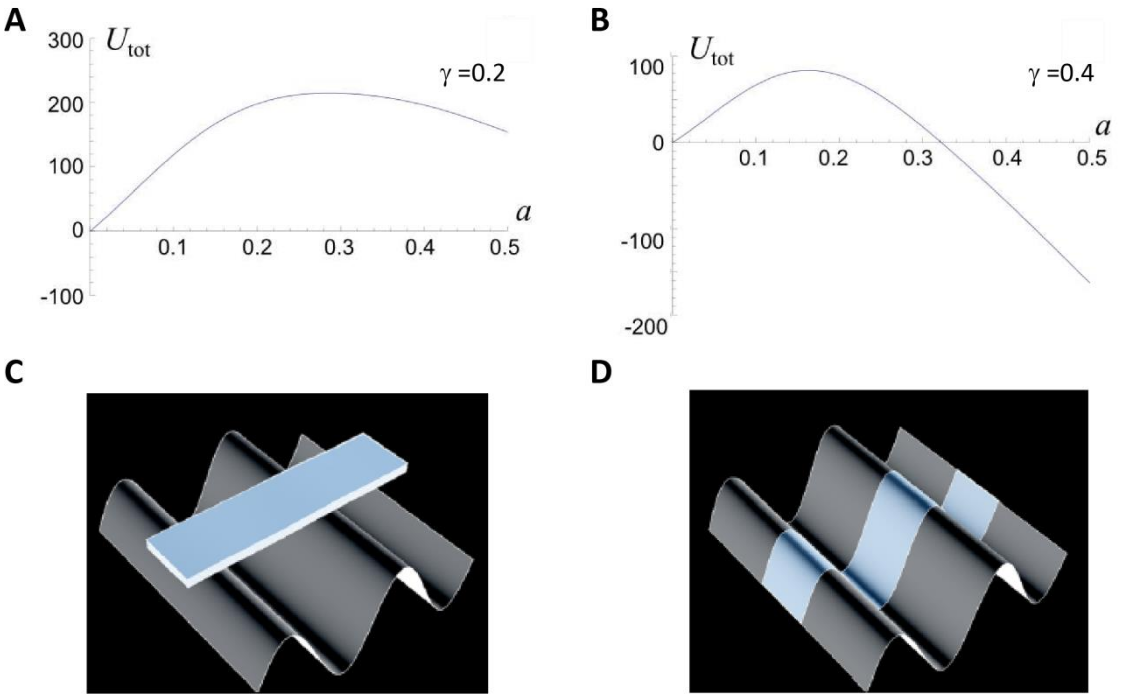


Figure 46. Total energy of an elastic beam adhering on a rigid wavy substrate as function of the half of the contact length *a* for two different normalized surface energy (A) $\gamma$ = 0.2 and (B) $\gamma$ = 0.4. The minimum value is obtained for *a* = 0 and *a* = 0.5 respectively. Scheme of an elastic beam on the rigid sinusoidal substrate when (C) no adhesion and (D) full adhesion are considered (reproduced from [171]).

# 5.7. OTHER NANOSTRUCTURES AND FUTURE WORK

Mouse NSCs C17.2 have been also used to carry out a couple of preliminary assays on other two glass nanostructures produced by defocused ion beam sputtering.

The two nanopatterns present very different geometrical characteristics as observed in Figure 47. On the one hand, nanostructure I consists of low corrugation ripples with a periodicity around 200 nm and height of about 11 nm (Figure 47 (A and B)). In the case of nanostructure II, a different kind of feature is chosen: large holes with a periodicity around 1.36 μm and a corrugation of about 200 nm.

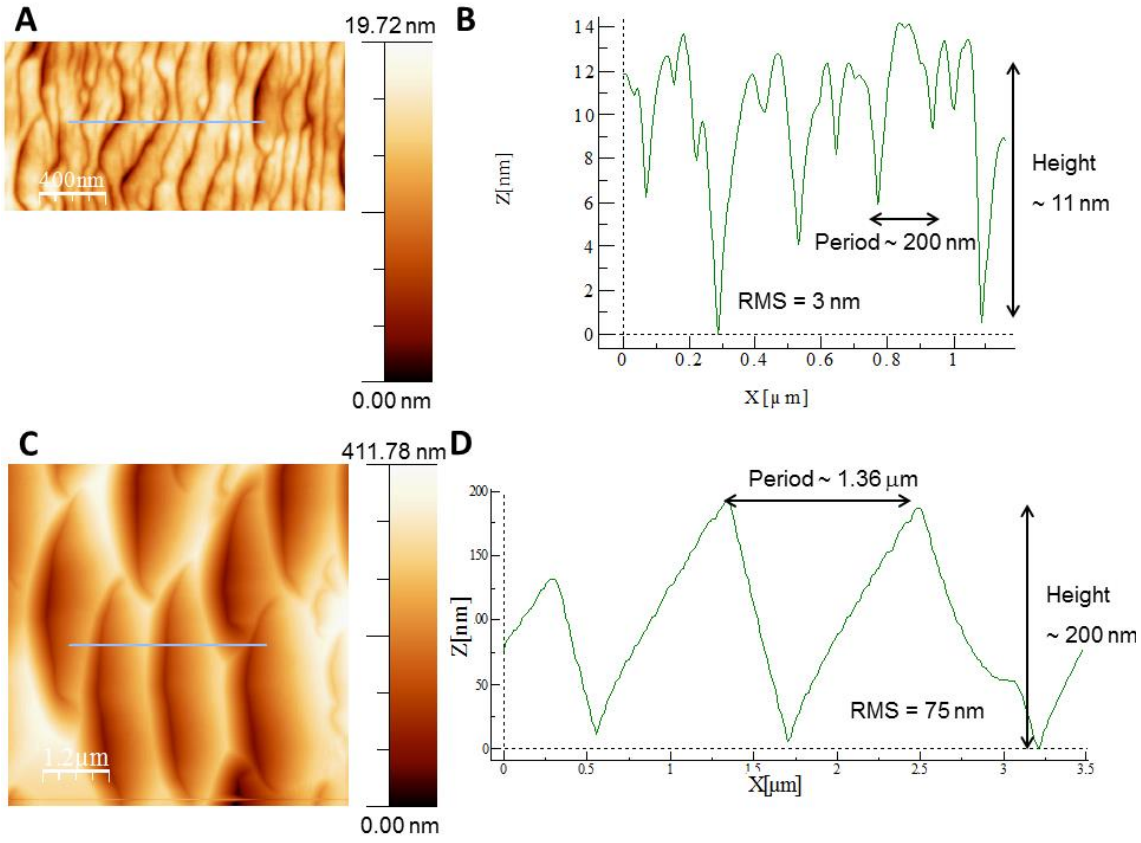


Figure 47. AFM topography of (A) low corrugation rippled and (C) nanoholed glass surface. (B) (C) Profiles along the blue line in (A) and (B) respectively, showing the periodicity and height of the patterns and room mean square (RMS) surface roughness.

The behaviour of NSCs plated on those glass substrates differs significantly in terms of global adhesion. Nanostructure I (low RMS) does not seem to affect global cell adhesion or viability when comparing to the control flat substrates. However, in the case of nanostructure II (high RMS) relative cell viability decreases to 57 %, morphology becomes rounder in some cases and cells do not aggregate, so that the global adhesion is reduced.

Figure 48 shows NSCs fixed on nanostructure I (A-C) and II (D-E) after three days of incubation at 37 ºC and 5 % $CO_2$. If comparing these results to control ones (flat glass substrates), there are no significant differences between them in none of the cases in terms of filopodia orientation. Moreover, cell podios does not seem to be aligned with the low corrugation ripples or the nanoholes, but randomly distributed. In the case of nanostructure I

the most probable reason it that, since the ripples present extremely low RMS roughness (around 3 nm), the cells do not feel differences between them and flat substrates. In addition, visualizing these ripples with the AFM after plating the cells on them is complicated because they seem to be covered by the medium and this could also mask the topographic effect. On the other hand, the presence of holes make difficult for the filopodia to adhere and if they do, they do not follow the preferential orientations of the substrate. Thus, nanoholes might not be the most suitable feature for inducing filopodia reorientation because their degree of anisotropy is lower than in the case of ripples.

Combined with the results in Section 5.5, these observations show how interesting would be developing a systematic and statistical set of new experiments in order to investigate in detail, among others, the threshold values of corrugation and roughness required to induce local and global adhesion modification, filopodia reorientation and the most suitable geometrical features for specific applications.

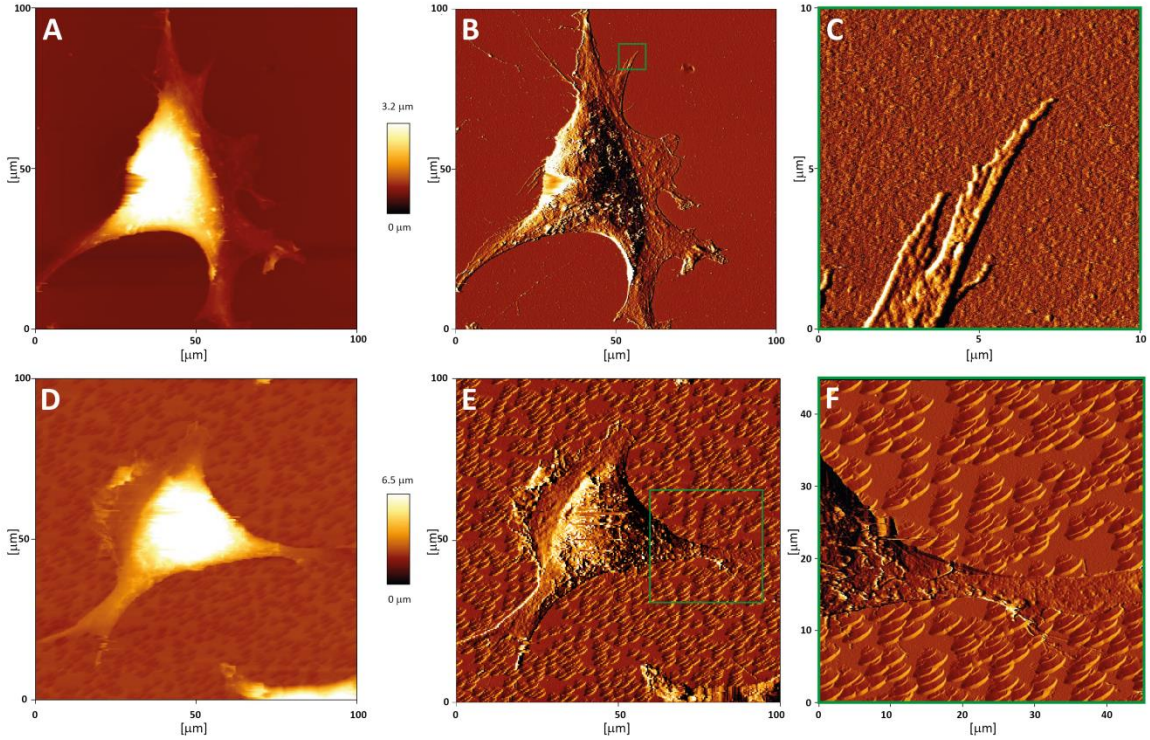


Figure 48. (A) Topography and (B) vertical deflection (indicating the local differences of sample heights) AFM images of a NSC on low corrugation rippled substrate (nanostructure I). (D) Topography and (E) vertical deflection AFM images of a NSC on nanoholed glass substrate (nanostructure II). (C) and (F) AFM image zooms of (B) and (E), respectively. Green squares indicate the zoom area.

# 5.8. CONCLUSIONS AND NEXT STEPS

In this Chapter, the effect of a rigid rippled surface pattern on the adhesion of neural stem cells is studied on glass, which is a biocompatible, cheap and completely transparent material. In particular, the spontaneous arrangement of mouse NSCs (C17.2) on irregularly undulated glass substrates is investigated by means of cell viability tests, optical microscopy and AFM measurements.

The rippled patterns are produced by defocused ion beam sputtering on glass. Compared to other top-down lithographic methods, this technique allows patterning homogeneously large areas (up to 1 $cm^2$) of different materials in a single step, without changes in surface polarity or wettability that could affect the behaviour of the cells.

This type of morphology is chosen, firstly, because a grooved architecture is particularly interesting for tissues with anisotropic morphology such as NSCs. In addition, ripple periodicity and corrugation can be tuned to be comparable to the cell filopodia thickness (in the 100 nm range).

As a result of these similarities, ripples induce a pinning effect on the filopodia, which are found to preferentially align parallel and perpendicular to the nanogrooves. Therefore, local adhesion increases due to this geometrical "trapping" mechanism.

On the other hand, as a consequence of the local pinning, the stem cells are prevented to spread out and their shape remains round and compact, influencing in this way the global structure and morphology of NSCs. Considering that, the contact total area between NSCs and substrate is reduced when comparing them to cells plated on flat surfaces. The resulting global adhesion between mouse NSCs and glass decreases as well as their viability.

A 3D theoretical model is needed in order to fully understand all the phenomena studied experimentally. A good starting point can be the 2D model developed by Carbone *et al.* [168] for the adhesion of a thin elastic beam on a wavy substrate.

Our results support the use of nanorippled glass substrates as a scaffold to induce adhesion and morphological changes in biological materials in a self-organized way, without forcing their response by external fields. This strategy yields as a rather inexpensive, easily reproducible and natural alternative to typical chemical treatments. Furthermore, since this surface nanotexture allows also the possibility of controlling both adhesion and orientation (factors that have a strongly impact on directing stem-cell differentiation), they could find important long-term applications in regenerative medicine.

Finally, more experiments will be required in order to systematically investigate the corrugation/roughness threshold values for inducing structural and adhesion modifications in NSCs and the most convenient geometrical architectures for each specific application. In fact, one of the basic challenges in biotribology is to identify the mechanisms of cell adhesion, motion and differentiation. This interdisciplinary task will involve the fields of the biology, mathematical modeling and physical science with suitable applications to medical and biotechnological science.

# Chapter 6

# NANOTRIBOLOGY OF GRAPHENE

# 6. NANOTRIBOLOGY OF GRAPHENE

In Chapter 6, nanotribological aspects of graphene are investigated in two different samples and environments. Since graphene has a natural wavy structure [172, 173], we firstly wanted to exploit this intrinsic characteristic together with its negative thermal expansion coefficient to create large ripples on free-standing graphene membranes by using a thermal treatment and study their influence in lubricant properties. A general characterization of suspended graphene membranes before and after inducing ripple formation was thus done by FFM, QNM and UFM. Unfortunately, the obtained ripples were not enough homogenous to investigate in detail the tribological behaviour of the samples in air.

Since much higher resolution has been reported in our group using FFM in water (on mineral surfaces [174, 175]), we have thus considered this environment also for the characterization of graphene. This was not feasible on the previous membranes, whereas atomic resolution is repeatedly obtained on graphene previously grown on copper. Additionally, our results are compared to molecular dynamics (MD) simulations, performed in the group of Prof. Rubén Pérez (Universidad Autónoma de Madrid), showing that FFM images of graphene in water are indeed expected to be very similar to those acquired in ultra-high vacuum with the same technique.

## 6.1. BACKGROUND

Graphene is one-atom-thick planar sheet of carbon atoms, bound by covalent $sp^2$-bonds, disposed in a densely packed honeycomb crystal lattice as shown in Figure 49. Besides, it is the building block of graphite, in which graphene layers are stacked and held together by van der Waals forces.

Since its discovery in 2004, graphene has grabbed appreciable attention in many research and technological areas due to its exceptional properties such as high electrical and thermal conductivities, superior mechanical strength and elastic properties and high optical transparency [176-180]. Those special properties have opened up promising perspectives of future applications and the creation of new devices and systems, especially in nanotechnology [181-183].

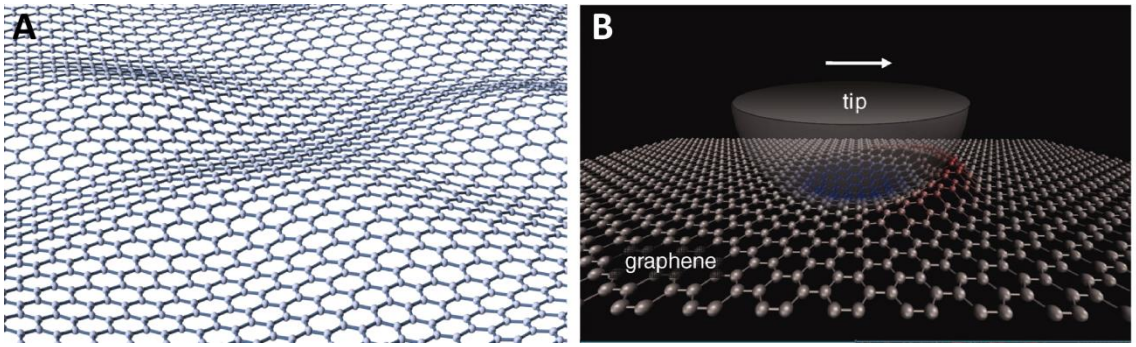


Figure 49. (A) Scheme of a graphene sheet [184]. (B) A schematic of an AFM tip sliding on a graphene layer showing the “puckering” effect [185].

In particular, among its many applications, graphene has been also proposed as a solid lubricant because of its high chemical inertness, extreme strength, easy shear capability, atomically smooth surface, low surface energy and low friction coefficient [186-188]. In principle, graphene coatings could be applied to reduce friction on surfaces such as those of micro/nanoelectromechanical devices (MEMS and NEMS) where oscillating, rotating and sliding contacts seriously reduce lifetime.

It is surprising that despite intense R&D efforts on graphene for plenty of existing and future applications, its tribological potential remains relatively unexplored in comparison. Some theoretical and experimental studies have investigated the nature of graphene friction mechanisms based on computational methods at different scales and atomic force microscopy. First of all, it has been demonstrated that the friction force decreases as the number of layers increases [189-191]. This force is considered to be dominated by the contribution from the out-of-plane deformation, the so-called "puckering" effect (Figure 49 (B)) and the quality of contact variation when a tip slides over the graphene surface [192]. In general terms, the AFM tip deforms ultrathin layers in the course of sliding leading to a higher contact area and, therefore, to higher friction. On the other hand, the effects of the chosen substrate on the final friction coefficient have been also examined. According to Lee *et al.* [191], the bond between the graphene and the substrate plays a key role in the lubrication. Both free-standing graphene and graphene attached to surfaces with little interaction with the substrate (i.e. $SiO_2$) act in a similar way in terms of the number of layers. On the other hand, if atomically flat and strongly adherent substrates (for example mica) are used, the friction behaviour described above is no longer true. Kim and coworkers [188] have also observed that the preparation method influences the final tribological properties of the graphene flakes. The variation in the properties of graphene grown on different materials is attributed to the different adhesion between graphene flakes and substrate. This fact also leads to contrasting effects in wear resistance. As an example, Marchetto *et al.* [193] observed a considereably running-in effect when the graphene layer is torn away locally after several loading and unloading cycles.

As mentioned before, two completely different approaches are followed in this thesis in order to extend the study of graphene nanotribology in air and water media on suspended membranes and Cu-supported graphene, respectively.

At this point, it is important to notice that the previous observations have been reported for planar configuration or suspended membranes. However, diversity in the local roughness could affect the frictional behaviour of the material. For that reason, in the first part of the Chapter, free-standing graphene membranes are characterized in air before and after they undergo a thermal treatment to create large ripples in the flake by using graphene negative thermal expansion coefficient. Nevertheless, the obtained wavy patterns do not show homogeneous periodicity and corrugation and, so that, they are not enough suitable for comparison. As a consequence, we did not continue in this direction, but rather moved to the characterization of graphene in water. Here, we succeeded in obtaining atomic resolution of graphene on copper by friction force microscopy as shown in Section 6.4.

# 6.2. SAMPLE PREPARATION

## 6.2.1. SUSPENDED GRAPHENE MEMBRANES

Suspended graphene membranes on $Si_3N_4$ were produced following a method developed by Dr. Stephano Rodaro and coworkers at NEST Laboratory (Pisa, Italy). This procedure consists of several steps. First of all, a silicon nitride substrate is patterned using photolithography with a conventional photoresist and reactive ion etching (RIE) [194] to obtain holes of different diameters (3-10 μm) as shown in the scheme in Figure 50 (A).

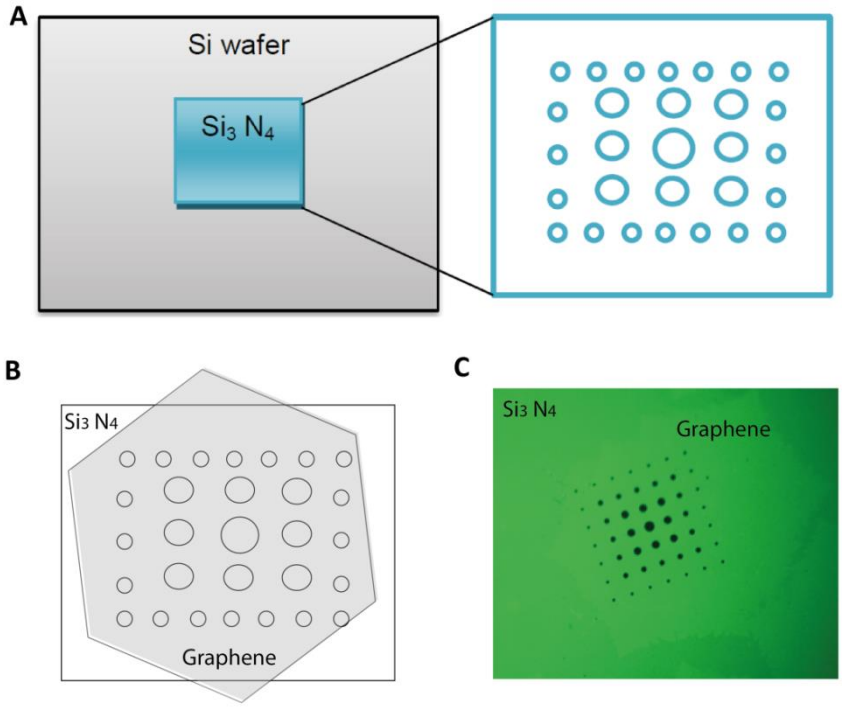


Figure 50. Scheme of (A) the $Si_3N_4$ membrane with the array of holes and (B) the graphene flake on the top of the arrays of holes. (C) Optical image of the real membrane sample.

In parallel, large graphene monocrystals (typical size 100-200 μm) are grown on copper via CVD growth at a pressure of 25 mbar and a temperature of 1060 ºC inside a 4 inch cold-wall reactor (Aixtron BM Pro) [195]. After that, poly(methyl methacrylate) (PMMA) is spin-coated on the surface. The graphene is detached from the Cu growth substrate using electrochemical delamination ("Bubbling transfer") method by immersing it in a NaOH solution where hydrolysis is carried out. In that way, the produced bubbles induce the separation of graphene from the Cu layer. Employing a semirigid polyimide frame, free-standing graphene/PMMA membranes are rinsed in deionized water and dried. Then, the large graphene/PMMA flakes are placed onto the $Si_3N_4$ membrane by a semi-dry transfer using a microscope equipped with a micromanipulator [196]. As the PMMA is completely transparent, graphene flakes can be easily observed and correctly positioned as shown in the scheme of Figure 50 (B). The sample is then heated up to 120 ºC for 5 minutes. The PMMA is finally removed by means of dissolution in acetone for 30 min and in isopropanol for 1 min and dried by nitrogen flow. The resulting sample is shown in Figure 50 (C).

The formation of ripples in some of the free-standing graphene samples is induced by a thermal treatment considering the negative thermal expansion coefficient of graphene [197,

198]. The procedure starts with a fast heating up to 400 ºC in vacuum (~$10^{-3}$ bar) for 5 min in an annealing chamber. After that, the cooling down is done firstly introducing a very small nitrogen flow and then fast in air. In order to avoid any oxygen in the chamber, prior to the heating process, at least 5 cycles/purges are done with nitrogen.

### 6.2.2. GRAPHENE ON COPPER

The graphene on Cu samples were prepared by Dr. Yu Zhou and Dr. Li Lin from the Beijing National Laboratory for Molecular Sciences and the College of Chemistry and Molecular Engineering at Beijing University. The used methodology is described below. A 5 x 5 $cm^2$ copper foil (99.8 % purity, 25 μm thick, Alfa Aesar) is polished using the electrochemical method, washed for 10 min by ultrapure water (18 MΩ cm) and dried with a high-purity nitrogen flow for 5 min. After that, the pretreated Cu foil is cut into 2 x 2 $cm^2$ and loaded into a home-made low pressure chemical vapor deposition (CVD) system in a multizone furnace (Lindberg Blue M HTF55667C) and the chamber is evacuated to 0.1 Pa. The Cu foil is then annealed at 1020 ºC by introducing hydrogen (5 standard $cm^3$/min, partial pressure of ~10 Pa) to remove the oxide from the surface. Subsequently, methane (10 $cm^3$) is introduced into the chamber for 30 min to grow the intrinsic graphene film. The fast cooling down to 700 ºC is done by quenching the quartz tube. The growth is finished with hydrogen and cooling to room temperature in 10 min.

## 6.3. SUSPENDED GRAPHENE MEMBRANES

Suspended graphene membranes [172, 199] are a useful experimental testbed in a wide range of areas. Among other advantages, the sample geometry can be precisely determined, the 2D structure is less sensitive to the presence of a single defect [179] and the graphene behaviour is not directly influenced by the substrate underneath.

On the other hand, structural defects such as atomic ones, wrinkles or ripples and microscopic corrugations have already been reported on supported graphene and considered to be the cause of changes in graphene properties or performance.

In this part of the Chapter, preliminary results on suspended membranes are presented. They are generally characterized here topographically and tribologically in the sub-μm scale. Furthermore, large ripples are obtained in those samples after a thermal treatment at 400 ºC. This part of the thesis was conducted during a 3-week scientific stay at NEST Laboratory and CNR-INO (Pisa, Italy) under the supervision of Dr. Pasqualantonio Pingue and Dr. Franco Dinelli in the framework of a Short Term Scientific Mission (STSM) grant included in the COST Action MP1303.

### 6.3.1. CHARACTERIZATION BEFORE THERMAL TREATMENT

First of all, we performed a general characterization of large areas in the samples prepared as explained in Section 6.2.1. One of those areas is shown in Figure 51, where three different PeakForce® channels, see Section 2.2.3, (topography, error and deformation) of the

suspended graphene membranes on different diameter holes are observed. In agreement with optical images, graphene flake covers all the holes on the $Si_3N_4$ substrate.

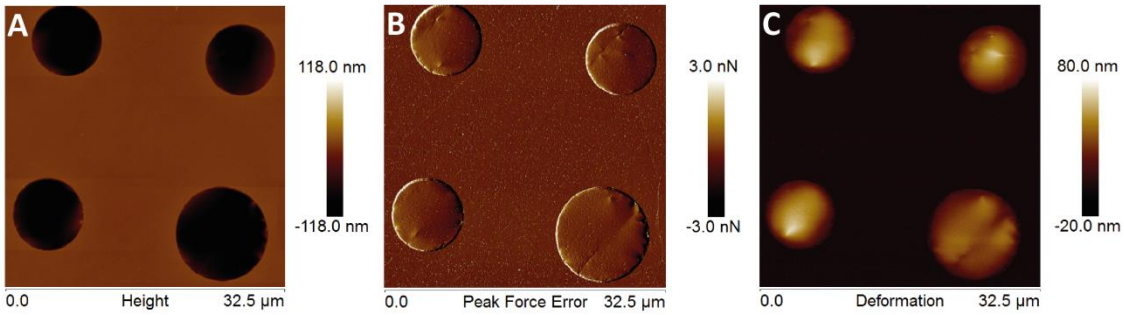


Figure 51. PeakForce images of a large area with 4 suspended graphene membranes on different diameter holes. Three PeakForce channels are shown: (A) Topography, (B) PeakForce error, (C) Deformation.

In particular, PeakForce™ nanomechanical maps of a suspended graphene membrane on a 8-µm-diameter holes are presented in Figure 52, before thermal treatment. In all signals images, it is possible to discriminate between the free-standing graphene and the $Si_3N_4$ substrate. Besides, PeakForce™ allows us to easily identify, especially in the topography and the error signals, the defects in the membranes and the more pronounced pinning points in the borders of the holes in accordance with previous reports [194]. In all the cases, the membrane depth, as well as the deformation, increases when increasing the applied normal load, as expected. Furthermore, the adhesion and dissipation are higher on the suspended graphene membrane and are highly affected, together with the deformation, by the previously mentioned defects on the membrane itself.

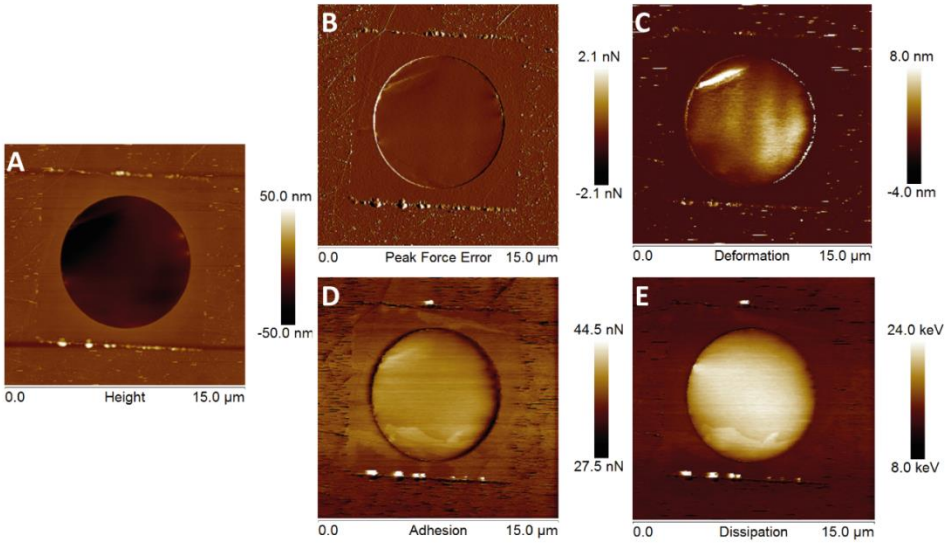


Figure 52. Graphene suspended membrane on a 8-µm-diameter hole before any thermal treatment, measured using PeakForce QNM™: (A) Topography, (B) Peak Force Error, (C) Deformation, (D) Adhesion and (E) Dissipation. The applied load is 1 nN.

Moreover, it is important to note that some features that appear in both adhesion and dissipation components of the PeakForce QNM™ can be also detected in UFM images (Section 2.2.4.2), as the ones shown in Figure 53. These features could correspond to contaminants or elements related to defects on the surface and further studies such as RAMAN, infrared microscopy or EDX should be done in the future in order to understand their nature.

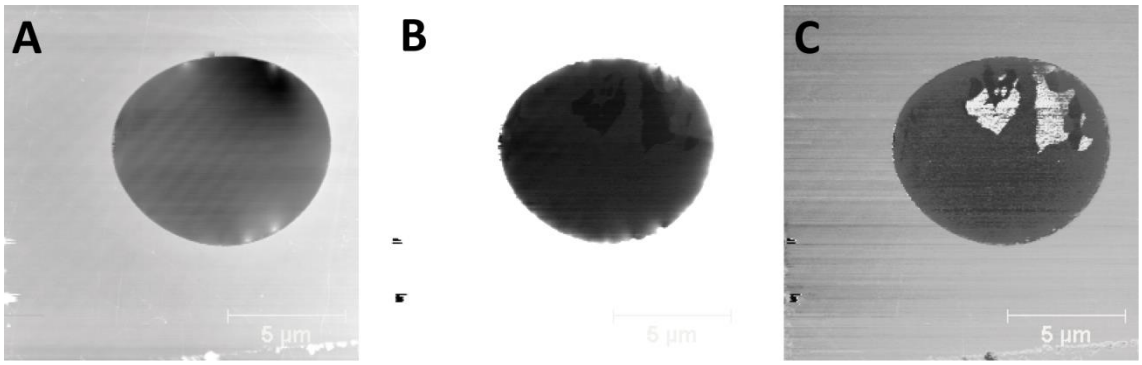


Figure 53. UFM images of suspended graphene membrane on a 8 μm diameter hole before any thermal treatment. (A) Topography. (B) UFM ρ and (C) UFM θ signals. The ultrasonic frequency is 2.28 MHz and the amplitude 5 V.

After the general characterization presented above, friction measurements on the sample have been performed. Each experiment consists of recording the lateral force while increasing and decreasing the normal force.

Figure 54 shows the lateral force vs the load on a suspended graphene membrane on the top of a 8 μm hole before the sample undergoes any thermal treatment. A linear behaviour with no hysteresis is observed. Furthermore, the friction coefficient obtained from the line slope is $\mu_{Gbefore}$ = 0.084 ± 0.030, in the same order of magnitude of previous ones reported in literature [190, 191].

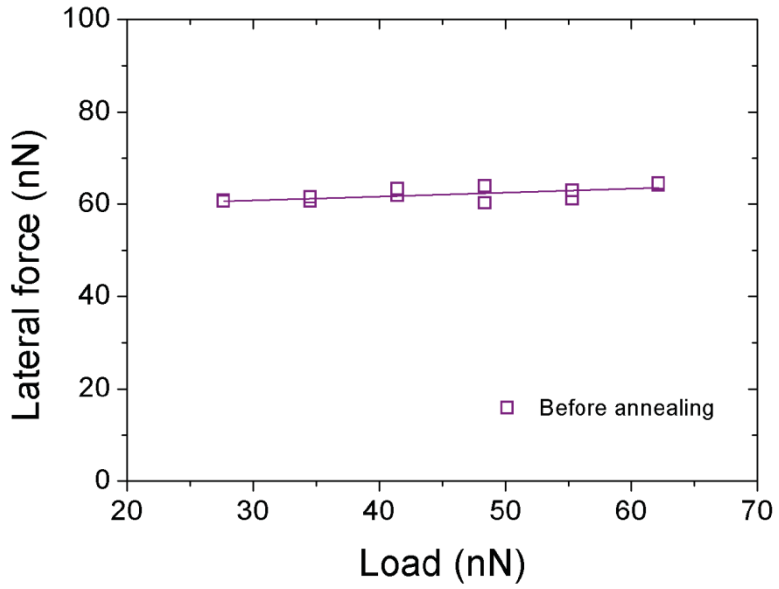


Figure 54. Lateral force vs applied normal load for a free standing graphene membrane on a 8-μm-diameter hole before thermal treatment.

### 6.3.2. CHARACTERIZATION AFTER THERMAL TREATMENT

Once the free-standing membranes are characterized, ripples are induced on their surface by exploiting their thermal expansion coefficient. A thermal annealing is performed on the sample and it is upon the cooling down when large ripples appear and/or buckling occurs, depending on the geometrical boundary conditions [197, 198]. The ripples arise from the

compressive strain induced by the graphene negative thermal expansion coefficient in comparison with the silicon nitride one. The effect of the thermal treatment is observed in Figure 55, where two 3D topographies, one before and one after the annealing, are shown for a membrane suspended on a 8-μm-diameter hole.

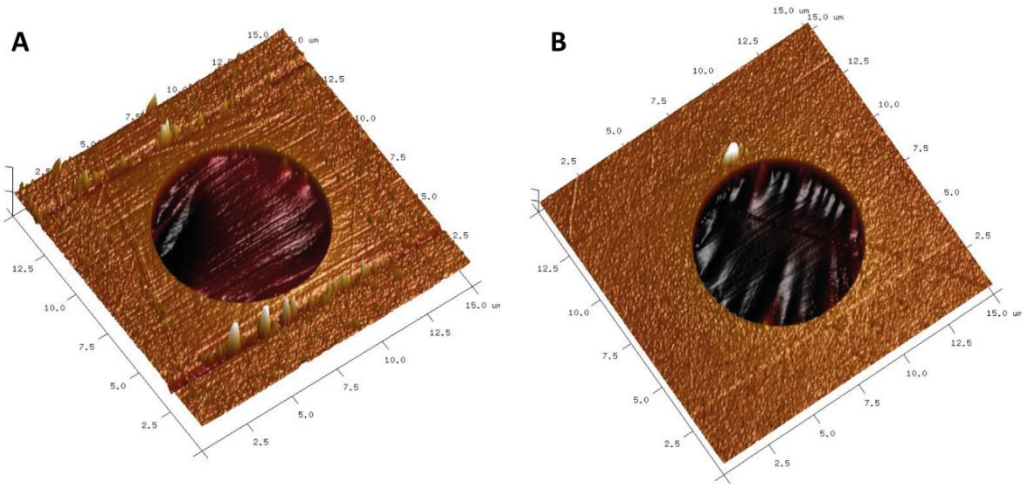


Figure 55. 3D topography of a free standing graphene membrane (A) before and (B) after thermal annealing.

Very interesting information about the strain can be obtained by microRaman spectroscopy maps [200, 201], as the ones in Figure 56. According to the results, the strain is quite homogeneous when the graphene membrane is on $Si_3N_4$. However, in the free standing membrane there are many inhomogeneities as shown in the 2D position Raman map. This result is consistent with the presence of ripples in this part.

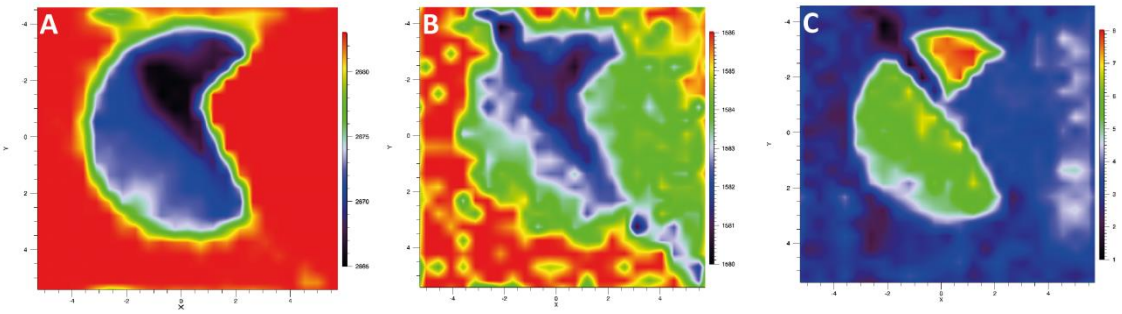


Figure 56. Raman spectroscopy of a suspended graphene membrane on a 8 μm hole after annealing (same membrane of Figure 55 (B) and Figure 57. (A) 2D position mapping, (B) G position mapping and (C) 2D Intensity/G Intensity mapping.

Moreover, the ripple-like structure is clearly visible in other PeakForce™ signals acquired with the topography, such as error, dissipation and especially deformation, which presents the highest contrast (Figure 57). These ripples are not as regular as the ones previously reported in the literature [197]. This might be due to the different geometrical constraints (circular holes instead of trenches) and to the presence of defects before the annealing procedure, which clearly influence ripple characteristics. It is interesting to compare this effect with the influence of the boundary conditions on the orientation of ripples made on polymer such as the ones in Chapters 3 and 4. According to Napolitano and coworkers [70], in this case, the ripples tend to follow the boundary circular border even though the direction is also entangled with the one expected in the absence of constraints. Additionally, it is

important to note that the bigger the hole where the membrane is placed, the clearer ripples are induced due to the lower influence of boundaries as shown in Figure 58 for 3 and 10 µm diameters. Moreover, the features that appeared before thermal treatment in PeakForce™ adhesion and dissipation signals and UFM seems to disappear after the annealing. This supports the hypothesis of their contaminant nature because thermal heating has been also proved as a good cleaning methodology for this type of membranes.

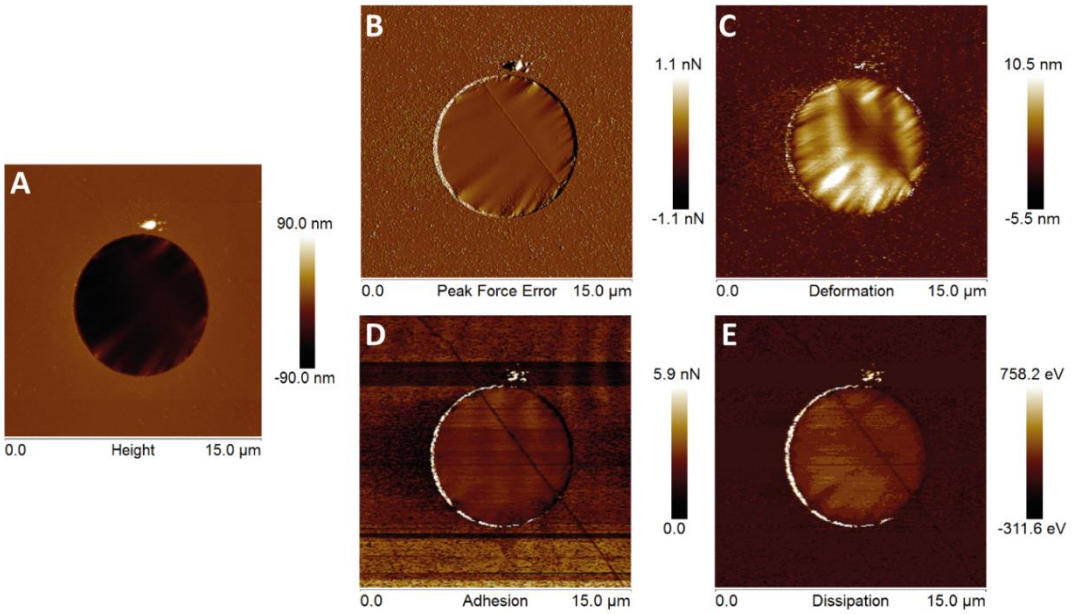


Figure 57. Graphene suspended membrane on a 8-µm-diameter hole after the thermal treatment, measured using PeakForce QNM™: (A) Topography, (B) Peak Force Error, (C) Deformation, (D) Adhesion and (E) Dissipation. The applied load is 1 nN.

As a result of this characterization we conclude that thermally-formed ripples are strongly influenced by flake defects as well as geometrical constraints of the circular holes. As a consequence, the ripple periodicity and corrugation vary inhomogeneously and no precise control on the roughness could be achieved by this technique, in the limited time of the stay, in order to investigate tribological response of these samples.

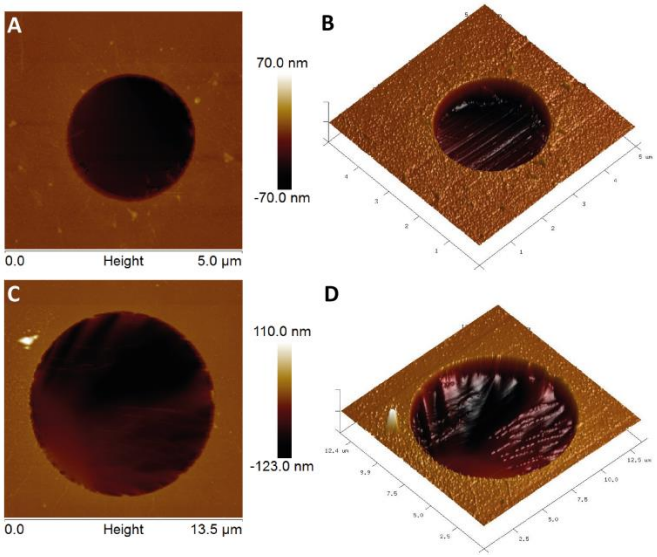


Figure 58. Suspended graphene membrane on a 3-µm-diameter hole after the thermal treatment (A) 2D and (B) 3D. Suspended graphene membrane on a 10-µm-diameter hole after the thermal treatment (C) 2D and (D) 3D.

Furthermore, it is important to note for future experiments that if large loads are applied while sliding, the ripples could disappear since they are formed because of strains and this effect could be reversible. Moreover, the application of large loads will be also challenging because of the apparent higher membrane fragility after the thermal treatment.

# 6.4. GRAPHENE ON COPPER

The second part of Chapter 6 is the continuation of previous works done in our group on atomic scale resolution and friction on mineral surfaces in liquid environments [174, 175] but in this case applied to graphene. Since the suspended graphene membranes are quite fragile for being immersed in water, supported graphene on copper is employed for experimental and theoretical calculations in this Section.

The lattice-resolved friction maps of a material results from a stick-slip movement of the probing tip on the crystal surface. However, atomic resolution in ambient conditions is difficult due to the presence of contaminants and, most important, water bridges formed between the tip and surface by capillary condensation, which are dragged during the scanning [202]. These problems can be reduced or avoided by performing FFM in UHV or, as a cheaper alternative approach, in liquid. However, to the best of our knowledge, nanotribology of graphene in liquid has been rarely investigated, e.g. by Robinson *et al.* [203] who characterized this material in a nonpolar liquid without achieving lattice resolution.

## 6.4.1. HIGH RESOLUTION FRICTION IMAGING IN WATER

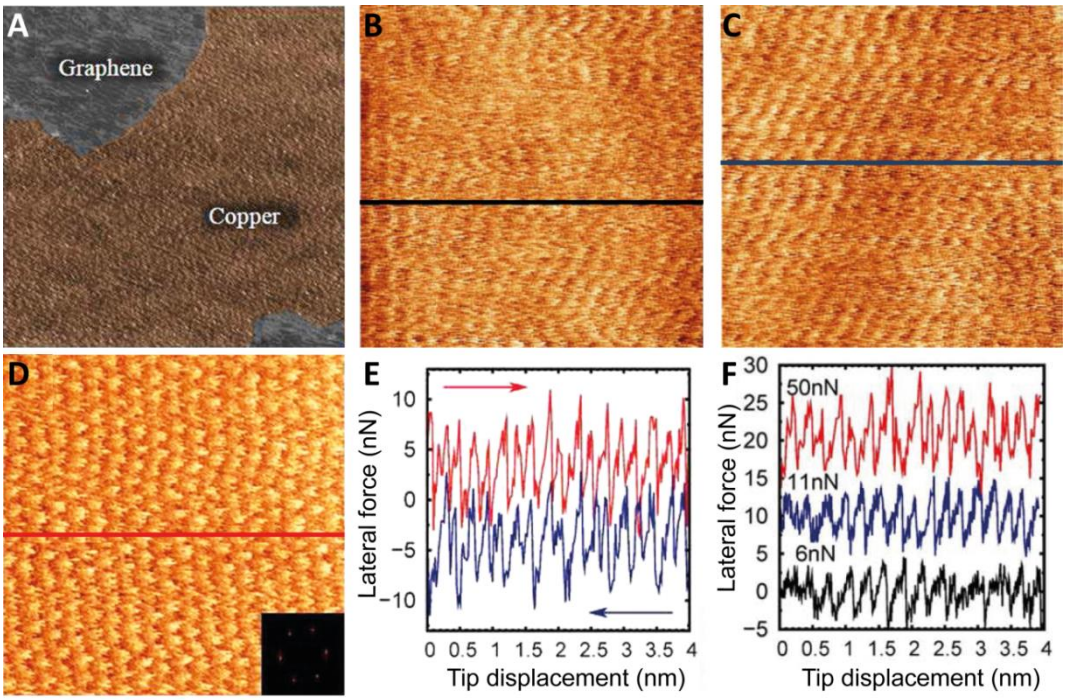


Figure 59. (A) AFM lateral force map in water (13.17 x 13.17 $\mu m^2$) of graphene islands on Cu. (B) High-resolution lateral force (4 x 4 $nm^2$) on a graphene island for a load $F_N$ = 6 nN. (C) Same for $F_N$ = 11 nN. (D) Same for $F_N$ = 50 nN. Inset in (D) shows the 2D FFT. (E) Cross-section showing the friction loop with the corresponding forward and backward scans along the red line in (D). (F) Profiles at different loads corresponding to forwards scans along the color lines in (B), (C) and (D).

In Figure 59, friction images of graphene on Cu obtained with a sharp AFM tip (SNL10D, Bruker) in water are shown. Those images were acquired with the set-up described in Section 2.3.2 in collaboration with Dr. Carlos Pina and Carlos Pimentel at Centro Nacional de Microscopía (Universidad Complutense de Madrid). Figure 59 (A) shows a lateral force map where two graphene islands can be distinguished from the Cu substrate. Those islands are grown in a carpet-like fashion on the copper steps. Furthermore, atomic resolution images (FFM) on the top of the graphene islands can be observed in Figure 59 (B-D) for three different loads: 6 nN (B), 11 nN (C) and 50 nN (D). Even though stick-slip is clearly visible in all the cases, its shape is more pronounced at the highest load as also detected in Figure 59 (E-F), where the friction loop in the latter case is shown, and, respectively, three forward cross-sections. Moreover, it is worthy to note that no lattice resolution could be obtained when performing the measurements in the same conditions but in air, due to the previously mentioned reasons.

Additionally, the average values of the lateral force ($F_L$) as a function of the applied normal force ($F_N$) at increasing and decreasing values of the load have been measured, for comparison, on the Cu substrate, on graphite and on the graphene layer on Cu. Those results are presented in Figure 60, where linear behaviour with no hysteresis is observed for all the cases, similarly to the result obtained on free-standing graphene in Section 6.3.1. Moreover, friction coefficients can be also estimated as the slope of the lines for the three different set of data. According to the calculations, the friction coefficient between the silicon tip and the graphene is $\mu_G$ = 0.058 ± 0.012 whereas the values on graphite and copper are $\mu_g$ = 0.048 ± 0.007 and $\mu_{Cu}$ = 0.36 ± 0.02, respectively. The low friction value on graphene compared to copper one as well as its decrease with the increasing number of layers (graphite) is consistent with previous reported results by other groups in air and UHV [190, 191].

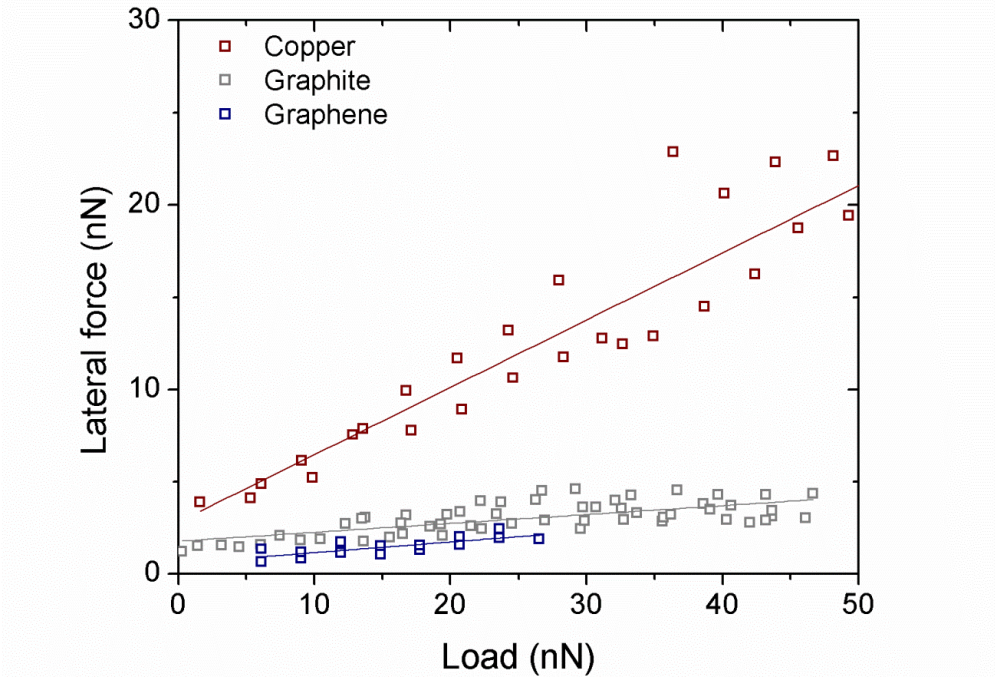


Figure 60. Lateral force vs applied normal load for copper, graphite and graphene.

## 6.4.2. MOLECULAR DYNAMICS SIMULATIONS

Despite the interesting atomic resolution results obtained by FFM in liquid, this technique is rarely used. Molecular dynamics (MD) simulations have been performed by Dr.

José Guilherme Vilhena and Prof. Rubén Pérez (Universidad Autónoma de Madrid) in collaboration with our group to understand the role of water in the high resolution imaging.

Sliding and indentation of a diamond tip (1 nm tip radius) on graphene in water and UHV are simulated by means of contact-velocity steered molecular dynamics (SMD) using AMBER software suite with NVIDIA GPU acceleration. It is important to note that a three-layer graphene sheet is used as a sample, where the bottom layer is kept fixed to mimic the rigid metal support in the experiments.

Figure 61 shows the lateral force curves at three applied loads (5, 10 and 20 nN) when simulating in vacuum (A) and in water (B). In vacuum environment, the sawtooth shape characteristic of the stick-slip mechanism is observed at 20 nN, and it is smoothed out at 10 nN and below, while the lattice periodicity remains clearly discernable (see Socoliuc *et al.* [55] for similar behaviour on alkali halide surfaces). Moreover, the mean friction obtained at the different loads is relatively low and barely increases with $F_N$, as observed in the experiments too. These trends are also consistent with previous experimental [204, 205] and theoretical [206] works in UHV.

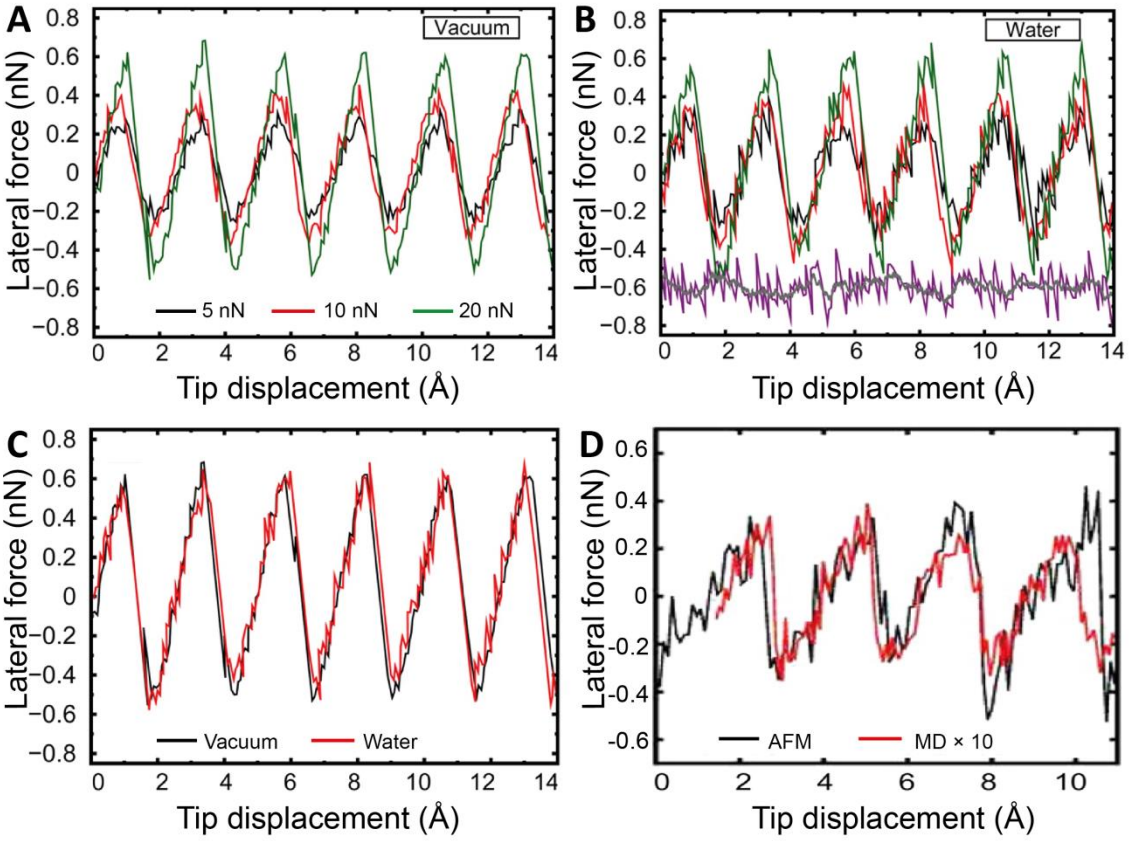


Figure 61. MD simulations of the lateral force as a function of the sliding distance at three different loads $F_N$: 5 nN (black), 10 nN (red) and 20 nN (green) under (A) vacuum and (B) in water. The purple and grey curves show the friction curve obtained while scanning over the first hydration layer and its moving average over 0.1 nm, respectively, according to the simulations. For clarity, those curves have been shifted by - 0.6 nN. (C) Comparison between simulated lateral force curves under vacuum and water at $F_N$ = 20 nN. (D) Comparison between the experimental lateral force curve of graphene on copper in water at $F_N$ = 6 nN and the corresponding MD simulation at $F_N$ = 5 nN (rescaled by a factor of 10).

In addition, the same experiment is simulated in water. The stick-slip mechanism is again observed and the contrast turns out to be analogous to the one obtained in vacuum. This

similarity can be better appreciated in Figure 61 (C), which shows that the only remarkable difference between vacuum and water lateral force curves is the larger fluctuations in the second case around the otherwise coincident values. Furthermore, simulation at the lowest load $F_N$ = 5 nN, simply multiplied by a factor of 10, perfectly matches the periodicity and friction values measured in the experiments at $F_N$ = 6 nN as shown in Figure 61 (D). The rescaling factor is required not only by the difference in contact area between the experiments and the simulation, but also by the discrepancies in tip shape and material, the slightly larger experimental operation load and that no attempt is made to match the relative tip/surface orientation.

Altogether, the experimental and theoretical results show that the effect of water on friction contrast is negligible. At this point, two interesting issues can be additionally addressed by MD. On the one hand, the possible role of water in the contact region and, on the other hand, the effect of the fluctuations induced by the collisions occurring between the tip and the surrounding water molecules.

In order to investigate the first issue, the contribution of hydration layers to the tip-sample interaction has to be considered. Figure 62 (A) shows simulated force-distance curves in both vacuum and water environments. Furthermore, snapshots of the tip approaching the surface at different loads are illustrated in Figure 62 (B-C). In those images, it is possible to observe that the tip is already in contact with the surface at very small normal force $F_N$ = 5 nN. By analyzing the force-distance curve in vacuum, three interaction regimes can be distinguished: weakly interacting (d > 6.5 Å), attractive (6.5 < d < 3.3 Å) and repulsive (d < 3.3 Å). However, in the water environment, two peaks on the force curve can be recognized superimposed to the previously mentioned regimes. According to literature [207, 208], these peaks arise due to the breaking of the second and first hydration layers formed over the graphene (Figure 62 (B-C)). Besides, the position of the hydration layers measured in the MD simulations matches with X-ray data [209]. These results confirm that these layers are broken at rather low applied normal force as previously reported using frequency-modulated AFM [207]. Thus, in our experiments where high resolution is achieved, the imaging is produced in direct mechanical contact between the tip and graphene. Furthermore, it is possible to study the friction signal in the low load regime before breaking the hydration layer. According to the simulations, the friction signal in these conditions seems to resemble mostly noise (Figure 61 (B) purple curve). However, when considering the average of the curve (in grey) the signal displays the same periodicity as graphene's hollows sites, even though the friction signal is very low (~0.1 nN).

On the other hand, a fluid dynamics analysis is required to understand the effect of water collisions on the tip. According to previous MD simulations of pure water [210], the viscosity as a function of time saturates in less than 1 ps. Moreover, considering that the largest movement of the tip in 1 ps is 0.012 Å (during the slip phase), this would imply that in the time that one water molecule loses its stress memory, the tip barely moves. In fact, MD simulations show that only 5 % of the water molecules initially in contact with the tip remain within the interacting distance. Hence, the stress imposed on the tip by water fluctuations from purely random collisions results in a null stress sum. These random fluctuations can be

appreciated in the slight increase in the friction force fluctuations measured in water in comparison with the ones in vacuum at the same load (Figure 61 (C)).

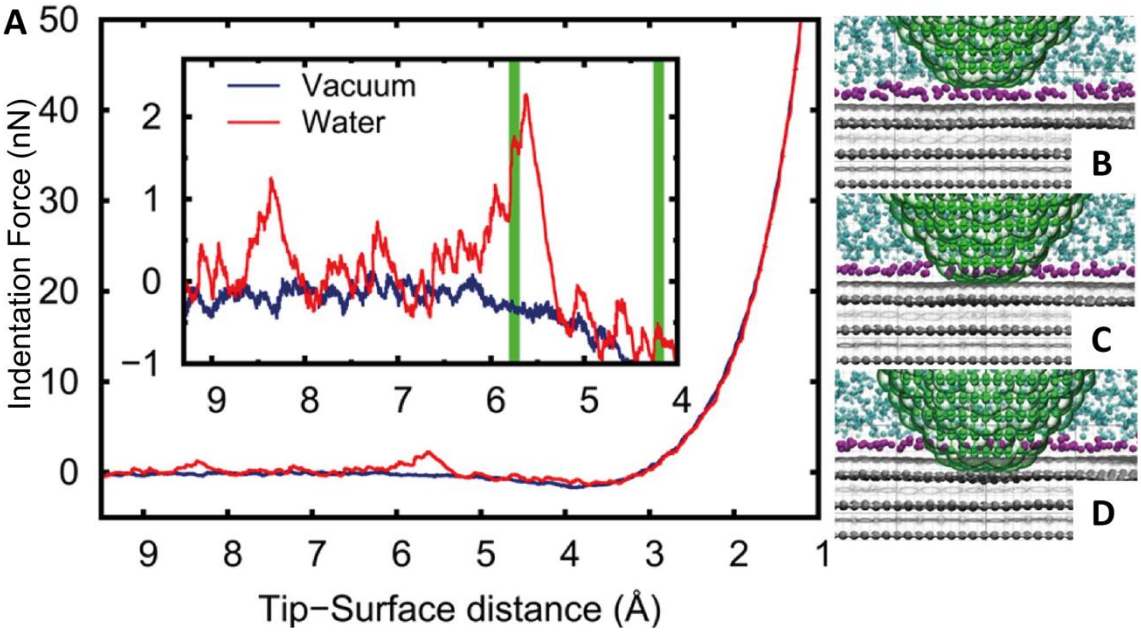


Figure 62. Indentation simulations in water. (A) Force felt by the tip as function of the tip-surface distance. The inset highlights the force peaks associated with the breaking of the hydration layers. The green vertical lines correspond to (B) and (C) steps. Ball and stick models of the atomic configurations at different normal loads: (B) over the first hydration layer, (B) just before breaking it, (C) FN = 5 nN. Gray, green, cyan and purple represent graphene, diamond-tip, water and first hydration layer water oxygen atoms, respectively. Besides, the van der Waals surface ($r = \sigma_{cc}/2 = 1.65$ Å) of the tip and the surface is represented in green and grey.

# 6.5. CONCLUSIONS AND NEXT STEPS

In this Chapter, different aspects of nanotribology of copper-supported and free standing graphene membranes have been studied following different approaches in two environments: air and water.

First of all, we focus the research on suspended graphene membranes placed on the top of holes on a silicon nitride membrane. The goal is to induce large ripples on graphene membranes in order to study differences in tribological properties induced by changes in local topography.

As a first step, free standing graphene membranes are generally characterized by PeakForce™. The obtained results are consistent with similar ones reported in literature. Furthermore, UFM measurements shows features also present in adhesion and dissipation signals, which are presumably caused by contaminants or defects on the membranes.

Additionally, the frictional behaviour on flat suspended membranes is very similar to the one registered on graphene on copper, with a linear tendency with no hysteresis. The friction coefficient in this case is 0.08, also in the same range of previous reports.

Wrinkles on the free standing graphene membranes are obtained by a thermal treatment consisting in a fast heating in vacuum up to 400 ºC for 5 min followed by a fast

cooling down in nitrogen and after that in air. It is during the latter one when the rippling formation occurs. The reasons for that are, on the one hand, the graphene negative thermal expansion coefficient and, on the other hand, that out of plane bending is energetically favored over in plane compression in thin elastic sheets leading to regular periodic wrinkles or disordered crumples.

After the annealing, ripples are clearly observed in topography, PeakForce™ error and deformation signals. However, ripple formation seems to depend not only on the geometrical constraints of the holes but also on the defects previous to the thermal treatment. As a result, the obtained ripples have not enough homogenous characteristics to compare their tribological behaviour with the samples previous to the annealing or to perform atomic scale friction on them.

Furthermore, it is important to note that the annealing process is also an effective method for cleaning the membrane of residual PMMA used in the preparation method we adopted. In fact, after thermal treatment features previously observed in adhesion and dissipation signals are not there anymore. Nonetheless, the thermal treatment seems to make the membrane more fragile. It is also not excluded that, since ripple formation is reversibly induced by strains during the thermal treatment, ripples could disappear if large loads are applied while sliding the tip.

Regarding other future work, more experiments should be carried out in order to investigate how hole geometrical constraints influence tribological and mechanical properties of the membrane by means of PeakForce™, UFM and force spectroscopy. Furthermore, regular ripples on trenches instead of holes could be also used to investigate frictional anisotropy depending on the ripple orientation.

Finite element simulations could be also very helpful for studying the different vibrations modes of the suspended membranes, their dependence on membrane defects and geometry and their possible role in lubricant properties of free standing graphene.

In the second part of this Chapter, friction force microscopy experiments of graphene on copper are performed in water obtaining atomic resolution with improved stick-slip contrast with increasing load. Furthermore, linear tendencies without hysteresis are observed in lateral force vs applied load graphs for graphene, graphite and copper. The friction coefficient of graphene on copper ($\mu_G$) is also estimated to be about 0.06. This low value together with the graphite one are in agreement with previous results in air and UHV.

Additionally, our results are compared to MD simulations of a diamond tip sliding on graphene in water and UHV. According to them, stick-slip mechanism is observed at very low loads in accordance with the experimental results. Moreover, atomic stick-slip is expected to be almost identical to the one found in UHV, promoting water as an efficient alternative to ultrahigh vacuum for reliable high resolution imaging.

Last but not least, MD simulations are also very helpful to fully understand the role of water in high resolution FFM. Firstly, they demonstrate that for the load values at which lattice resolution is achieved in the experiments, the tip and the substrate are in full mechanical

contact and the hydration layers on the top of the graphene are broken. In addition, simulations also predict that the surrounding water plays a purely stochastic role in FFM due to the fact that water molecules lose their force memory much faster than the sliding of the tip occurs.

# GENERAL CONCLUSIONS

# GENERAL CONCLUSIONS

In this thesis the rippling of various solid surfaces has been investigated in connection to friction, wear and adhesion processes at different length scales. This goal has been reached with the help of atomic force microscopy (AFM) under different operation conditions. The main conclusions of this work are described in the following.

Polymer thin films easily form wrinkle patterns when an AFM tip slides over their surface as a result of the corrugation induced by the tip indentation and lateral motion. A series of measurements on toluene-enriched polystyrene have been interpreted within an original model with some analogies to the Prandtl-Tomlinson one for atomic-scale sliding friction. The key parameters are the indentation rate, the scan rate, the tip width and the lateral spring constant. Depending on the parameter values, a transition from surface rippling to wearless sliding is expected and experimentally observed.

Furthermore, the surface damage produced as rippling on polymers is successfully reduced on the nanoscale by applying out of plane ultrasonic vibrations during sliding. The effect of the mechanical vibrations is enhanced when the excitation frequency is around the resonance frequency of the contact and the amplitude of the vibrations increases. Under the same conditions, friction also diminishes.

As a result of this work, not only a good control on the wear and friction on polymers on the nanoscale is achieved but also a better understanding of AFM nanopatterning process, the so-called nanolithography.

In a different context, we have studied the nanoripples created over large glass areas by defocused ion beam sputtering and investigated how their anisotropy influences the adhesion behaviour of much larger structures such as neural stem cells (NSCs). Since characteristic width of the ripples and the cell filopodia are in the same range, the latter ones undergo a trapping effect and preferentially aligned parallel or perpendicular to the nanopatterns. Consequently, the local adhesion increases in those points. However, the cell global adhesion decreases as a result of the local pinning, preventing the cells to spread out and considerably modifying the structure and morphology of NSCs. These results encourage the possible use of these substrates as scaffolds to control adhesion, orientation and morphological changes of NSCs (and possibly other biosystems) without chemical modifications of the surface.

Finally, nanotribology of graphene, either supported on copper or as free-standing membrane, has been explored in water and air environments, respectively. In line with the main subject of the thesis, the formation of large inhomogeneous ripples on circular suspended graphene membranes could be induced during the cooling down of a thermal treatment. Also interestingly, the friction coefficients for flat graphene are of the same order of magnitude in both environments (whereas systematic investigation of wrinkled membranes was not possible). Last but not least, atomic resolution could be readily obtained on friction force images of graphene in water. This is explained by molecular dynamics simulations showing that the role of water in atomic scale friction is purely stochastic. In this way, friction

force microscopy in liquid appears as a reliable and relatively low-cost technique for high resolution imaging of solid surfaces.

# CONCLUSIONES GENERALES

En esta tesis las ondulaciones creadas en varias superficies sólidas han sido investigadas en conexión con procesos de fricción, desgaste y adhesión a diferentes escalas. Este objetivo se ha alcanzado con ayuda de la microscopía de fuerzas atómicas (*AFM*), bajo diferentes condiciones de operación. Las principales conclusiones de este trabajo se describen a continuación.

Las películas delgadas de polímero forman fácilmente patrones ondulados cuando una punta de AFM se desliza sobre su superficie como resultado de la corrugación inducida por la indentación de la punta y su movimiento lateral. De esta manera, se han realizado una serie de medidas sobre poliestireno enriquecido en tolueno, que han sido interpretadas con un original modelo que presenta analogías con el de Prandtl-Tomlinson comúnmente utilizado para describir la fricción a escala atómica. Los parámetros clave del mismo son la velocidad de indentación, la velocidad de escaneo, el ancho de la punta y la constante de fuerza lateral. Dependiendo de los valores de dichos parámetros, el modelo muestra una transición desde la formación de las estructuras onduladas en la superficie hasta el deslizamiento de la punta sin desgaste, que también se observa experimentalmente.

Además, el daño producido en forma de ondulación en la superficie polimérica se reduce exitosamente en la nanoescala aplicando vibraciones ultrasónicas fuera de plano durante el deslizamiento de la punta. El efecto de las vibraciones mecánicas aumenta cuando la frecuencia de excitación se encuentra en torno a la frecuencia de resonancia en contacto y la amplitud de las vibraciones aumenta. En estas mismas condiciones, la fricción también disminuye.

Como resultado de este trabajo, no solamente se logra un buen control del desgaste y la fricción de polímeros a escala nanométrica, sino también una mejor compresión de los procesos de nanolitografía mediante AFM.

En un contexto diferente, se han estudiado nanoestructuras onduladas creadas sobre amplias superficies de vidrio mediante bombardeo deslocalizado de iones, investigando cómo su anisotropía influye en la adhesión de sistemas mucho más grandes como células madre neuronales. Dado que el ancho característico tanto de dichos patrones ondulados como de los filopodios de las células se encuentran en el mismo rango de escala, éstos últimos quedan atrapados, alineándose preferentemente de forma paralela o perpendicular a la dirección de ondulación. En consecuencia, la adhesión local se incrementa en dichos puntos. Sin embargo, la adhesión global de la célula disminuye como resultado de dicha fijación local, impidiendo que las células se diseminen y modificando considerablemente la estructura y la morfología de las mismas. Los resultados obtenidos promueven el posible uso de estos sustratos con el objetivo de controlar los cambios en la adhesión, la orientación y la morfología de las células madre neuronales (y posiblemente de otros biosistemas) sin modificaciones químicas en la superficie de los mismos.

Finalmente, se ha estudiado la nanotribología del grafeno ya sea sobre cobre o como membrana suspendida en agua y en aire, respectivamente. En línea con el tema principal de la

tesis, se ha podido inducir la formación de grandes ondulaciones no homogéneas en membranas suspendidas circulares de grafeno durante el enfriamiento de un tratamiento térmico. Curiosamente, los coeficientes de fricción en el caso del grafeno plano son del mismo orden de magnitud en ambos ambientes (mientras que la investigación sistemática de las membranas con ondulaciones no ha sido posible). Por último, pero no por ello menos importante, se han podido obtener imágenes de resolución atómica de grafeno mediante microscopía de fuerza lateral en agua. Esto es posible, tal y como se ha demostrado mediante simulaciones de dinámica molecular, porque el papel del agua en este tipo de medidas es puramente estocástico. De esta manera, la microscopía de fuerza lateral en líquido parece ser una técnica fiable y de coste relativamente bajo para la obtención de imágenes de alta resolución de superficies sólidas.

# APPENDIX

# APPENDIX I: PRANDTL-TOMLINSON MODEL

The Prandtl-Tomlinson (PT) model [28, 211], proposed in the early 1920's, is the most adequate model for the description of nanoscale friction. In spite of its simplicity, it reproduces the main characteristics of the stick-slip motion of a particle resembling a single asperity of a rough surface elastically driven on a countersurface.

The PT model considers a point mass (tip) being dragged along a corrugated substrate potential $U_{int}$ by a rigid support via a spring of effective stiffness $k_{eff}$ (see below) and with a constant velocity $v$ (Figure 63 (A)). If the x axis is oriented along the direction of motion, the equation of motion of the tip is (at zero temperature):

$$m\ddot{x} + m\gamma\dot{x} + k_{eff}\,(x - vt) + U'_{int}(x) = 0$$

Equation 21

where: $\gamma$ is the damping coefficient describing the coupling with phonons and (for metal surfaces) electron hole pairs excited in the substrate during sliding.

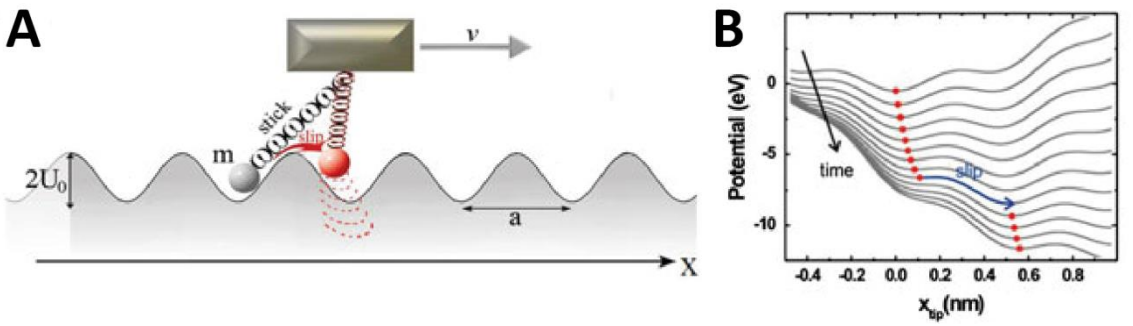


Figure 63. (A) Scheme of the tip movement in a sinusoidal interaction potential based on the Prandtl – Tomlinson model. A point-like tip is coupled elastically to the body by a spring with spring constant $k$ in x direction. For sliding, the body is moved with a velocity $v$ in x direction. (B) Temporary sequence of $U_{tot}$ and the corresponding position of the tip (red dots) capturing a stick-slip instability ($\eta$ =3.2). Both images reproduced from [212].

Neglecting the inertia of the point mass (i.e. assuming very slow driving velocities), the total energy of the system is expressed by the sum of the $U_{int}$ (depending on the normal load, on the chemical composition of the material in contact and the atomic arrangement at the tip end) and the elastic energy stored in the spring:

$$U_{total}\,(x,t) = U_{int}(x) + \frac{1}{2}\,k_{eff}\,(x - vt)^2$$

Equation 22

Considering a sinusoidal interaction potential, the total energy simplifies to:

$$U_{total}\,(x,t) = -U_0 \cos\frac{2\pi x}{\lambda} + \frac{1}{2}\,k_{eff}\,(x - vt)^2$$

Equation 23

where: $U_0$ = Half the peak to peak amplitude of the tip-sample potential,

$\lambda$ = period of the tip-substrate potential.

As a result, $U_{tot}$ has the form of a corrugated parabola, whose shape depends on the tip and support position (Figure 63 (B)). The tip is located in the minimum of $U_{tot}$ ($x = x_{min}$) obtained as the solution of $\partial U_{tot}/\partial x = 0$ with the stability condition $\partial^2 U_{tot}/\partial x^2 > 0$ :

$$\frac{\partial U_{tot}}{\partial x} = \frac{2\pi U_0}{\lambda}\sin\frac{2\pi x}{\lambda} + k_{eff}(x - vt) = 0$$

Equation 24

Using the approximation $\sin\alpha \approx \alpha$ in previous equation, it is possible to obtain the initial velocity of the tip:

$$v_{tip}\,(0) = \left.\frac{dx_{min}}{dt}\right|_{t\to 0} = \frac{v}{1+\eta}$$

Equation 25

where: $\eta$ = Dimensionless parameter that reflects the ratio between the strength of the surface potential and the spring energy given by the following equation:

$$\eta = \frac{4\pi^2 U_0}{k_{eff}\lambda^2}$$

Equation 26

When the support starts moving over the surface, the spring extends which results in a growing lateral force and a flattening of the local minima. The tip becomes unstable and experiences an elastic instability at the position $x_{min} = x_0$, where it jumps to the next stable position. This occurs when $\partial^2 U_{tot}/\partial x^2 = 0$ :

$$x_0 = \frac{\lambda}{2\pi}\arccos(-\frac{1}{\eta})$$

Equation 27

The lateral force which induces the jump ($F^* = -k_{eff}(x_0 - vt)$), can be evaluated taking into account the first and the second derivatives of $U_{tot}$ and using the identity $cos^2\alpha + sin^2\alpha = 1$:

$$F^* = \frac{k_{eff}\lambda}{2\pi}\sqrt{\eta^2 - 1}$$

Equation 28

It is interesting to note that this force is slightly lower than the maximum force $F_L^{max} = (k_{eff}\lambda/2\pi)\eta$, which is reached slightly before hopping. In addition it is possible to obtain $U_o$ as:

$$U_0 \approx \frac{\lambda F_L^{max}}{2\pi}$$

Equation 29

According to Equation 28, instabilities and hence stick-slip only occur if $\eta$>1 (soft cantilever or strong-tip-sample interaction). In this case, a hysteretic friction loop is observed while scanning forth and back along the same line and its area represents the energy dissipated in the process. On the other hand, for $\eta$<1, the elastic instabilities and related

dissipation are suppressed. In this case, the tip smoothly follows the surface potential in an oscillatory way and a “superlubric” state is reached.

Moreover, it is important to notice that the effective stiffness $k_{eff}$ corresponds to a series of three springs associated to the torsion of the cantilever and the lateral deflection of the tip apex and surface. When $\eta$ is large, it basically corresponds to the sticking slope ($k_{exp}$) at the beginning of the friction loop. However, when $\eta$ approaching 1, the relation has to be corrected to $k_{eff} = (1 + (1/\eta))k_{exp}$ [212].

Finally, it is worthy to mention that this model can be also extended to 2D such as in the work previously developed in our group by Gnecco and coworkers [213].

# REFERENCES


1. Jost, H.P., *The Jost Report*. 1966, Department of Education and Science, UK.
2. Mate, C.M., *Tribology on the small scale: A bottom up approach to friction, lubrication and wear*. Mesoscopic physics and nanotechnology, ed. H.G. Craighead, et al. Vol. 6. 2008: Oxford University Press.
3. Bhushan, B., *Handbook of Micro/Nanotribology*. Second ed. The mechanics and material science. 1999: CRC Press. 859.
4. Popov, V.L., *Contact Mechanics and Friction: Physical Principles and Applications*. First ed. 2010, Berlin: Springer. 359.
5. Bhushan, B., *Introduction to tribology*. Second ed. Tribology. 2013: John Wiley & Sons, Ltd.
6. Tzanakis, I., et al., *Future perspectives on sustainable tribology.* Renewable & Sustainable Energy Reviews, 2012. **16**(6): p. 4126-4140.
7. Holmberg, K. and A. Erdemir, *Global impact of friction and energy consumption, economy and environment.* FME Transactions, 2015. **43**(3): p. 5.
8. España, B.N.d. *Los Códices de Madrid*. 2011 [cited 2017 02-01-2017]; Available from: http://www.bne.es/es/Colecciones/Manuscritos/Leonardo/.
9. Persson, B.N.J., *Theory of rubber friction and contact mechanics.* The Journal of Chemical Physics, 2001. **115**(8): p. 3840-3861.
10. Persson, B.N.J., *Contact mechanics for randomly rough surfaces.* Surface Science Reports, 2006. **61**(4): p. 201-227.
11. Webwizzard. *Powder skiing in Chamonix Mont Blanc*. 2016 [cited 2016 22/11/2016]; Available from: https://upload.wikimedia.org/wikipedia/commons/2/26/Powder_skiing_in_Chamonix_Mont_Blanc.JPG.
12. Beauford, J. *Ripples in sand dunes*. 2016 [cited 2016 22/11/2016]; Available from: http://www.publicdomainpictures.net/view-image.php?image=167806&picture=ripples-in-the-sand-dunes.
13. Spector, D. *Why train tracks buckle in extreme heat*. 2013 [cited 2016 22/11/2016 ]; Available from: http://www.businessinsider.com/why-train-tracks-buckle-in-extreme-heat-2013-7.
14. Nishimori, H. and N. Ouchi, *Formation of ripple patterns and dunes by wind-blown sand.* Physical Review Letters, 1993. **71**(1): p. 197-200.
15. Aste, T. and U. Valbusa, *Ripples and ripples: from sandy deserts to ion-sputtered surfaces.* New Journal of Physics, 2005. **7**(1): p. 122.
16. Finnie, I. and Y.H. Kabil, *On the formation of surface ripples during erosion.* Wear, 1965. **8**(1): p. 60-69.
17. Enrico Gnecco and Ernst, M., *Elements of Friction Theory and Nanotribology*. 2015: Cambridge University Press.
18. Buividas, R., L. Rosa, and J. Remigijus Šliupas and Tadas Kudrius and Gintas Šlekys and Vitaly Datsyuk and Saulius, *Mechanism of fine ripple formation on surfaces of (semi)transparent materials via a half-wavelength cavity feedback.* Nanotechnology, 2011. **22**(5): p. 055304.
19. Howland, R. and L. Benatar, *A practical guide to scanning probe microscopy*. First ed. 2000: Diane Publishing Company.
20. Binning, G., et al., *SURFACE STUDIES BY SCANNING TUNNELING MICROSCOPY.* Physical Review Letters, 1982. **49**(1): p. 57-61.

21. Bhushan, B. and O. Marti, *Scanning Probe Microscopy: Principle of operation, instrumentation and probes*, in *Handbook of Nanotechnology*, B. Bhushan, Editor. 2007, Springer.
22. Binnig, G., C.F. Quate, and C. Gerber, *ATOMIC FORCE MICROSCOPE.* Physical Review Letters, 1986. **56**(9): p. 930-933.
23. Kaupp, G., *Atomic force microscopy, scanning nearfield optical microscopy and nanoscratching*. First ed. NanoScience and Technology, ed. P. Avouris, et al. 2006: Springer. 301.
24. Bhushan, B., *Scanning probes microscopy in nanoscience and nanotechnology*. First ed. Nanoscience and Technology. Vol. 3. 2013: Springer. 630.
25. Salapaka, S.M. and M.V. Salapaka, *Scanning probe microscopy.* Ieee Control Systems Magazine, 2008. **28**(2): p. 65-83.
26. Eaton, P. and P. West, *Atomic Force Microscopy*. First ed. 2010: Oxford University Press 248.
27. Mate, C.M., et al., *ATOMIC-SCALE FRICTION OF A TUNGSTEN TIP ON A GRAPHITE SURFACE.* Physical Review Letters, 1987. **59**(17): p. 1942-1945.
28. Tomlinson, G.A., *A molecular theory of friction.* Philosophical Magazine, 1929. **7**(46): p. 905-939.
29. Bennewitz, R., *Friction Force Microscopy*, in *Fundamentals of Friction and Wear on the Nanoscale*, E. Gnecco and E. Meyer, Editors. 2015, Springer. p. 3-16.
30. Carpick, R.W., D.F. Ogletree, and M. Salmeron, *Lateral stiffness: A new nanomechanical measurement for the determination of shear strengths with friction force microscopy.* Applied Physics Letters, 1997. **70**(12): p. 1548-1550.
31. Lantz, M.A., et al., *Atomic-force-microscope study of contact area and friction on ${\mathrm{NbSe}}_{2}$.* Physical Review B, 1997. **55**(16): p. 10776-10785.
32. Pittenger, B., et al., *Quantitative Mechanical Property Mapping at the Nanoscale with PeakForceQNM*. 2010, Veeco Instruments.
33. Maugis, D., *Contact, adhesion and rupture of elastic solids*. Solid State Science. 2000, Berlin: Springer.
34. Marinello, F., Daniele and E. Savio, *Acoustic Scanning Probe Microscopy*. Nanoscience and Technology. 2013: Springer. 494.
35. Rabe, U. and W. Arnold, *ACOUSTIC MICROSCOPY BY ATOMIC-FORCE MICROSCOPY.* Applied Physics Letters, 1994. **64**(12): p. 1493-1495.
36. Rabe, U., K. Janser, and W. Arnold, *Vibrations of free and surface-coupled atomic force microscope cantilevers: Theory and experiment.* Review of Scientific Instruments, 1996. **67**(9): p. 3281-3293.
37. Rupp, D., et al., *Nonlinear contact resonance spectroscopy in atomic force microscopy.* Journal of Physics D-Applied Physics, 2007. **40**(22): p. 7136-7145.
38. Arnold, W., *Force Modulation*, in *Encyclopedia of Nanotechnology*, B. Bhushan, Editor. 2012, Springer.
39. Rabe, U., et al., *Evaluation of the contact resonance frequencies in atomic force microscopy as a method for surface characterisation (invited).* Ultrasonics, 2002. **40**(1-8): p. 49-54.
40. Hurley, D.C., et al., *Quantitative elastic-property measurements at the nanoscale with atomic force acoustic microscopy.* Advanced Engineering Materials, 2005. **7**(8): p. 713-718.
41. Yuya, P.A., D.C. Hurley, and J.A. Turner, *Contact-resonance atomic force microscopy for viscoelasticity.* Journal of Applied Physics, 2008. **104**(7).
42. Kolosov, O. and K. Yamanaka, *NONLINEAR DETECTION OF ULTRASONIC VIBRATIONS IN AN ATOMIC-FORCE MICROSCOPE.* Japanese Journal of Applied Physics Part 2-Letters, 1993. **32**(8A): p. L1095-L1098.

43. Dinelli, F., et al., *Mapping surface elastic properties of stiff and compliant materials on the nanoscale using ultrasonic force microscopy.* Philosophical Magazine a-Physics of Condensed Matter Structure Defects and Mechanical Properties, 2000. **80**(10): p. 2299-2323.
44. Ohler, B. *Application Note 94: Practical advice on the determination of cantilever spring constants*. 2010. 12.
45. Hutter, J.L. and J. Bechhoefer, *CALIBRATION OF ATOMIC-FORCE MICROSCOPE TIPS (VOL 64, PG 1868, 1993).* Review of Scientific Instruments, 1993. **64**(11): p. 3342-3342.
46. Butt, H.J. and M. Jaschke, *CALCULATION OF THERMAL NOISE IN ATOMIC-FORCE MICROSCOPY.* Nanotechnology, 1995. **6**(1): p. 1-7.
47. Luthi, R., et al., *NANOTRIBOLOGY - AN UHV-SFM STUDY ON THIN-FILMS OF C-60 AND AGBR.* Surface Science, 1995. **338**(1-3): p. 247-260.
48. Nonnenmacher, M., et al., *SCANNING FORCE MICROSCOPY WITH MICROMACHINED SILICON SENSORS.* Journal of Vacuum Science & Technology B, 1991. **9**(2): p. 1358-1362.
49. Noy, A., et al., *CHEMICAL FORCE MICROSCOPY - EXPLOITING CHEMICALLY-MODIFIED TIPS TO QUANTIFY ADHESION, FRICTION, AND FUNCTIONAL-GROUP DISTRIBUTIONS IN MOLECULAR ASSEMBLIES.* Journal of the American Chemical Society, 1995. **117**(30): p. 7943-7951.
50. NT-MDT. *Ntegra Prima*. Available from: https://www.ntmdt.com/modular-afm/prima.
51. Electrónica, C.N.d.M. *AFM microscope*. 12/09/2016]; Available from: http://www.cnme.es/.
52. JPK. *Nanowizard II*. 12/09/2016]; Available from: http://www.jpk.com/.
53. Bruker. *Dimension Icon*. Available from: https://www.bruker.com.
54. Horcas, I., et al., *WSXM: A software for scanning probe microscopy and a tool for nanotechnology.* Review of Scientific Instruments, 2007. **78**(1).
55. Socoliuc, A., et al., *Transition from stick-slip to continuous sliding in atomic friction: Entering a new regime of ultralow friction.* Physical Review Letters, 2004. **92**(13).
56. Bagnold, R., *The physics of blown sand and desert dunes*. 1974: Springer.
57. Schallamach, A., *How does rubber slide?* Wear, 1971. **17**(4): p. 301-312.
58. Koudine, A.A. and M. Barquins, *On the influence of rubber thickness on the existence of Schallamach waves.* International Journal of Adhesion and Adhesives, 1997. **17**(2): p. 107-110.
59. Andersson, M., et al., *Formation of gold nanowires through self-assembly during scanning force microscopy.* Applied Physics A, 1999. **68**(5): p. 609-614.
60. Socoliuc, A., et al., *Ripple formation induced in localized abrasion.* Physical Review B, 2003. **68**(11).
61. Teichert, C., *Self-organization of nanostructures in semiconductor heteroepitaxy.* Physics Reports-Review Section of Physics Letters, 2002. **365**(5-6): p. 335-432.
62. Leung, O.M. and M.C. Goh, *ORIENTATIONAL ORDERING OF POLYMERS BY ATOMIC FORCE MICROSCOPE TIP-SURFACE INTERACTION.* Science, 1992. **255**(5040): p. 64-66.
63. Schmidt, R.H., G. Haugstad, and W.L. Gladfelter, *Correlation of nanowear patterns to viscoelastic response in a thin polystyrene melt.* Langmuir, 1999. **15**(2): p. 317-321.
64. Schmidt, R.H., G. Haugstad, and W.L. Gladfelter, *Scan-induced patterning in glassy polymer films: Using scanning force microscopy to study plastic deformation at the nanometer length scale.* Langmuir, 2003. **19**(3): p. 898-909.
65. Wang, X.P., M.M.T. Loy, and X.D. Xiao, *Bundle structure formation on a polymer film at various temperatures and scanning velocities.* Nanotechnology, 2002. **13**(4): p. 478-483.
66. Gotsmann, B. and U. Durig, *Thermally activated nanowear modes of a polymer surface induced by a heated tip.* Langmuir, 2004. **20**(4): p. 1495-1500.

67. Gnecco, E., et al., *Linear ripples and traveling circular ripples produced on polymers by thermal AFM probes.* Physical Review B, 2009. **79**(23).
68. Rice, R.H., et al., *Local Thermomechanical Analysis of a Microphase-Separated Thin Lamellar PS-b-PEO Film.* Langmuir, 2012. **28**(37): p. 13503-13511.
69. D'Acunto, M., et al., *Fast formation of ripples induced by AFM. A new method for patterning polymers on nanoscale.* Materials Letters, 2007. **61**(14-15): p. 3305-3309.
70. Napolitano, S., et al., *Ordered rippling of polymer surfaces by nanolithography: influence of scan pattern and boundary effects.* Nanotechnology, 2012. **23**(47).
71. Leach, R.N., et al., *Nanometer-scale solvent-assisted modification of polymer surfaces using the atomic force microscope.* Langmuir, 2003. **19**(24): p. 10225-10232.
72. D'Acunto, M., F. Dinelli, and P. Pingue, *Nanoscale rippling on polymer surfaces induced by AFM manipulation.* Beilstein Journal of Nanotechnology, 2015. **6**: p. 2278-2289.
73. Elkaakour, Z., et al., *BUNDLE FORMATION OF POLYMERS WITH AN ATOMIC-FORCE MICROSCOPE IN CONTACT MODE - A FRICTION VERSUS PEELING PROCESS.* Physical Review Letters, 1994. **73**(24): p. 3231-3234.
74. Iwata, F., T. Matsumoto, and A. Sasaki, *Local elasticity imaging of nano bundle structure of polycarbonate surface using atomic force microscopy.* Nanotechnology, 2000. **11**(1): p. 10-15.
75. Lea, A.S., et al., *MANIPULATION OF PROTEINS ON MICA BY ATOMIC FORCE MICROSCOPY.* Langmuir, 1992. **8**(1): p. 68-73.
76. Dinelli, F., G.J. Leggett, and P.H. Shipway, *Nanowear of polystyrene surfaces: molecular entanglement and bundle formation.* Nanotechnology, 2005. **16**(6): p. 675-682.
77. Hall, D.B., P. Underhill, and J.M. Torkelson, *Spin coating of thin and ultrathin polymer films.* Polymer Engineering and Science, 1998. **38**(12): p. 2039-2045.
78. Gotsmann, B., et al., *Controlling Nanowear in a Polymer by Confining Segmental Relaxation.* Nano Letters, 2006. **6**(2): p. 296-300.
79. Sun, Y., et al., *Effect of the Molecular Weight on Deformation States of the Polystyrene Film by AFM Single Scanning.* Scanning, 2013. **35**(5): p. 308-315.
80. Rao, A., et al., *The analytical relations between particles and probe trajectories in atomic force microscope nanomanipulation.* Nanotechnology, 2009. **20**(11).
81. Sun, Y., et al., *3D polymer nanostructures fabrication by AFM tip-based single scanning with a harder cantilever.* Tribol Int, 2012. **47**.
82. Johnson, K.L., *Contact Mechanics*. Ninth ed. 1987, Cambridge: Cambrigde University Press. 452.
83. MatWeb. *MatWeb*. 13/09/2016]; Available from: http://www.matweb.com/.
84. Oliver, W.C. and G.M. Pharr, *AN IMPROVED TECHNIQUE FOR DETERMINING HARDNESS AND ELASTIC-MODULUS USING LOAD AND DISPLACEMENT SENSING INDENTATION EXPERIMENTS.* Journal of Materials Research, 1992. **7**(6): p. 1564-1583.
85. Taljat, B. and G.M. Pharr, *Development of pile-up during spherical indentation of elastic–plastic solids.* International Journal of Solids and Structures, 2004. **41**(14): p. 3891-3904.
86. Tranchida, D., et al., *Nanoscale mechanical characterization of polymers by atomic force microscopy (AFM) nanoindentations: viscoelastic characterization of a model material.* Measurement Science and Technology, 2009. **20**(9).
87. Gnecco, E., et al., *Linear ripples and traveling circular ripples produced on polymers by thermal AFM probes.* Phys Rev B, 2009. **79**.
88. Beake, B.D., P.H. Shipway, and G.J. Leggett, *Influence of mechanical properties on the nanowear of uniaxially oriented poly(ethylene terephthalate) film.* Wear, 2004. **256**(1–2): p. 118-125.
89. Urbakh, M., et al., *The nonlinear nature of friction.* Nature, 2004. **430**(6999): p. 525-528.

90. D'Acunto, M., F. Dinelli, and P. Pingue, *Nanowear of Polymers*, in *Fundamentals of friction friction and wear on the nanoscale*, E. Gnecco and E. Meyer, Editors. 2015, Springer: London.
91. Fridman, H.D. and P. Levesque, *REDUCTION OF STATIC FRICTION BY SONIC VIBRATIONS.* Journal of Applied Physics, 1959. **30**(10): p. 1572-1575.
92. Akay, A., *Acoustics of friction.* Journal of the Acoustical Society of America, 2002. **111**(4): p. 1525-1548.
93. Teidelt, E., J. Starcevic, and V.L. Popov, *Influence of Ultrasonic Oscillation on Static and Sliding Friction.* Tribology Letters, 2012. **48**(1): p. 51-62.
94. Littmann, W., H. Storck, and J. Wallaschek, *Sliding friction in the presence of ultrasonic oscillations: superposition of longitudinal oscillations.* Archive of Applied Mechanics, 2001. **71**(8): p. 549-554.
95. Dong, S. and M.J. Dapino, *Wear reduction through piezoelectrically-assisted ultrasonic lubrication.* Smart Materials and Structures, 2014. **23**(10).
96. Goto, H., M. Ashida, and Y. Terauchi, *EFFECTS OF ULTRASONIC VIBRATION ON THE WEAR CHARACTERISTICS OF A CARBON-STEEL - ANALYSIS OF THE WEAR MECHANISM.* Wear, 1984. **94**(1): p. 13-27.
97. Eaves, A.E., et al., *Review of the application of ultrasonic vibrations to deforming metals.* Ultrasonics, 1975. **13**(4): p. 162-170.
98. Godfrey, D., *VIBRATION REDUCES METAL TO METAL CONTACT AND CAUSES AN APPARENT REDUCTION IN FRICTION.* Asle Transactions, 1967. **10**(2): p. 183-&.
99. Storck, H., et al., *The effect of friction reduction in presence of ultrasonic vibrations and its relevance to travelling wave ultrasonic motors.* Ultrasonics, 2002. **40**(1-8): p. 379-383.
100. Hesjedal, T. and G. Behme, *The origin of ultrasound-induced friction reduction in microscopic mechanical contacts.* Ieee Transactions on Ultrasonics Ferroelectrics and Frequency Control, 2002. **49**(3): p. 356-364.
101. Dinelli, F., et al., *Ultrasound induced lubricity in microscopic contact.* Applied Physics Letters, 1997. **71**(9): p. 1177-1179.
102. Gnecco, E., et al., *Dynamic superlubricity on insulating and conductive surfaces in ultra-high vacuum and ambient environment.* Nanotechnology, 2009. **20**(2).
103. Socoliuc, A., et al., *Atomic-scale control of friction by actuation of nanometer-sized contacts.* Science, 2006. **313**(5784): p. 207-210.
104. Roth, R., et al., *Lateral vibration effects in atomic-scale friction.* Applied Physics Letters, 2014. **104**(8).
105. Lantz, M.A., D. Wiesmann, and B. Gotsmann, *Dynamic superlubricity and the elimination of wear on the nanoscale.* Nature Nanotechnology, 2009. **4**(9): p. 586-591.
106. Yuya, P.A., D.C. Hurley, and J.A. Turner, *Relationship between Q-factor and sample damping for contact resonance atomic force microscope measurement of viscoelastic properties.* Journal of Applied Physics, 2011. **109**(11).
107. Truax, B.E., F.C. Demarest, and G.E. Sommargren, *Laser Doppler velocimeter for velocity and length measurements of moving surfaces.* Applied Optics, 1984. **23**(1): p. 67-73.
108. Der, L. *Frequency Modultation (FM) Tutorial*. 2008 [cited 2016 03/10/2016]; Available from: http://www.silabs.com/Marcom%20Documents/Resources/FMTutorial.pdf.
109. Hopcroft, M.A., W.D. Nix, and T.W. Kenny, *What is the Young's Modulus of Silicon?* Journal of Microelectromechanical Systems, 2010. **19**(2): p. 229-238.
110. Miyake, K., N. Satomi, and S. Sasaki, *Elastic modulus of polystyrene film from near surface to bulk measured by nanoindentation using atomic force microscopy.* Applied Physics Letters, 2006. **89**(3).
111. Aoike, T., et al., *Comparison of Macro- and Nanotribological Behavior with Surface Plastic Deformation of Polystyrene.* Langmuir, 2001. **17**(7): p. 2153-2159.

112. Bistac, S., A. Ghorbal, and M. Schmitt, *Friction of polystyrene: Consequence on nano-wear.* Progress in Organic Coatings, 2006. **55**(4): p. 345-354.
113. Argon, A.S., *A theory for the low-temperature plastic deformation of glassy polymers.* Philosophical Magazine, 1973. **28**(4): p. 839-865.
114. Miehe, C., S. Goktepe, and J.M. Diez, *Finite viscoplasticity of amorphous glassy polymers in the logarithmic strain space.* International Journal of Solids and Structures, 2009. **46**(1): p. 181-202.
115. Richeton, J., et al., *A formulation of the cooperative model for the yield stress of amorphous polymers for a wide range of strain rates and temperatures.* Polymer, 2005. **46**(16): p. 6035-6043.
116. Hertz, H.J., *Ueber die Berührung fester elastischer Körper.* Journal für die reine und angewandte Mathematik (Crelle's Journal), 1882. **92**: p. 156-171.
117. Whitney, W. and R.D. Andrews, *Yielding of glassy polymers: Volume effects.* Journal of Polymer Science Part C: Polymer Symposia, 1967. **16**(5): p. 2981-2990.
118. Richeton, J., et al., *Influence of temperature and strain rate on the mechanical behavior of three amorphous polymers: Characterization and modeling of the compressive yield stress.* International Journal of Solids and Structures, 2006. **43**(7-8): p. 2318-2335.
119. Gnecco, E., et al., *Channeling motion of gold nanospheres on a rippled glassed surface.* Nanotechnology, 2014. **25**(48): p. 485302.
120. Lüthi, R., et al., *Sled-Type Motion on the Nanometer Scale: Determination of Dissipation and Cohesive Energies of C60.* Science, 1994. **266**(5193): p. 1979-1981.
121. Rao, A., et al., *Trajectory fluctuations accompanying the manipulation of spherical nanoparticles.* Physical Review B, 2009. **80**(19).
122. Gnecco, E., et al., *Controlled manipulation of rigid nanorods by atomic force microscopy.* Nanotechnology, 2010. **21**(21).
123. Nita, P., et al., *Spinning and translational motion of Sb nanoislands manipulated on MoS2.* Nanotechnology, 2013. **24**(32).
124. Korayem, M.H., et al., *Three-dimensional modeling and simulation of the AFM-based manipulation of spherical biological micro/nanoparticles with the consideration of contact mechanics theories.* Proceedings of the Institution of Mechanical Engineers Part K-Journal of Multi-Body Dynamics, 2015. **229**(4): p. 370-382.
125. Falvo, M.R., et al., *Manipulation of individual viruses: Friction and mechanical properties.* Biophysical Journal, 1997. **72**(3): p. 1396-1403.
126. Iwata, F., M. Adachi, and S. Hashimoto, *A single-cell scraper based on an atomic force microscope for detaching a living cell from a substrate.* Journal of Applied Physics, 2015. **118**(13).
127. Castillo, J., M. Dimaki, and W.E. Svendsen, *Manipulation of biological samples using micro and nano techniques.* Integrative Biology, 2009. **1**(1): p. 30-42.
128. D'Acunto, M., S. Danti, and O. Salvetti, *Adhesion and friction contributions to cell motility*, in *Fundamentals of friction and wear on the nanoscale*, E. Gnecco and E. Meyer, Editors. 2015, Springer. p. 669-697.
129. Baharvand, H. and N. Aghdami, *Stem Cells Nanoengineering*. First ed. 2015: Wiley-Backwell.
130. Baranes, K., et al., *Topographic cues of nano-scale height direct neuronal growth pattern.* Biotechnology and Bioengineering, 2012. **109**(7): p. 1791-1797.
131. Zhou, F., et al., *Phenomenon of "contact guidance" on the surface with nano-micro-groove-like pattern and cell physiological effects.* Chinese Science Bulletin, 2009. **54**(18): p. 3200-3205.
132. Choi, C.H., et al., *Cell interaction with three-dimensional sharp-tip nanotopography.* Biomaterials, 2007. **28**(9): p. 1672-1679.
133. Norman, J. and T. Desai, *Methods for fabrication of nanoscale topography for tissue engineering scaffolds.* Annals of Biomedical Engineering, 2006. **34**(1): p. 89-101.

134. Wood, M.A., *Colloidal lithography and current fabrication techniques producing in-plane nanotopography for biological applications.* Journal of the Royal Society Interface, 2007. **4**(12): p. 1-17.
135. Wang, P.-Y., et al., *Modulation of alignment, elongation and contraction of cardiomyocytes through a combination of nanotopography and rigidity of substrates.* Acta Biomaterialia, 2011. **7**(9): p. 3285-3293.
136. Zhu, B.S., et al., *Nanotopographical guidance of C6 glioma cell alignment and oriented growth.* Biomaterials, 2004. **25**(18): p. 4215-4223.
137. Rebollar, E., et al., *Proliferation of aligned mammalian cells on laser-nanostructured polystyrene.* Biomaterials, 2008. **29**(12): p. 1796-1806.
138. Rajnicek, A.M., S. Britland, and C.D. McCaig, *Contact guidance of CNS neurites on grooved quartz: influence of groove dimensions, neuronal age and cell type.* Journal of Cell Science, 1997. **110**: p. 2905-2913.
139. Fujita, S., M. Ohshima, and H. Iwata, *Time-lapse observation of cell alignment on nanogrooved patterns.* Journal of the Royal Society Interface, 2009. **6**: p. S269-S277.
140. Teixeira, A.I., et al., *Epithelial contact guidance on well-defined micro- and nanostructured substrates.* Journal of Cell Science, 2003. **116**(10): p. 1881-1892.
141. Teixeira, A.I., et al., *The effect of environmental factors on the response of human corneal epithelial cells to nanoscale substrate topography.* Biomaterials, 2006. **27**(21): p. 3945-3954.
142. WojciakStothard, B., et al., *Guidance and activation of murine macrophages by nanometric scale topography.* Experimental Cell Research, 1996. **223**(2): p. 426-435.
143. Tang-Schomer, M.D., et al., *Bioengineered functional brain-like cortical tissue.* Proceedings of the National Academy of Sciences of the United States of America, 2014. **111**(38): p. 13811-13816.
144. Lancaster, M.A., et al., *Cerebral organoids model human brain development and microcephaly.* Nature, 2013. **501**(7467): p. 373-379.
145. Marín, O., et al., *Guiding Neuronal Cell Migrations.* Cold Spring Harbor Perspectives in Biology, 2010. **2**(2): p. a001834.
146. Toma, A., et al., *Ion beam erosion of amorphous materials: evolution of surface morphology.* Nuclear Instruments & Methods in Physics Research Section B-Beam Interactions with Materials and Atoms, 2005. **230**: p. 551-554.
147. Hülsenberg, D., A. Harnisch, and A. Bismarck, *Microstructuring of Glasses*. Springer Series in Material Science, ed. R. Hull, et al. 2008, Berlin: Springer. 323.
148. Navez, M., D. Chaperot, and C. Sella, *MICROSCOPIE ELECTRONIQUE - ETUDE DE LATTAQUE DU VERRE PAR BOMBARDEMENT IONIQUE.* Comptes Rendus Hebdomadaires Des Seances De L Academie Des Sciences, 1962. **254**(2): p. 240-&.
149. Toma, A., et al., *Self-organized ion-beam synthesis of nanowires with broadband plasmonic functionality.* Physical Review B, 2010. **81**(16).
150. Toma, A., et al., *Patterning polycrystalline thin films by defocused ion beam: The influence of initial morphology on the evolution of self-organized nanostructures.* Journal of Applied Physics, 2008. **104**(10).
151. Zhang, Z.Q., et al., *GaAs nanostructuring by self-organized stencil mask ion lithography.* Journal of Applied Physics, 2011. **110**(11).
152. Fan, J.A., et al., *Self-Assembled Plasmonic Nanoparticle Clusters.* Science, 2010. **328**(5982): p. 1135-1138.
153. De, S., et al., *Silver Nanowire Networks as Flexible, Transparent, Conducting Films: Extremely High DC to Optical Conductivity Ratios.* Acs Nano, 2009. **3**(7): p. 1767-1774.
154. van de Groep, J., P. Spinelli, and A. Polman, *Transparent Conducting Silver Nanowire Networks.* Nano Letters, 2012. **12**(6): p. 3138-3144.
155. Ward, D.R., et al., *Electromigrated nanoscale gaps for surface-enhanced Raman spectroscopy.* Nano Letters, 2007. **7**(5): p. 1396-1400.

156. Smentkowski, V.S., *Trends in sputtering.* Progress in Surface Science, 2000. **64**(1-2): p. 1-58.
157. Brow, R.K., *GLASS-SURFACE MODIFICATIONS DURING ION-BEAM SPUTTERING.* Journal of Non-Crystalline Solids, 1988. **107**(1): p. 1-10.
158. Albuschies, J. and V. Vogel, *The role of filopodia in the recognition of nanotopographies.* Scientific Reports, 2013. **3**.
159. Bartolo, L., et al., *Influence of membrane surface properties on the growth of neuronal cells isolated from hippocampus.* Journal of Membrane Science, 2008. **325**(1): p. 139-149.
160. Lavenus, S., et al., *ADHESION AND OSTEOGENIC DIFFERENTIATION OF HUMAN MESENCHYMAL STEM CELLS ON TITANIUM NANOPORES.* European Cells & Materials, 2011. **22**: p. 84-96.
161. Wang, P.Y., et al., *High-throughput characterisation of osteogenic differentiation of human mesenchymal stem cells using pore size gradients on porous alumina.* Biomaterials Science, 2013. **1**(9): p. 924-932.
162. Park, J., et al., *Nanosize and vitality: TiO2 nanotube diameter directs cell fate.* Nano Letters, 2007. **7**(6): p. 1686-1691.
163. Lancaster, M.V. and R.D. Fields, *Antibiotic and cytotoxic drug susceptibility assays using resazurin and poising agents*. 1996, Google Patents.
164. Fisher, T. *AlamarBlue Assay*. 2016 [cited 2016 03-08-2016]; Available from: https://tools.thermofisher.com/content/sfs/manuals/PI-DAL1025-1100_TI%20alamarBlue%20Rev%201.1.pdf.
165. Kulangara, K., et al., *Nanotopography as modulator of human mesenchymal stem cell function.* Biomaterials, 2012. **33**(20): p. 4998-5003.
166. Ludecke, C., et al., *Physical vapor deposited titanium thin films for biomedical applications: Reproducibility of nanoscale surface roughness and microbial adhesion properties.* Applied Surface Science, 2013. **280**: p. 578-589.
167. Svitkina, T.M., et al., *Mechanism of filopodia initiation by reorganization of a dendritic network.* Journal of Cell Biology, 2003. **160**(3): p. 409-421.
168. Carbone, G. and P. Decuzzi, *Elastic beam over an adhesive wavy foundation.* Journal of Applied Physics, 2004. **95**(8): p. 4476-4482.
169. Radmacher, M., et al., *Measuring the viscoelastic properties of human platelets with the atomic force microscope.* Biophysical Journal, 1996. **70**(1): p. 556-567.
170. Daffonchio, D., J. Thaveesri, and W. Verstraete, *CONTACT-ANGLE MEASUREMENT AND CELL HYDROPHOBICITY OF GRANULAR SLUDGE FROM UPFLOW ANAEROBIC SLUDGE BED REACTORS.* Applied and Environmental Microbiology, 1995. **61**(10): p. 3676-3680.
171. Scharfenberg, S., et al., *Observation of a snap-through instability in graphene.* Applied Physics Letters, 2012. **100**(2).
172. Meyer, J.C., et al., *The structure of suspended graphene sheets.* Nature, 2007. **446**(7131): p. 60-63.
173. de Parga, A.L.V., et al., *Periodically rippled graphene: Growth and spatially resolved electronic structure.* Physical Review Letters, 2008. **100**(5).
174. Pimentel, C., C.M. Pina, and E. Gnecco, *Epitaxial Growth of Calcite Crystals on Dolomite and Kutnahorite (104) Surfaces.* Crystal Growth & Design, 2013. **13**(6): p. 2557-2563.
175. Pimentel, C., E. Gnecco, and C.M. Pina, *High-resolution imaging of (100) kyanite surfaces using friction force microscopy in water.* Surface Science, 2015. **635**: p. 123-127.
176. Novoselov, K.S., et al., *Electric field effect in atomically thin carbon films.* Science, 2004. **306**(5696): p. 666-669.
177. Wang, X., L.J. Zhi, and K. Mullen, *Transparent, conductive graphene electrodes for dye-sensitized solar cells.* Nano Letters, 2008. **8**(1): p. 323-327.

178. Balandin, A.A., et al., *Superior thermal conductivity of single-layer graphene.* Nano Letters, 2008. **8**(3): p. 902-907.
179. Lee, C., et al., *Measurement of the elastic properties and intrinsic strength of monolayer graphene.* Science, 2008. **321**(5887): p. 385-388.
180. Zhu, Y.W., et al., *Graphene and Graphene Oxide: Synthesis, Properties, and Applications (vol 22, pg 3906, 2010).* Advanced Materials, 2010. **22**(46): p. 5226-5226.
181. Geim, A.K. and K.S. Novoselov, *The rise of graphene.* Nature Materials, 2007. **6**(3): p. 183-191.
182. Geim, A.K., *Graphene: Status and Prospects.* Science, 2009. **324**(5934): p. 1530-1534.
183. Choi, W., et al., *Synthesis of Graphene and Its Applications: A Review.* Critical Reviews in Solid State and Materials Sciences, 2010. **35**(1): p. 52-71.
184. Hedberg, J. *Wavy graphene*. 2015; A 3D model of graphene showing the undulations of the crystal]. Available from: http://www.jameshedberg.com/scienceGraphics.php.
185. Changgu, L., et al., *Elastic and frictional properties of graphene.* Physica Status Solidi B, 2009. **246**(11-12): p. 2562-7.
186. Dienwiebel, M. and R. Bennewitz, *Micro- and Nanotribology of Graphene*, in *Fundamental of Friction and Wear on the Nanoscale*, E. Gnecco and E. Meyer, Editors. 2015, Springer. p. 453-463.
187. Filleter, T., et al., *Friction and Dissipation in Epitaxial Graphene Films.* Physical Review Letters, 2009. **102**(8).
188. Kim, K.-S., et al., *Chemical Vapor Deposition-Grown Graphene: The Thinnest Solid Lubricant.* Acs Nano, 2011. **5**(6): p. 5107-5114.
189. Smolyanitsky, A., J.P. Killgore, and V.K. Tewary, *Effect of elastic deformation on frictional properties of few-layer graphene.* Physical Review B, 2012. **85**(3).
190. Li, Q., et al., *Substrate effect on thickness-dependent friction on graphene.* physica status solidi (b), 2010. **247**(11-12): p. 2909-2914.
191. Lee, C., et al., *Frictional Characteristics of Atomically Thin Sheets.* Science, 2010. **328**(5974): p. 76-80.
192. Li, S., et al., *The evolving quality of frictional contact with graphene.* Nature, 2016. **539**(7630): p. 541-545.
193. Marchetto, D., et al., *Friction and Wear on Single-Layer Epitaxial Graphene in Multi-Asperity Contacts.* Tribology Letters, 2012. **48**(1): p. 77-82.
194. Clark, N., A. Oikonomou, and A. Vijayaraghavan, *Ultrafast quantitative nanomechanical mapping of suspended graphene.* Physica Status Solidi B-Basic Solid State Physics, 2013. **250**(12): p. 2672-2677.
195. Miseikis, V., et al., *Rapid CVD growth of millimetre-sized single crystal graphene using a cold-wall reactor.* 2d Materials, 2015. **2**(1): p. 8.
196. Settembrini, F.F., et al., *Anisotropic straining of graphene using micropatterned SiN membranes*. 2016, Cornell University Library: arXiv:1606.06995. p. 8.
197. Bao, W.Z., et al., *Controlled ripple texturing of suspended graphene and ultrathin graphite membranes.* Nature Nanotechnology, 2009. **4**(9): p. 562-566.
198. Bao, W.Z., et al., *In Situ Observation of Electrostatic and Thermal Manipulation of Suspended Graphene Membranes.* Nano Letters, 2012. **12**(11): p. 5470-5474.
199. Booth, T.J., et al., *Macroscopic Graphene Membranes and Their Extraordinary Stiffness.* Nano Letters, 2008. **8**(8): p. 2442-2446.
200. Zabel, J., et al., *Raman Spectroscopy of Graphene and Bilayer under Biaxial Strain: Bubbles and Balloons.* Nano Letters, 2012. **12**(2): p. 617-621.
201. Larsen, M., et al., *Transfer induced compressive strain in graphene: Evidence from Raman spectroscopic mapping.* Microelectronic Engineering, 2014. **121**: p. 113-117.
202. Meyer, E., et al., *Nanoscale: Friction and Rheology on the nanometer scale*. 1998: World Scientific.

203. Robinson, B.J., N.D. Kay, and O.V. Kolosov, *Nanoscale Interfacial Interactions of Graphene with Polar and Nonpolar Liquids.* Langmuir, 2013. **29**(25): p. 7735-7742.
204. Filleter, T. and R. Bennewitz, *Structural and frictional properties of graphene films on SiC(0001) studied by atomic force microscopy.* Physical Review B, 2010. **81**(15).
205. Dienwiebel, M., et al., *Superlubricity of graphite.* Physical Review Letters, 2004. **92**(12).
206. Dong, Y., X. Wu, and A. Martini, *Atomic roughness enhanced friction on hydrogenated graphene.* Nanotechnology, 2013. **24**(37): p. 375701.
207. Suzuki, K., et al., *Atomic-Resolution Imaging of Graphite-Water Interface by Frequency Modulation Atomic Force Microscopy.* Applied Physics Express, 2011. **4**(12).
208. Tocci, G., L. Joly, and A. Michaelides, *Friction of Water on Graphene and Hexagonal Boron Nitride from Ab Initio Methods: Very Different Slippage Despite Very Similar Interface Structures.* Nano Letters, 2014. **14**(12): p. 6872-6877.
209. Zhou, H., et al., *Understanding controls on interfacial wetting at epitaxial graphene: Experiment and theory.* Physical Review B, 2012. **85**(3).
210. Tazi, S., et al., *Diffusion coefficient and shear viscosity of rigid water models.* Journal of Physics-Condensed Matter, 2012. **24**(28).
211. Prandtl, L., *Ein Gedankenmodell zur kinetischen Theorie der festen Körper.* ZAMM - Journal of Applied Mathematics and Mechanics / Zeitschrift für Angewandte Mathematik und Mechanik, 1928. **8**(2): p. 85-106.
212. Gnecco, E. and E. Meyer, *Fundamentals of friction and wear on the nanoscale*. Second ed. Nanoscience and technology. 2015, London: Publisher.
213. Gnecco, E., et al., *Anisotropy Effects in Atomic-Scale Friction.* Tribology Letters, 2012. **48**(1): p. 33-39.

# LIST OF PUBLICATIONS

The publications involved in the development of this thesis are the following ones:

I. J. G. Vilhena; C. Pimentel; **P. Pedraz**; F. Luo; P. A. Serena; C. M. Pina; E. Gnecco; R.Perez; *Atomic-Scale Sliding Friction on Graphene in Water*. ACS NANO. 10 - 4, pp. 4288 - 4293. 04/2016. ISSN 1936-0851.
The figures in Section 6.4 “Graphene on copper” are reproduced or modified from this paper unless otherwise exposed in the main text.

II. **P. Pedraz**; S. Casado; V. Rodriguez; M. C. Giordano; F. Buatier de Mongeot; A. Ayuso-Sacido; E. Gnecco, *Adhesion modification of neural stem cells induced by nanoscale ripple patterns*. NANOTECHNOLOGY. 27 - 12, 03/2016. ISSN 0957-4484.
The figures in Chapter 5 “Influence of rippled patterns in neural stem cells” are reproduced or modified from this paper unless otherwise exposed in the main text.

III. **P. Pedraz**; R. Wannemacher; E. Gnecco; *Controlled Suppression of Wear on the Nanoscale by Ultrasonic Vibrations*. ACS NANO. 9 - 9, pp. 8859 - 8868. 09/2015. ISSN 1936-0851.
The figures in Chapter 4 “Control of wear by ultrasonic vibrations” are reproduced or modified from this paper unless otherwise exposed in the main text.

IV. E. Gnecco; **P. Pedraz**; P. Nita; F. Dinelli; S. Napolitano; P. Pingue. *Surface rippling induced by periodic instabilities on a polymer surface*. NEW JOURNAL OF PHYSICS. 17, 03/2015. ISSN 1367-2630.
The figures in Chapter 3 “Surface rippling on polymers by AFM” are reproduced or modified from this paper unless otherwise exposed in the main text.

Other publications not included in the thesis:

V. **P. Pedraz**; J. Cortes; O. Hilgendorf; S, Rassid; C. Bogaert; O. Herouard; F. J.Montes; M. E. Diaz; R. L. Cerro. *Affinity separation by Langmuir-Blodgett deposition of bovine serum albumin using arachidic acid as specific ligand*. SEPARATION AND PURIFICATION TECHNOLOGY. 143, pp. 161- 168. 03/2015. ISSN 1383-5866.

VI. **P. Pedraz**; F. J. Montes; R. L. Cerro; M. E. Diaz. Characterization of Langmuir biofilms built by the biospecific interaction of arachidic acid with bovine serum albumin. THIN SOLID FILMS. 525, pp. 121 - 131.12/2012. ISSN 0040-6090.

# ACKNOWLEDGMENTS

Many people have contributed, in one way or another, to this thesis being finished today and I would like to acknowledge all of them.

First of all, I want to deeply thank Dr. Enrico Gnecco for giving me the opportunity to enter in this world, as well as his dedication and patience during these years. Specially, for his valuable time and for being always available, even in the distance.

Por otra parte, también quiero agradecer al Dr. Amadeo López Vázquez de Parga, mi tutor de la Universidad Autónoma, su disposición en todo momento así como su ayuda con todos los trámites implícitos en la realización de una tesis.

Asimismo, me gustaría dar las gracias al Dr. Rodolfo Miranda por su apoyo para que esta tesis pudiese finalizarse, así como por su capacidad para contagiar su pasión por la ciencia a todos los niveles. También me gustaría reconocer la disposición y el trabajo del grupo administrativo de IMDEA Nanociencia, en especial a la Dra. María Jesús Villa.

Furthermore, I would like to acknowledge all the members at IMDEA Nanoscience in Madrid, where I did almost the entire work included here, at Laboratory NEST (National Enterprise for nanoscience and nanotechnology) and CNR-INO (Consiglio Nazionale delle Ricerche-Istituto Nazionale di Ottica) in Pisa, where I made a short placement. Thanks for facilitating the multidisciplinary working environment indispensable for the accomplishment of this thesis.

Moreover, I want to thank the entities that, in part, financed this research. On the one hand, the Spanish Ministry of Economy and Competiveness for the MINECO project MAT2012-38810: *Friction on the atomic scale: Anisotropy effects and influence of mechanical excitations*, in which I was included. And on the other hand, the COST Action MP1303 *Understanding and controlling Nano and Mesoscale friction*, which allows me to participate in two workshops focused on nanotribology in May 2014 and June 2015 and in the summer school *Nanotribology: Theory and Applications* in August 2014. In addition, I would also like to thank COST Action MP1303 for conferring me a Short Term Scientific Mission (STSM) grant in order to financially support my PhD placement in Pisa in March 2016.

Additionally, I want to appreciate Skype™ contribution in this work for aiding the finalization of the thesis in the distance.

Al mismo tiempo, también quiero dar las gracias a todos los miembros que han pertenecido al grupo “Nanotribo” durante estos años. Al Dr. Reinhold Wannemacher, por su gran contribución en la realización de esta tesis. En particular, en el Capítulo 4 pero no únicamente, donde sus conocimientos en el campo de los ultrasonidos han sido cruciales. Al Dr. Carlos Pina (Universidad Complutense de Madrid), por su absoluta disposición para ayudarme en todo momento y por hacerme partícipe de sus muy interesantes conversaciones, tanto las de índole científica como aquellas que no lo eran. Al Dr. Juan Mazo, junto con Iván Bailera (Universidad de Zaragoza), por ampliar a 3 dimensiones el modelo del Capítulo 3, así como por su dedicación. Al Dr. Pawel Nita, por introducirme en el mundo de la nanolitografía

de polímeros. Al Dr. Rubén Álvarez, por ser capaz de contagiarme su increíble curiosidad, por sus buenos consejos tanto científicos como personales y por haberme enseñado tantas cosas sin esperar nada a cambio. Sabes que el haber finalizado esta tesis es, en gran medida, gracias a ti. A Almudena Inchausti, compañera de fatigas en estos últimos meses. Y a Carlos Pimentel (Universidad Complutense de Madrid), por su indispensable ayuda de principio a fin durante estos años de trabajo, por hacer más llevaderas las largas tardes de medidas en la Complutense; pero sobre todo, por su amistad.

Dado el carácter interdisciplinar de esta tesis, he tenido la posibilidad de colaborar con diversos grupos de investigación y numerosas personas.

En primer lugar, quería agradecer al Dr. Ángel Ayuso (CIOCC e IMMA) por involucrarse en el trabajo que ha dado como resultado el Capítulo 5 y por poner a nuestra disposición la línea celular utilizada en el mismo, así como los materiales necesarios. A la Dra. Vanessa Rodríguez, por iniciarme en el cultivo celular y por sus protocolos, que me resultaron de gran ayuda. También me gustaría reconocer especialmente la implicación del Dr. Santiago Casado en la obtención de las imágenes de AFM de dichas células así como en la interpretación de los resultados obtenidos. On the other hand, I would like to acknowledge Dr. Francesco Buatier de Mongeot and Dr. Maria Caterina Giordano (Università di Genova) for the preparation of ripples on glass used as substrates in Chapter 5.

I want to also thank Dr. Yu Zhou and Dr. Li Lin from the Beijing National Laboratory for Molecular Sciences and the College of Chemistry and Molecular Engineering at Beijing University and Dr. Feng Luo for proving the supported graphene samples used in part of Chapter 6.

Además, también quería dar las gracias al grupo del Dr. Rubén Pérez (Universidad Autónoma de Madrid) sin los que el modelo descrito en el Capítulo 6 de esta tesis, así como su entendimiento, no hubiese sido posible. En especial al Dr. Guillherme Vilhena, por su dedicación y amabilidad.

Additionally, I want to acknowledge Dr. Pasqualantonio Pingue (NEST Laboratory) and Dr. Franco Dinelli (CNR-INO) for giving me the opportunity to make a short placement with them and for their hospitality. Thanks to their planning capacity and their time, I gained experience in clean-room environment, graphene technology and other AFM techniques such as UFM and PeakForce. I can say that this period is one of the most enriching experiences of my PhD. I also want to thank the group of Dr. Stefano Rodaro at NEST, in special, Dr. Vaidotas Miseikis and Fabiana Settembrini for helping me with the preparation of suspended graphene membrane samples used in Chapter 6, even though the procedure was time consuming.

Asimismo, también me gustaría agradecer la disposición de las Dra. Isabel Rodríguez, Ana Pizarro y Adriana Arnáiz y de los Dr. Daniel Granados y Johann Mertens así como de Warren Smith y Antonio Buenilla; personas que, a pesar de no haber participado directamente en los resultados expuestos en esta tesis, han hecho posible que la misma haya avanzado mediante su trabajo, el uso de materiales, instrumentos u otros recursos. I would also want to include Dr. Karine Mougin (Institute of Materials Science of Mulhouse) for her kindness and helpful way to collaborate. It was a real pleasure to work with you, both in Mulhouse and in

Madrid. Furthermore, I would like to acknowledge Dr. Astrid de Wijn and Dr. Mark Rutland for inviting me to present part of this thesis at Stockholm University and KTH, respectively. I also want to thank Dr. Mark Rutland for valuable scientific discussions and his interest in this work.

Por otra parte, también quiero aprovechar este apartado para dar las gracias a mis compañeros de comidas, cafés y "Friday cakes" en IMDEA. Si algo bueno me llevo de esta tesis es haber tenido la oportunidad de conoceros. A Sara, por ser mi "Dori" particular, la alegría y la espontaneidad personificadas. A Patri, por su capacidad de escucha y las cañas compartidas después del trabajo. A Irene, por su serenidad y compañía en los inicios. A Alejandra, por alargar las comidas hasta el infinito mientras el resto estamos "reposando". A Felipe, por sus consejos sobre células y por haber sido la primera persona a quien conocí en IMDEA. A Fernando, por tener la cara más expresiva y graciosa que conozco, por lo que dices y lo que no. A Fran, por su sonrisa. Y a David, por su capacidad para no rendirse. También quiero agradecer al grupo de postdocs: A Jaime, Iván, Jose y, en especial a Manu, por acogerme y ser capaces de sacarme una sonrisa incluso cuando más se me resiste. Por otra parte, no quiero olvidarme de Juan Carlos y Pili, por hacer de IMDEA un lugar más acogedor.

Igualmente quiero tener en cuenta a mis amigos, tanto a los que están cerca como a los que están lejos. A Paula, Celia, Vane, Gloria, Ana, Jose y Luis porque a pesar de no veros tan a menudo como me gustaría, sé que puedo contar con vosotros. A María, por estar ahí a lo largo de los años, por la tranquilidad que me inspiras y por hacerme ver qué es lo importante. A Linnea y a Carmen por tantas tardes de café compartidas. Al "grupo de coro", por recordarme de dónde vengo. A mis amigos de Ingeniería Química, en particular, a Modi, Rosa y Vega, por compartir ese sentido práctico que todo ingeniero tiene, pero especialmente por hacerme un hueco en vuestras vidas y en tantos momentos inolvidables a lo largo de los años. Al grupo de "los miércoles de cervezas" por enseñarme desde el principio que esta ciudad merece la pena. A Mario, por descubrirme Madrid, por los momentos vividos, pero sobre todo, por los que nos quedan. A Lola, a las dos Marías, a Elena y a Isabel por permitirme entrar en vuestras vidas y sentirme como en casa.

A Pablo, por su capacidad para disfrutar de la vida y por hacerme partícipe de ello. Gracias por tu apoyo incondicional durante estos años y por esforzarte en comprenderme.

Finalmente, quiero reservar el último párrafo a mi familia, aquellos que aún sin entender lo que he hecho durante este tiempo me han ayudado de una forma u otra. En especial a mis padres, quienes me inculcaron la capacidad de esfuerzo y trabajo sin las cuales la realización de esta tesis no hubiese sido posible. A Marina, mi ojito derecho, por su sencillez, su integridad y por ser un ejemplo a seguir a pesar de su edad. Por último, a mi hermano, porque aunque él no lo sepa, el carácter vocacional que para mí tiene la investigación, se lo debo a él y a su capacidad de lucha.